12-8-2023

Improved methodology for conducted EMI assessment of power electronics and line impedance measurement

Mark Anthony Didat
Mississippi State University, mad643@msstate.edu

Improved methodology for conducted EMI assessment of power electronics and line impedance measurement

By

Mark Anthony Didat

Approved by:

Seungdeog Choi (Major Professor)
Andrew Lemmon
Masoud Karimi-Ghartemani
Yong Fu
Jenny Q. Du (Graduate Coordinator)
Jason M. Keith (Dean, Bagley College of Engineering)

A Dissertation
Submitted to the Faculty of
Mississippi State University
in Partial Fulfillment of the Requirements
for the Degree of Doctor of Philosophy
in Electrical and Computer Engineering
in the Department of Electrical and Computer Engineering

Mississippi State, Mississippi

December 2023

Name: Mark Anthony Didat

Date of Degree: December 8, 2023

Institution: Mississippi State University

Major Field: Electrical and Computer Engineering

Major Professor: Seungdeog Choi

Title of Study: Improved methodology for conducted EMI assessment of power electronics and line impedance measurement

Pages in Study: 99

Candidate for Degree of Doctor of Philosophy

Electromagnetic Interference (EMI), primarily common mode (CM), is problematic in a wide range of electronic circuits due to its propensity to radiate, particularly in high power applications. It is routine for much effort and resources to be dedicated to its characterization and reduction as EMI compliance is a requirement for most electronic systems and devices, including power electronics.

Many well-known factors contribute to a system's EMI performance including intentional coupling from system components as well as unintentional coupling from parasitics. Sources of intentional coupling may include Y-capacitors intended to mitigate EMI as part of a filter. Unintentional coupling is more elusive and can exist throughout the system in PCB layout, cabling, load construction, and internal to components such as inverter bridges. Lesser-known contributions to EMI performance irregularities can be EMI filter asymmetries, switching asymmetries, line impedance variances, and galvanic coupling from the metrology intended to measure EMI. It is critical to understand these contributors to facilitate designs with optimal EMI performance.

EMI filters are often added to designs with no consideration to asymmetries in construction and component tolerances. This proposal evaluates the impact to CM currents in cases of coupling or leakage inductance imbalances of a CM choke. Similarly, CM currents are also evaluated for cases when EMI filter Y-capacitor imbalances span the components tolerance band. Also analyzed are switching asymmetries in a typical converter topology to understand EMI impact and evaluate potential benefits if intentional asymmetric switching is applied. A practical method is introduced to measure line impedance upstream of devices under test as line impedance variation can impact the performance of EMI filter design. However, few documented practices exist to measure line impedance without specialized instrumentation.

Finally, this work proposes a streamlined method for conducted emissions evaluation employing an oscilloscope, differential voltage probes, and post-processing software implemented in MATLAB. This method eliminates unintended metrology ground coupling that can significantly impact EMI measurements and minimizes risk of instrumentation damage particularly in high power systems.

DEDICATION

This work is dedicated to God that it may glorify Him through my Lord and Savior Jesus Christ.

ACKNOWLEDGEMENTS

First and foremost, I thank my wife, Jennifer. This endeavor was her idea and she supported me vehemently even when the program stretched out to eight years taking time away from our family. Dr. Andrew Lemmon who mentored, guided, and encouraged me from the beginning. He always had an idea for a new strategy at every obstacle. Dr. Seungdeog Choi who trusted my vision and gave me the freedom necessary to pursue my body of work. And last, my fellow graduate students Dr. Christopher New, Ashik Amin, and Dinh Le, who provided endless support through the years.

Thank you.

TABLE OF CONTENTS

DEDICATION ii

ACKNOWLEDGEMENTS iii

LIST OF TABLES vi

LIST OF FIGURES vii

CHAPTER

I. INTRODUCTION 1

1.1 Motivation 1
1.2 State of the Art 3
1.3 Challenges 5

II. ANALYSIS OF EMI FILTER IMBALANCES AND ASYMMETRIC DEADTIME SWITCHING 7

2.1 Proposed Analytical Methods 7
2.2 Approach 10
2.3 Results 22

III. METHOD FOR MEASURING SINGLE PHASE LINE IMPEDANCE 30

3.1 Proposed Analytical Methods 30
3.2 Approach 31
3.3 Results 37

IV. IMPROVED METHODOLOGY FOR CONDUCTED EMI ASSESSMENT 48

4.1 Proposed EMI Assessment Method 48
4.2 Accuracy Analysis of Alternate EMI Measurement System 52
4.3 EMI receiver Requirements and Operation 54
4.3.1 Application Standard and frequency Band 55
4.3.2 Measurement System and Compliance Limits 55
4.3.3 EMI Receiver Operation 56
4.4 MATLAB EMI Receiver Emulator (MERE) 58
4.5 Method Verification 63

4.5.1 Function Generator Verification....63
4.5.2 WBG-Based Converter Validation....65
4.6 Predictive Model Application....74
4.7 Results....84

V. CONCLUSION....86

5.1 Conclusion and Contributions....86
5.2 Publications....88
5.3 Future Work....88

REFERENCES....89

APPENDIX

A. SUPPORTING ANALYSIS AND DOCUMENTATION....95

A.1 MERE Comparison to Yang/Wang Method....96
A.2 Noise Floor Analysis....97

LIST OF TABLES

Table 2.1 Ratio of Half Bridge to Full Bridge CM Current 8
Table 2.2 EMI Filter Parameters 11
Table 2.3 Asymmetry Sensitivity Matrix 12
Table 2.4 EMI Filter Imbalance Results Matrix....22
Table 3.1 Line Impedance Measurement Results of Experiment 1....39
Table 3.2 Operating Conditions and Metrology of the Measurement Waveform....40
Table 3.3 Experiment Description....44
Table 3.4 Line Impedance Measurement Results of Experiment 2....44
Table 4.1 Amplitude Accuracy Comparison: Conventional Setup and Isolated Setup....53
Table 4.2 Conducted Limits and Quasi-peak Time Constants [27] 56
Table 4.3 Experiment Descriptions 65
Table 4.4 Operating Conditions and Metrology of Study 66

LIST OF FIGURES

Figure 2.1 Half Bridge Test Platform Schematic [1], [2], [3], [4] 9

Figure 2.2 Full Bridge Test Platform Schematic 9

Figure 2.3 LTspice Simulation Model for Full Bridge Testbed 10

Figure 2.4 Inductor and Capacitor Equivalent Models 10

Figure 2.5 Single Stage EMI Filter 11

Figure 2.6 CEM for Half Bridge EUT [10] with Reduced Simulation Version on Right 15

Figure 2.7 CEM for Full Bridge EUT – Before Simplification 16

Figure 2.8 Simplified CEM for Full Bridge EUT 17

Figure 2.9 Simulink and m-script Agreement of i_{CMo}, i_{CMi}, and i_{BP} for Half Bridge CEM 18

Figure 2.10 Full bridge CEM Simulink 19

Figure 2.11 Full Bridge CEM with Leakage Imbalance 20

Figure 2.12 Switching Signals with Deadtime 21

Figure 2.13 Input CM Current Spectral Magnitude at All Frequency Bands 23

Figure 2.14 Input DM Current Spectral Magnitude at All Frequency Bands 24

Figure 2.15 RMS CM and DM Currents Compensated to Baseline 25

Figure 2.16 Gate Signal Shifting in Bipolar Pairs 27

Figure 2.17 Reduction Results Plot: MATLAB vs LTspice 28

Figure 2.18 Half Bridge: LTspice and Physical Fixture Base Plate Current Agreement 29

Figure 3.1 Equivalent Circuit of Residential Line Feed Including Impedance Measurement Components 32

Figure 3.2 Simplified Equivalent Circuit of Line Impedance Measurement Method Using Capacitor Load....33

Figure 3.3 Voltage (blue) and Current (green) Observed at Switch Close Event....34

Figure 3.4 Square 'D' Trip Curve for QO Circuit Breaker Series....36

Figure 3.5 Alternate Line Impedance Measurement Method using Resistive Load with Duty Cycle Switching....36

Figure 3.6 LTspice simulation: Voltage (blue) and Current (red). Left: Resistor Load with Duty Cycle Switching and Right: Capacitor Load with Simple Switching....37

Figure 3.7 Measurement Switching Distribution....38

Figure 3.8 Experimental Voltage Sag and Current Peak at 90° Switching Angle Measured with Shunt: Blue= Voltage (V), Red= Current....41

Figure 3.9 Experimental Voltage Sag and Current Peak at 90° Switching Angle Measured with Clamp: Blue= Voltage (V), Red= Current(A)....41

Figure 3.10 Line Impedance Distributed as External Source and Internal Wire Feed....42

Figure 3.11 Measurement Circuit Impacted by Multiple Incremental Loaded Circuits Connected to the AC Mains....45

Figure 3.12 LTspice Simulation Waveforms with *Ls* = 138μH.....47

Figure 4.1 EMI Converter Testbed of [1], [2] with Induction Motor Load [5] with CM Loops....49

Figure 4.2 Quasi-peak Detection Circuit [40]....55

Figure 4.3 Example Block Diagram of EMI Receiver [26]....57

Figure 4.4 MERE Functional Block Diagram for CISPR Band B....60

Figure 4.5 EMI Performance Comparison Plots for a 400 kHz Square Wave Stimulus: (a) Peak, (b) QP, and (c) Average....64

Figure 4.6 High-Power Converter EMI Testbed....68

Figure 4.7 a) LISN Metrology Attachments on the Realized Testbed, and Notional Diagram of the Metrology Connections for (b) Experiment 1 and (c) Experiment 2....69

Figure 4.8 (a) Experiment 1: Quasi-peak Spectra: EMI Receiver Measurement vs. MERE Output with EMI Receiver Connected (b) Experiment 2: Quasi-peak Spectra: MERE Output with EMI Receiver Connected (Experiment 1) vs MERE Output without EMI Receiver Connected 70

Figure 4.9 Ground Currents with (Experiment 1) and without (Experiment 2) the EMI Receiver Connected 73

Figure 4.10 EMI Receiver Ground Current as a Function of DC Bus Voltage 73

Figure 4.11 LTspice Simulation Model of Testbed for Experiments 1 and 2 74

Figure 4.12 Empirical Testbed Ground Current Comparison with LTspice Simulation for Experiments 1 and 2 75

Figure 4.13 LTspice Compensated Testbed EMI Receiver Data from Experiment 1 Compared to Post processed Isolated Method of Experiment 2 76

Figure 4.14 CEM Model for the Testbed Configuration of Figure 4.1 with Normal LISN Current (brown) and Incremental LISN Current (green) via the Earth Ground Connection. 77

Figure 4.15 MATLAB Simulink (top) and LTspice (bottom) CEM Models for Testbed of Figure 4.1 78

Figure 4.16 Empirical Testbed Ground Current Comparison (top) and LISN Voltage (bottom) with CEM Model for Experiments 1 and 2 79

Figure 4.17 Simplified CEM with Load Impedances Magnitudes at Fundamental Frequency of 177kHz 80

Figure 4.18 LISN Current Comparison versus Frequency With and Without EMI Receiver Connected 82

Figure A.1 Comparison between MERE and Yang, Wang et al. Predictor [35] 96

Figure A.2 Testbed Noise Floor Measurements at Vdc = 0 V and Gate Drivers Switching 98

Figure A.3 Testbed Noise Floor Measurement at Vdc = 0 V and Gate Drivers not Switching 98

Figure A.4 Noise Floor Measurements with and without Attenuators 99

CHAPTER I

INTRODUCTION

1.1 Motivation

Review of EMI characterization and EMI filters suggests that asymmetries are undesirable as they create a significant differential to common mode noise conversion [1], [2], [5], [6], [7]. In particular, the theory proposed by Lee et. al in [5] suggests that differential mode (DM) conversion to common mode (CM) generates noise that is more difficult to attenuate. Lee concludes that the transformed noise is linear and that the converted noise due to the unbalances of Y-capacitors and choke inductors can be larger than the attenuated noise. This characteristic was carefully considered and observed as this study progressed.

Xue et. al in [6] concurs that filter asymmetry is driven by component tolerances, construction, and processes directly impacting the value of filter components and their parasitics. The author also claims that the relevant asymmetry range spans the tolerance range of the components within the EMI filter. In this study, this guidance was used as a basis for establishing the parameters of the planned evaluation procedures.

Rebholz and Tenbohlen [7] warn that series inductances are “especially responsible” for noise mode transformation. Discovery of this claim prompted a revision of the proposed evaluation procedure to include variation of the CM choke leakage inductances, which are stated to act as DM filters. These series inductances are known to convert DM noise to CM noise. The

authors present a well-defined method to design a symmetrical EMI filter by measuring the CM and DM input impedance of the system.

Wittenbreder [9] clearly explains the role CM choke leakage inductance plays in EMI filter topologies as an attenuator of DM signals. The author states that additional DM chokes are often not necessary in EMI filters as the small leakage inductance of the CM choke provides adequate DM attenuation. This point is also reinforced in [5], [6] where CM choke leakage inductance is identified as DM inductors.

The voltage sag of a power feed is the result of the $i \cdot R$ drop across the line and source resistances. As this resistance is typically small, a large current is necessary to generate a significant voltage sag. These low voltage disturbances, which can be acute (voltage dips and interrupts) or chronic (low line), are the result of large loading situations. The poor power quality from voltage dips and sags is far-reaching, impacting industrial, commercial, and residential systems, and in some cases, causing outages, data loss, and appliance damage [11], [12], [13]. In addition to power quality deficiencies, line impedance variation imposes other challenges, such as impacting the performance of equipment's EMI filters as described in [16] where the authors show attenuation increases with line impedance. Line impedance is also critical when specifying protective devices such as fast blow fuses used in the power input stages of controls where a low line impedance can lead to nuisance trips. Designers would need extensive quantification and characterization of the line impedance of their targeted environments to allow their designs to be robust to this key noise parameter.

EMI compliance is evaluated against quasi-peak (QP) and average limits per 47 CFR part 15 [27]. A significant challenge associated with these compliance measurements is achieving full-band quasi-peak (QP) and average data given the time constants and dwell time requirements of

[27], which are adopted from and defined in the CISPR 16-1-1 standard [26]. Many researchers have identified QP as the critical quantity for evaluating EMI compliance [28], [30], [31]; while [32] stresses that the QP measurement is of greatest importance.

Compliance evaluation using full QP scans with conventional EMI instruments is typically a time intensive task. Most significant is that conventional EMI instrumentation introduces galvanic earth ground coupling which can significantly alter measurement results and pose risk to instrument damage in high power applications. This work proposes a streamlined method for emissions evaluation of power electronics employing an oscilloscope, differential voltage probes, and post-processing software implemented in MATLAB. This proposed method eliminates unintended metrology ground coupling, yields faster full quasi-peak scan times, and minimizes risk of instrumentation damage.

1.2 State of the Art

Line impedance quantification has been historically difficult to achieve straightforwardly or with high accuracy. There are few commercially available instruments capable of measuring line impedance prompting many engineers to rely on estimations, calculations, or alternate measurement methods [18]. Other instrumentation capable of measuring line impedance is intended to mitigate and correct power quality making the equipment costly and superfluous for this dedicated task [14], [15]. Techniques using a purely resistive load would require a high wattage and impractical load resistor to generate the high current needed for accurate results or the addition of complex and costly switching circuitry to generate a momentary significant load current [14], [17], [18]. Attempting to measure the line resistance with a small current would result in low signal-to-noise ratio (SNR) and poor accuracy. It is important to maintain optimum SNR as some environments, particularly commercial and industrial, may exhibit high noise content in

the measured signals contributing to significant metrology errors. For example, 1 Volt of signal noise infused on a 120VAC signal can produce 10% or more incremental error in the calculated line impedance if low current measurements are utilized.

EMI compliance evaluation necessitates the use of a CISPR compliant EMI receiver. A typical EMI receiver requires that the user select points of interest from the peak output and then QP and average values are produced only for these selected frequency ranges. Muller makes this recommendation as one of the QP time saving principles outlined in [33]. This method is recommended because computing full-band QP data over the entire compliance band often requires several hours or more [29]. However, this timesaving approach, which relies on the operator selecting ranges of interest, could lead to false compliance passes because exceedances may exist in omitted sections of the scan. On the other hand, a designer may incur unnecessary cost to improve a peak exceedance that may be compliant when properly measured and evaluated as QP.

Considering these recognized challenges, significant efforts have been undertaken to provide full-band QP and average spectra with fast execution time. For example, some instrument vendors have developed hardware that is specifically designed to perform fast QP computations. One such instrument, the Gauss Instruments TDEMI X [34], is marketed as being 64,000 times faster than conventional EMI receivers. However, instruments with high-speed analysis capabilities are prohibitively expensive. Another approach is the development of “offline” computational tools that can compute QP spectra from recorded experimental data or simulation predictions. For example, L. Yang and S. Wang [35] and Karaca et al. [30] offer predictive EMI performance analysis tools with fast computation times. These methods work in the frequency domain and rely on approximations for calculations of the compliance variables. Krug and Prusser

[36] offer a similar frequency-based method. Their approach dramatically reduces peak scan times and offers some improvements for the computation of QP spectra as well. Giezendanner et al. [42] introduce a method of computing QP spectra in the time-domain and discuss the computational challenges associated with this approach.

Conventional EMI test methods may introduce new challenges when evaluating wide band-gap (WBG) based power electronic converter systems such as that presented in [21], [22]. Connecting a ground-referenced EMI receiver to this type of converter system creates additional galvanic common-mode (CM) paths from the source filter [23] and power module parasitic capacitances [24] through the EMI receiver's earth ground connection. These paths, involve implicit capacitive couplings in the power source, the load, the neutral connection point, and the power module(s) employed in the converter itself. The CM loop introduced by the galvanic instrumentation ground can dramatically impact the EMI behavior and compliance performance of this system, as reported in [21], [22], making it advantageous to employ an isolated method.

1.3 Challenges

This study is presented in three chapters in increasing scholarly significance. The main topics and challenges addressed in this dissertation are as follows:

I. Develop and conduct a comprehensive design of experiments inclusive of all EMI filter factors and levels to understand their impact on EMI performance. Investigate switching deadtime asymmetries to evaluate potential benefits to CM noise reduction.

II. Develop and validate method to quantify line impedance that is accurate, low cost, and uses available lab instrumentation and components.

III. Develop an improved method to assess conducted EMI compliance which will isolate the metrology from the DUT.

- Develop an alternate isolated measurement metrology.
- Demonstrate the alternate measurement instrumentation's accuracy is comparable to conventional instrumentation.
- Develop a method to post-process the alternate methods output measurement data to produce the EMI compliance metrics: Quasi-peak and Average.
- Show experimentally the alternate isolated approach with post-processing produces comparable EMI compliance metrics as the conventional method.
- Determine experimentally the impact of the CM ground coupling path introduced by conventional EMI receivers
- Develop a prognostic model that can be used by designers to predict impact of EMI receiver earth ground coupling in their designs.

CHAPTER II

ANALYSIS OF EMI FILTER IMBALANCES AND ASYMMETRIC DEADTIME SWITCHING

2.1 Proposed Analytical Methods

When working to minimize CM currents in power switching designs, it is important to understand their sources. This work's objective is to characterize the sensitivity of CM currents caused by asymmetries in EMI filter designs. The asymmetries are modeled from component tolerances, construction variances, and parasitics.

A single-phase full bridge inverter simulation model was the evaluation tool for this study. The full bridge (FB) topology in theory should generate no common mode currents which allow for accurate observation of the impact of the filter asymmetries. This claim is validated experimentally with the understanding that the inclusion of parasitic capacitances in the model will allow for some level of CM currents which will be substantially less than a half bridge system. A comparison of CM current magnitudes for the full bridge inverter system versus a half bridge version of the same system is shown in Table 2.1. The half bridge on average conducts more than 13 times the CM current than the full bridge when no EMI filter is present. Considering only RMS and low frequency (LF) band the half bridge dominance increases greater than a factor of 20. This relation holds true except for the two cases in the high frequency (HF) and very high frequency (VHF) bands with the balanced filter in which case the parasitics become more significant. This

validates the previous claim that a full bridge inverter generates comparatively small levels of CM currents.

Table 2.1 Ratio of Half Bridge to Full Bridge CM Current

Frequency Range	No Filter	Balanced Filter
RMS	31.68	7.03
LF	30.12	20.85
MF	8.07	7.41
HF	5.64	0.50
VHF	26.71	0.56

This study leverages prior research of a joint Mississippi State University and University of Alabama team in the area of EMI characterization [1], [2], [3], [4]. This research involved the construction of an EMI test platform to evaluate the behavior of common mode currents for high-performance power electronics applications. The test platform (Figure 2.1) includes a single-phase half bridge inverter as the equipment under test (EUT) fed by a HVDC power source through two input line impedance stabilization networks (LISNs). The inverter load is also two opposing LISNs. These four LISNs allow for measurement and comparison of the currents of interest. This test platform also supports full bridge operation which is the form utilized herein. This prior work has led to significant findings of common mode current mitigation techniques from the application of compensating capacitors attached externally to the half bridge module. This previous work also benefited from a representative LTspice simulation model for predictive analysis which is the primary analytical tool used in this study.

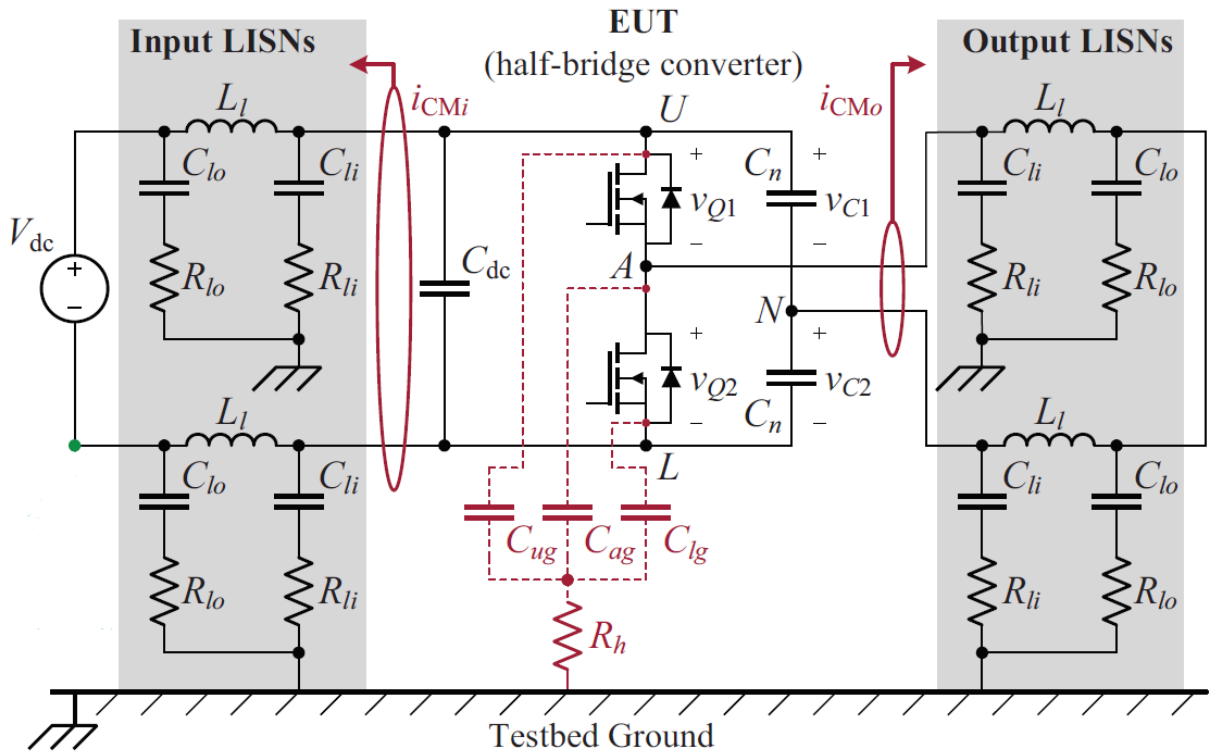

Figure 2.1 Half Bridge Test Platform Schematic [1], [2], [3], [4]

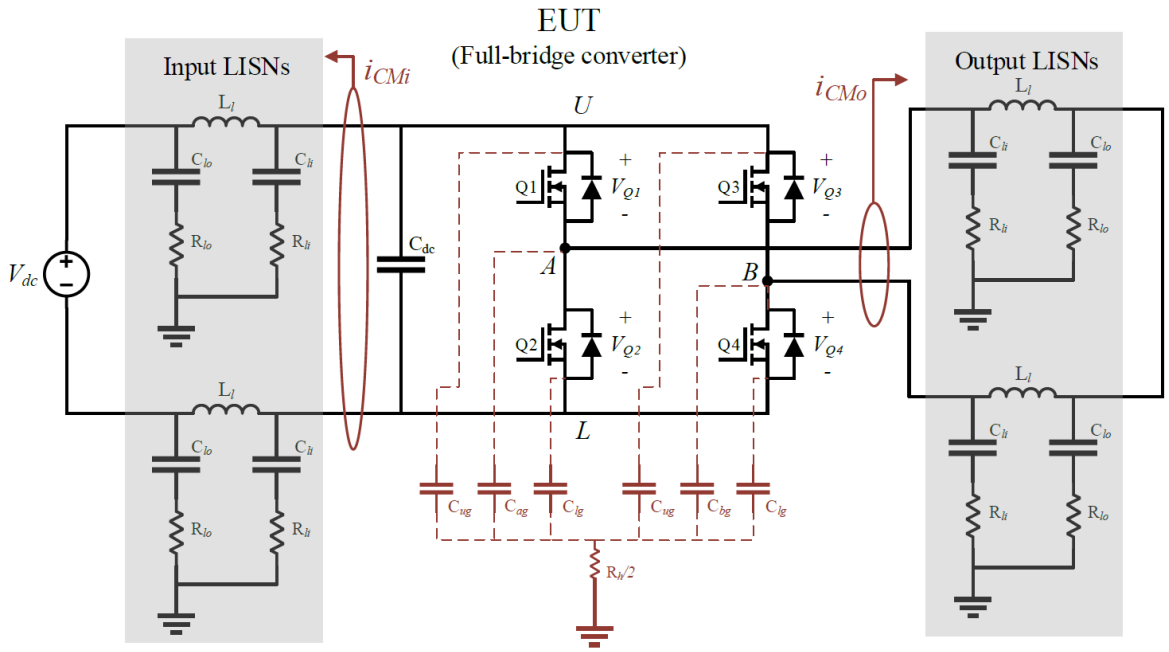

Figure 2.2 Full Bridge Test Platform Schematic

2.2 Approach

The aforementioned full bridge LTspice model was modified with the addition of a single stage EMI filter (Figure 2.5) inserted between the input LISNs and the inverter bridge. The usual DM filtering X-capacitor was omitted for two reasons: (1) the X-capacitor cannot generate an un-balanced condition and (2) the presence of the large bridge bulk capacitance (C1 of Figure 2.3) trivializes the addition of any practically sized X-capacitor.

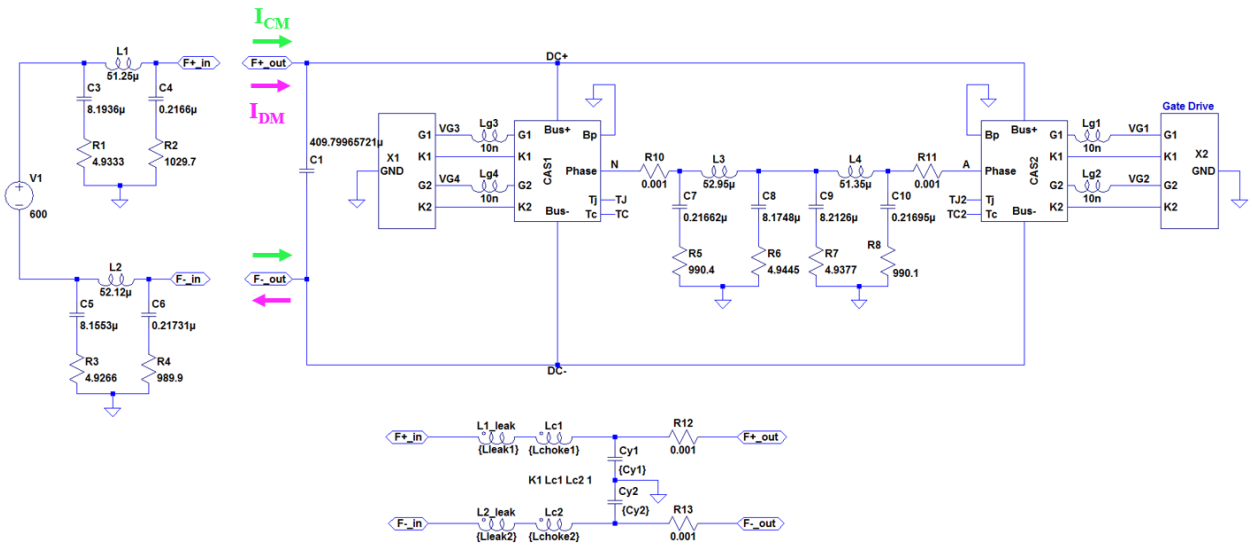

Figure 2.3 LTspice Simulation Model for Full Bridge Testbed

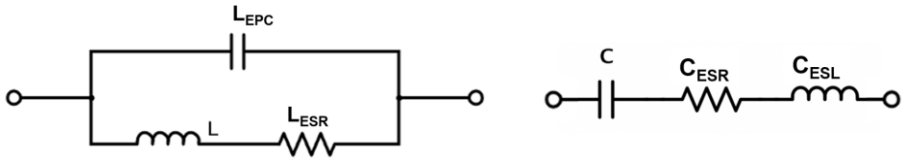

Figure 2.4 Inductor and Capacitor Equivalent Models

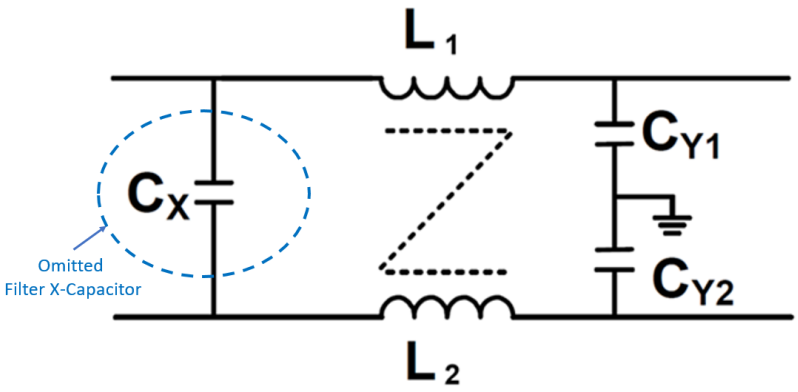

Figure 2.5 Single Stage EMI Filter

To evaluate filter asymmetries, the choke inductors and Y-capacitors were replaced with their equivalent models (Figure 2.4) and leakage inductances were included in the CM choke model. These parameters of the common mode filter components were stepped over a range that is representative of the physical component variations and are described in detail in Table 2.2.

Table 2.2 EMI Filter Parameters

CHOKE		
Parameter	**Tolerance**	**Value Range**
Inductance	5.1mH +/- 0.15mH	5.25mH to 4.95mH (*0.05mH steps)*
Leakage inductance	23uH MAX	0 and 23uH
Inductor ESR	30mΩ MAX	15mΩ and 30mΩ
Inductor ESR max imbalance	15mΩ MAX	0 and 15mΩ
Inductor EPC	15pF	0 and 15pF
Y- CAPACITORS		
Parameter	**Tolerance**	**Value Range**
Capacitance	20%, 2200pF nominal	1760pF to 2640pF, 220pF steps
Capacitor ESL	5nH	0 and 5nH
Capacitor ESR	20mΩ	0 and 20mΩ

The values represent actual tolerances of a commercial choke provided by a major manufacturer. The inductance imbalance is stepped from -0.15mH to +0.15mH from nominal 5.1mH individually on each winding. The leakage inductances were toggled from zero to maximum for each coil same as the inductor equivalent parallel capacitance. Likewise, the Y-capacitor tolerances, ESL, and ESR were toggled from zero to maximum for each individual component. This manner was chosen to allow for observation of impact by each parameter.

The accumulation of all test configurations is displayed in Table 2.3. Accommodating the above design of experiment combinations for all 14 parameters requires 32 individual simulation runs. Given the complexity of the LTspice model and maximum time step limitation, simulations typically exceeded 15 minutes to reach steady state transient results.

Table 2.3 Asymmetry Sensitivity Matrix

Run	L1 (mH)	L1-ls (µH)	L1-ESR (mΩ)	L1-EPC (pF)	L2 (mH)	L2-ls (µH)	L2-ESR (mΩ)	L2-EPC (pF)	Cy1 (pF)	Cy1-ESR (mΩ)	Cy1-ESL (nH)	Cy2 (pF)	Cy2-ESR (mΩ)	Cy2-ESL (nH)	Comments
Baseline2	5.1	23	30	15	5.1	23	30	15	2200	20	5	2200	20	5	Baseline w/ parasitics
1	5.25	23	30	15	5.1	23	30	15	2200	20	5	2200	20	5	Max inductance imbalance high DC+
2	5.15	23	30	15	5.1	23	30	15	2200	20	5	2200	20	5	Mid inductance imbalance high DC+
3	5.05	23	30	15	5.1	23	30	15	2200	20	5	2200	20	5	Mid inductance imbalance low DC+
4	4.95	23	30	15	5.1	23	30	15	2200	20	5	2200	20	5	Max inductance imbalance low DC+
5	5.1	23	30	15	5.25	23	30	15	2200	20	5	2200	20	5	Max inductance imbalance high DC-
6	5.1	23	30	15	5.15	23	30	15	2200	20	5	2200	20	5	Mid inductance imbalance high DC-
7	5.1	23	30	15	5.05	23	30	15	2200	20	5	2200	20	5	Mid inductance imbalance low DC-
8	5.1	23	30	15	4.95	23	30	15	2200	20	5	2200	20	5	Max inductance imbalance low DC-
9	5.1	23	30	15	5.1	23	30	15	2640	20	5	2200	20	5	Y-Cap DC+ tolerance value (+20%)
10	5.1	23	30	15	5.1	23	30	15	2420	20	5	2200	20	5	Y-Cap DC+ tolerance value (+10%)
11	5.1	23	30	15	5.1	23	30	15	1980	20	5	2200	20	5	Y-Cap DC+ tolerance value (-10%)
12	5.1	23	30	15	5.1	23	30	15	1760	20	5	2200	20	5	Y-Cap DC+ tolerance value (-20%)
13	5.1	23	30	15	5.1	23	30	15	2200	20	5	2640	20	5	Y-Cap DC- tolerance value (+20%)
14	5.1	23	30	15	5.1	23	30	15	2200	20	5	2420	20	5	Y-Cap DC- tolerance value (+10%)
15	5.1	23	30	15	5.1	23	30	15	2200	20	5	1980	20	5	Y-Cap DC- tolerance value (-10%)
16	5.1	23	30	15	5.1	23	30	15	2200	20	5	1760	20	5	Y-Cap DC- tolerance value (-20%)
17	5.1	23	30	15	5.1	23	30	15	2640	20	5	1760	20	5	Y-Caps max tolerance spread (2x20%), DC+ high
18	5.1	23	30	15	5.1	23	30	15	1760	20	5	2640	20	5	Y-Caps max tolerance spread (2x20%), DC- high
19	5.1	23	30	15	5.1	23	15	15	2200	20	5	2200	20	5	ESR imbalance +0.15
20	5.1	23	15	15	5.1	23	30	15	2200	20	5	2200	20	5	ESR imbalance -0.15
21	5.1	23	30	0	5.1	23	30	15	2200	20	5	2200	20	5	L1 0 EPC
22	5.1	23	30	15	5.1	23	30	0	2200	20	5	2200	20	5	L2 0 EPC
23	5.1	0	30	15	5.1	23	30	15	2200	20	5	2200	20	5	L1 0 leakage
24	5.1	23	30	15	5.1	0	30	15	2200	20	5	2200	20	5	L2 0 Leakage
25	5.1	23	30	15	5.1	23	30	15	2200	0	5	2200	20	5	Cy1 0 ESR
26	5.1	23	30	15	5.1	23	30	15	2200	20	5	2200	0	5	Cy2 0 ESR
27	5.1	23	30	15	5.1	23	30	15	2200	20	0	2200	20	5	Cy1 0 ESL
28	5.1	23	30	15	5.1	23	30	15	2200	20	5	2200	20	0	Cy2 0 ESL
29	5.25	23	30	15	5.1	23	30	15	2640	20	5	1760	20	5	Combined L imbalance, cap tolerance worst case DC+
30	5.1	23	30	15	5.25	23	30	15	1760	20	5	2640	20	5	Combined L imbalance, cap tolerance worst case DC-
31	5.1	23	30	15	5.25	23	30	15	2640	20	5	1760	20	5	Combined L imbalance, cap tolerance offsetting DC+
32	5.25	23	30	15	5.1	23	30	15	1760	20	5	2640	20	5	Combined L imbalance, cap tolerance offsetting DC-

The resulting impact of each test configuration was evaluated by comparison to baseline of the CM and DM currents at the input of the inverter bridge (post EMI filter). This location

includes the current contributions circulating in the EUT due to the filter asymmetries and are measured via the placement of two shunt resistors on the DC+ and DC- bus (R12 and R13 respectively shown in Figure 2.3). The CM and DM currents are calculated per equations (2.1) and (2.2).

$$I_{CM} = \frac{1}{2}\left(I_{R_{12}} + I_{R_{13}}\right) \tag{2.1}$$

$$I_{DM} = \frac{1}{2}\left(I_{R_{12}} - I_{R_{13}}\right) \tag{2.2}$$

Typically, spectral power is used as a figure of merit (Oswald et. al [8]) in this type of analysis. This can be problematic when comparing a set of data with wide varying magnitudes as minor changes could become "invisible" when viewed in a plot due to the dominance of squaring larger magnitudes. For this reason, spectral magnitude was chosen as a substitute for spectral power.

After the LTspice simulation was executed for each configuration, the FFT data was exported and processed through MATLAB to provide the input CM and DM current magnitudes within each of the following International Telecommunication Union (ITU) standard frequency bands:

- Low Frequency (LF): 30kHz - 300kHz
- Medium Frequency (MF): 300kHz – 3MHz
- High Frequency (HF): 3MHz - 30MHz
- Very High Frequency (VHF): 30MHz - 300MHz

The measurements in these bands allow for differentiation of the asymmetries impact across the relevant RF spectrum and isolating areas of frequency interest such as the primary inverter switching frequency at 100kHz (LF), the ground plane current ringing frequency at 1.75MHz (MF) and switching edge rate harmonics (~30MHz). The spectral current magnitude can be calculated from the discrete LTspice export data per equation (2.3).

$$X(f) = \sum_{n=1}^{N} |x(f)|\Delta f \tag{2.3}$$

RMS CM and DM current data represents the singular response of all frequencies and is reported with the band data.

Once one or more filter imbalances are identified that can generate significant CM noise, these results can be used to intentionally induce CM signals in the EMI testbed of Figure 2.2. This technique will allow for evaluation of alternate PWM switching schemes with the goal of CM noise reduction. The key method to be evaluated in reducing the CM noise will be the use of asymmetric dead-times within the PWM switching scheme.

The full bridge topology in theory should generate no CM noise currents. Thus, selection of this topology allows for accurate control of the induced CM noise and optimum determination of mitigation affects. The induced CM currents were achieved by imposing asymmetries in the EMI filter connected between the source voltage and the inverter bridge, within the known tolerance ranges for the associated components. The key filter asymmetries used to achieve given CM current levels were evaluated and are highlighted in Table 2.2.

Success of overall CM reduction will be gauged by inspecting the RMS values of the base plate current compared to the baseline of balanced switching deadtimes. The spectral magnitudes

of these signals in the low frequency (LF), medium frequency (MF), high frequency (HF), and very high frequency (VHF) ranges were also recorded and observed.

The LTspice simulation environment which includes a single-phase full-bridge inverter EUT (Figure 2.3), was intended as the primary evaluation tool for the proposed research. However, excessive simulation time and difficulty to automate made LTspice unsuitable to evaluate the initial test matrix which exceeded over one-thousand unique test configurations.

This led to the development of an alternative simulation platform. Aaron Brovont [10] developed a common mode equivalent model (CEM) of the half bridge converter testbed (Figure 2.6).

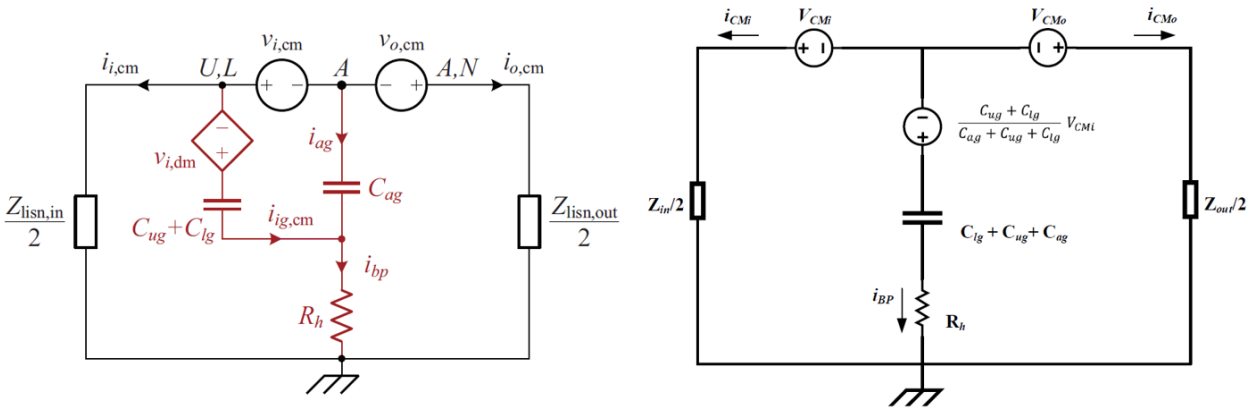

Figure 2.6 CEM for Half Bridge EUT [10] with Reduced Simulation Version on Right

The quantities Cug, Clg, and Cag are the upper, lower and A-node, parasitic capacitances respectively of the half bridge power module (Figure 2.1). The quantities V_{CMi} and V_{CMo} are the input and output driving voltages in the common mode which are defined below and $Z_{in/2}$ and $Z_{out/2}$ are the parallel combinations of the two input and the two output LISN impedances respectively.

$$v_{CMi} = \frac{1}{2}(v_{Q1} - v_{Q2}) \qquad v_{CMo} = \frac{1}{2}v_{AN} \approx \frac{1}{4}(v_{Q1} - v_{Q2}) \tag{2.4}$$

The baseplate current, i_{BP}, is the sum of the output and input LISN CM currents, i_{CMo} and $i_{CMi,}$ and is the primary figure of merit for this study.

The half bridge CEM model was simulated in MATLAB and shown to have exceptional agreement with the physical measured system. MATLAB provides many advantages over LTspice in simulation speed, automation, and data manipulation therefore a full bridge version of the CEM was developed for this study and is described below.

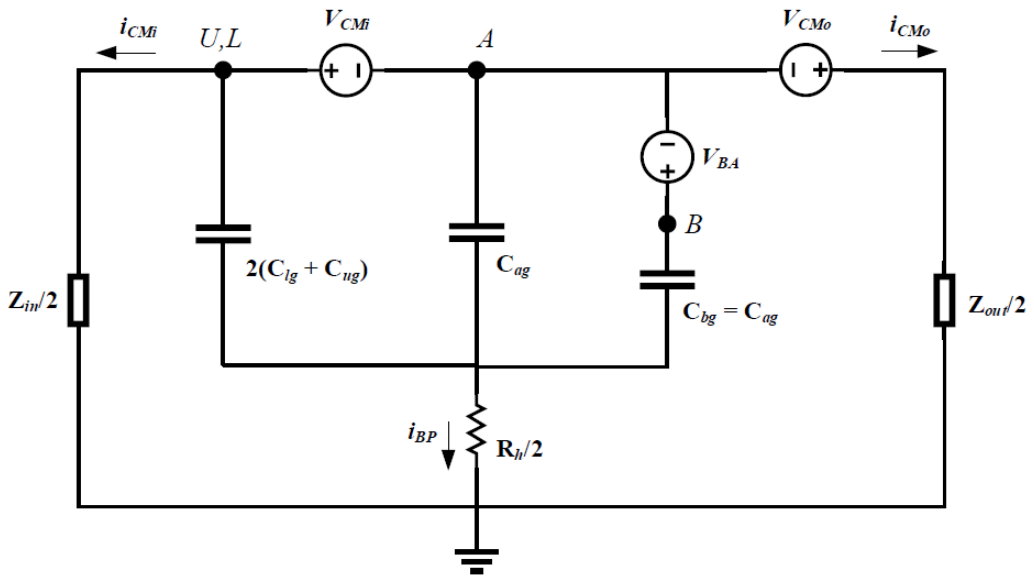

Figure 2.7 CEM for Full Bridge EUT – Before Simplification

The second power module of the full bridge adds a second, assumed identical, set of parasitics shown connected to Q3 and Q4 in Figure 2.2. To develop the full bridge CEM (Figure 2.7), the

upper and lower parasitic capacitances combine in parallel in the common mode while the B-phase parasitic is connected via an additional source V_{BA}.

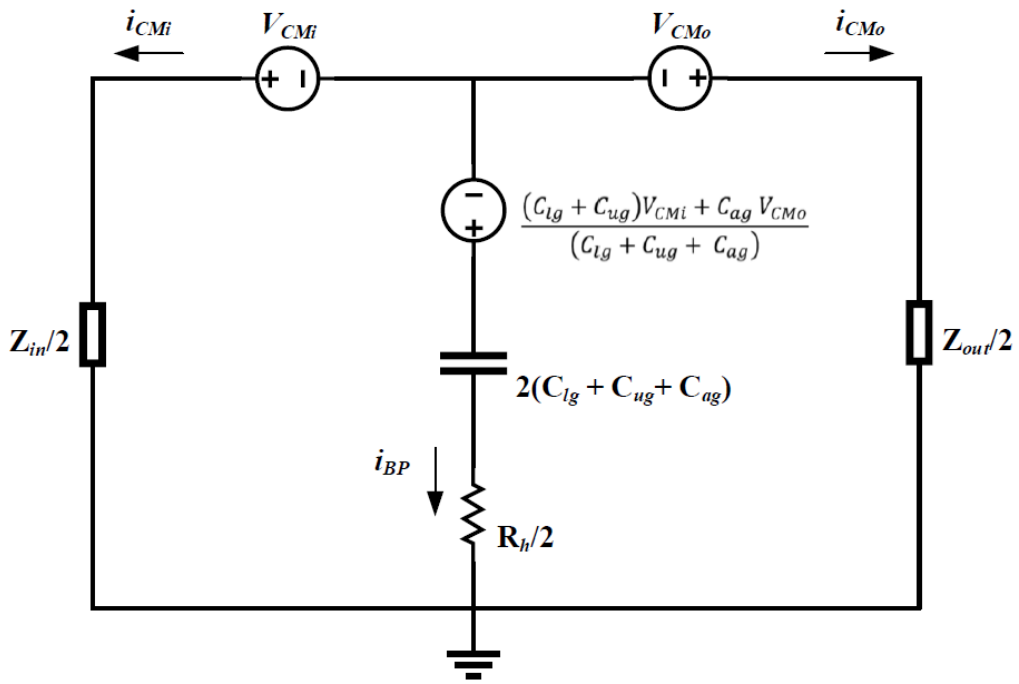

Figure 2.8 Simplified CEM for Full Bridge EUT

To take advantage of the prior MATLAB simulation modeling in [10] the full bridge CEM requires reduction in similar fashion as the half bridge. Applying Thevenin and Norton source transformations and the CM input and output voltage derivations below, the capacitor branches were reduced to an equivalent capacitance and series voltage source as shown in Figure 2.8. Differing from the half bridge, V_{CMo} is now a function of all switching voltages which will allow for control of all the deadtime parameters.

$$v_{AB} = -v_{Q1} + v_{Q3} = v_{Q2} - v_{Q4} \tag{2.5}$$

$$v_{AB} = -\frac{1}{2}\left(v_{Q1} - v_{Q2} - v_{Q3} + v_{Q4}\right) \tag{2.6}$$

$$v_{CMo} = \frac{1}{2}v_{AB} = \frac{1}{4}\left(v_{Q1} - v_{Q2} - v_{Q3} + v_{Q4}\right) \tag{2.7}$$

$$v_{CMi} = \frac{1}{2}\left(v_{Q1} - v_{Q2}\right) \tag{2.8}$$

The simulation models were constructed in MATLAB Simulink which was chosen for the straightforward construction of the four gate signals and for future implementation of closed loop control methods. A model of the half bridge system was first created to confirm the method produced agreement with the MATLAB model from [10] (Figure 2.9). Once functionality was validated, the full bridge converter model was built (Figure 2.10).

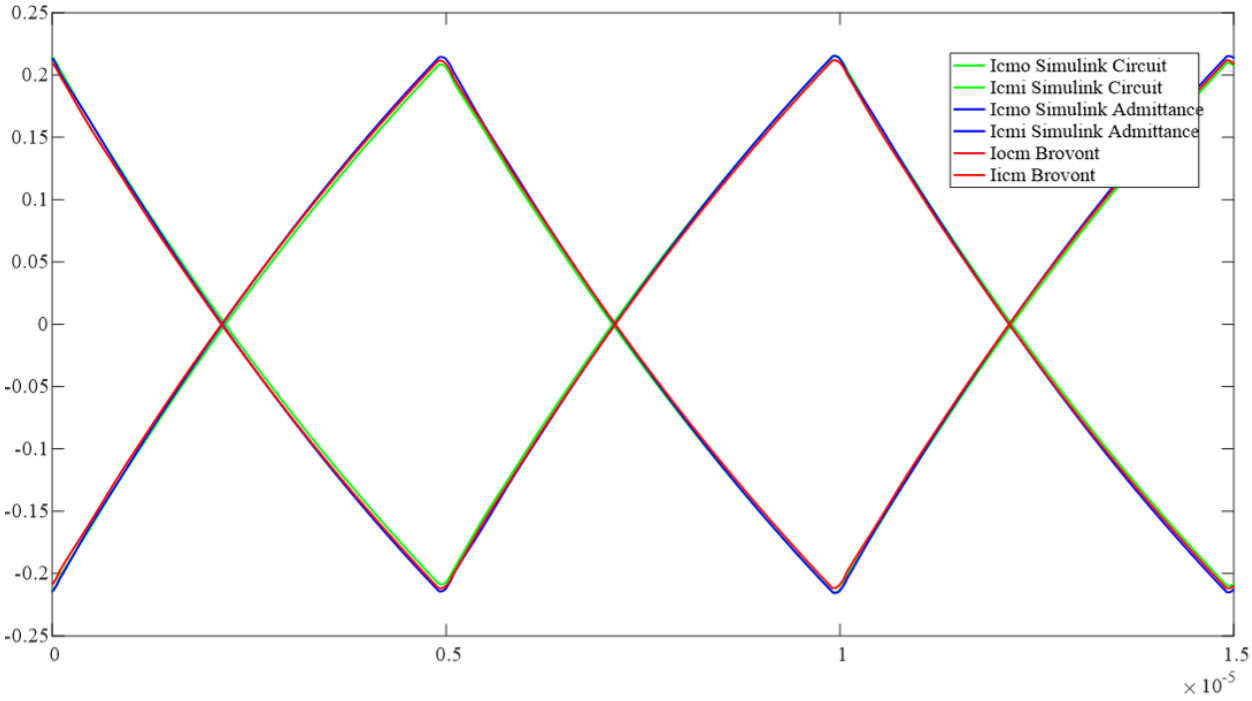

Figure 2.9 Simulink and m-script Agreement of i_{CMo}, i_{CMi}, and i_{BP} for Half Bridge CEM

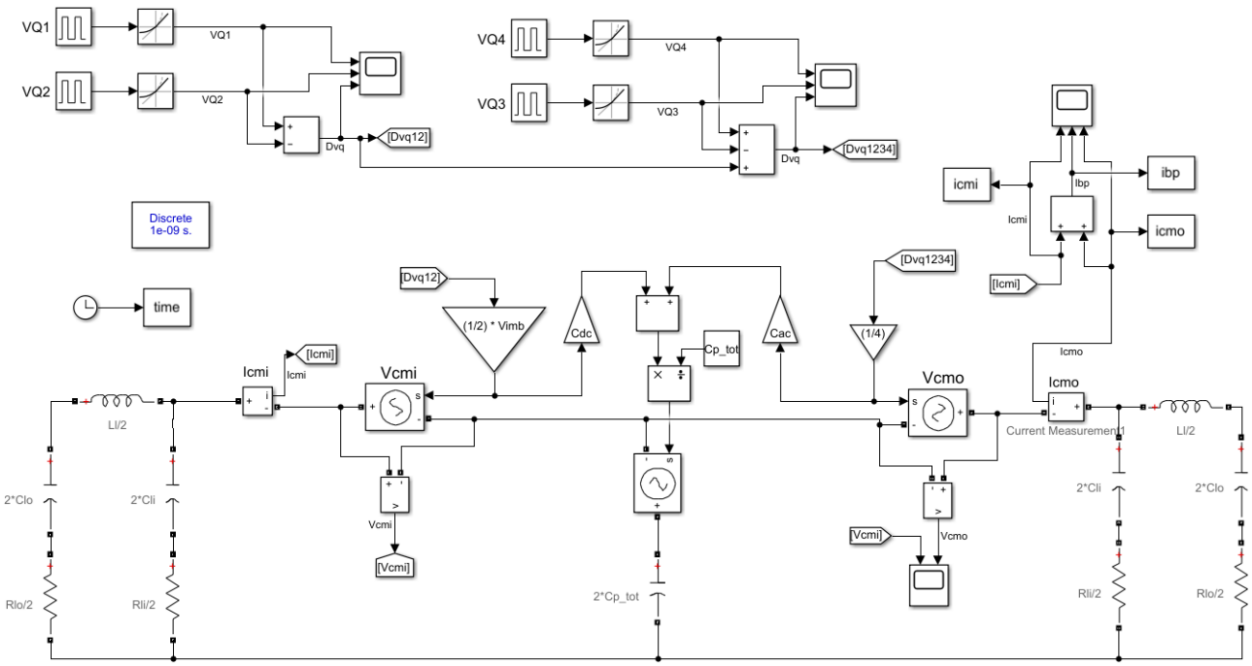

Figure 2.10 Full bridge CEM Simulink

The next necessary step was to introduce the EMI filter imbalance to the model. Based on the results of the imbalance study, which will be thoroughly discussed in the results section, the leakage imbalance produced the largest CM content making it the best choice for analysis. Aaron Brovont [10] developed an equivalent model for the leakage imbalance of a common mode choke which is introduced to the full bridge CEM highlighted in RED in Figure 2.11.

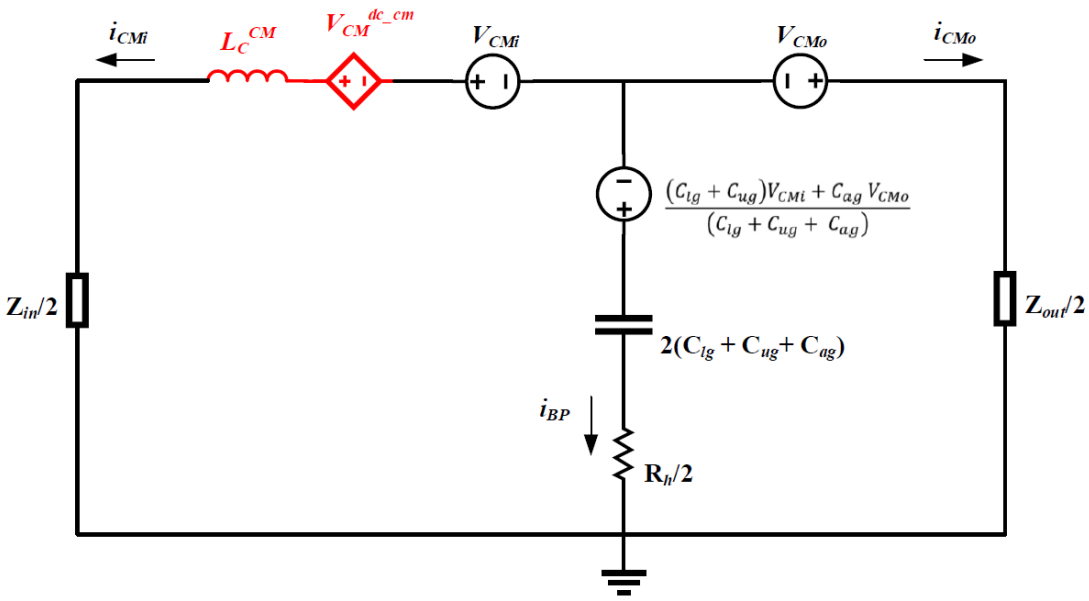

Figure 2.11 Full Bridge CEM with Leakage Imbalance

The leakage imbalance results in a voltage addition at the EUT input equating to the sum of the voltage drop across L_C^{cm} and $v_{CM}^{cm\rightarrow dm}$ which are defined as:

$$v_{CM}^{cm\rightarrow dm} = \frac{a}{2l}\Delta V_{dc} \tag{2.9}$$

$$L_C^{cm} = \left[m + \frac{(l+a)(l-a)}{2l}\right]\Delta L_C \tag{2.10}$$

Constants *m*, *l*, and *a* are the fractional mutual inductance, leakage inductance, and asymmetry factor. Specifically, the mutual inductance is $(m)L_C$ and the leakage inductance of each winding is $(l\text{-}a)L_C$ and $(l+a)L_C$. Adding the imbalance in this fashion adds new challenges in that V_{dc} is a variable quantity and does not exist in the CEM. Many attempts were trialed to artificially fabricate V_{dc} and to import LTspice data but neither produced correct results. After further consideration it was observed that the imbalance voltage can be approximated by adding a factor proportional to the input voltage V_{CMi}.

In a full bridge inverter there are four gate signals: Q1, Q2, Q3, Q4, shown in Figure 2.2. Subsequently, there are four deadtime parameters that can be varied, as identified graphically in Figure 2.12. In this study, these four parameters were individually and systematically cross-varied in pairs according to the test matrix which is included for review in the appendix. This full matrix of 141 test configurations was repeated for multiple duty cycles and filter imbalances for over 1000 data points. Simulation of this massive test matrix was only possible due to the automated and quick simulation time of the Simulink model and would not have been practical to complete in LTspice. Initially the deadtime magnitude was varied from 25ns to 200ns from the nominal 300ns of the test bed and was expanded to 1500ns after the initial results were evaluated.

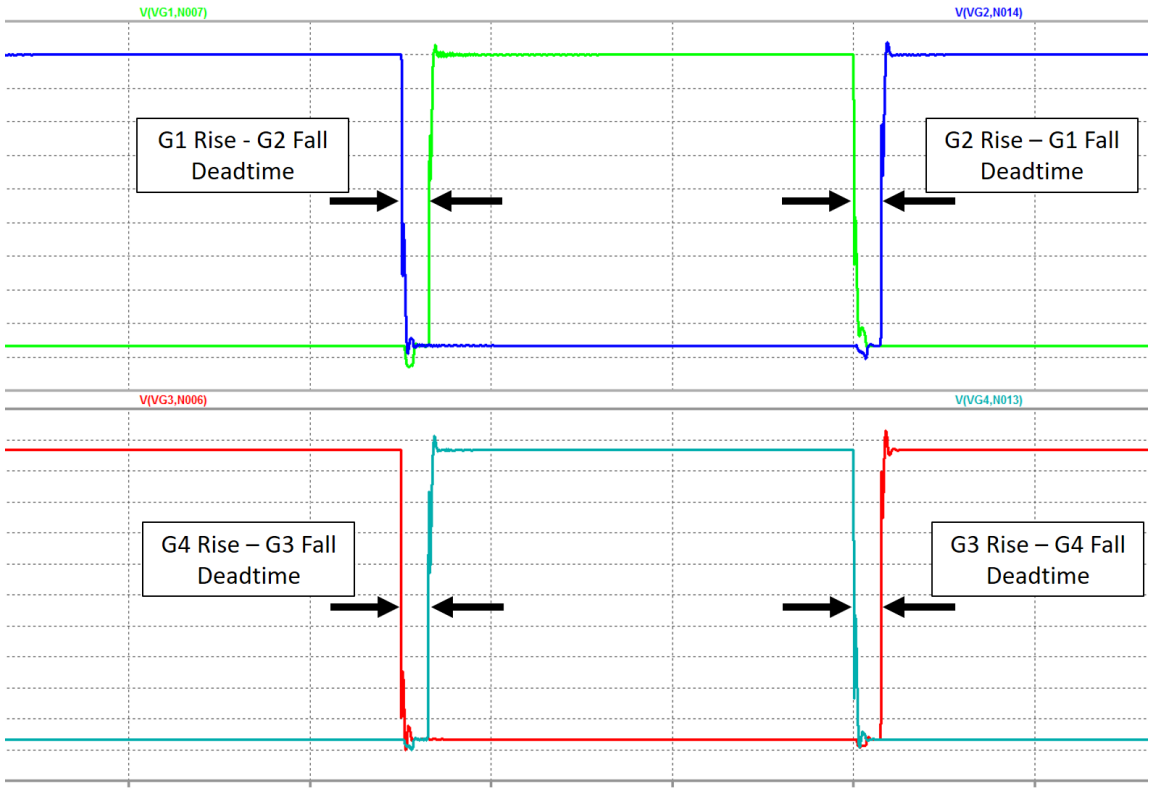

Figure 2.12 Switching Signals with Deadtime

2.3 Results

The results comparisons below are referred to the baseline performance of the system which is the EUT with the filter installed with all nominal component values and balanced parasitics. Table 2.4 shows the results matrix summary which ranks input CM and DM current significance for each test configuration and frequency band. Impact was assigned based on the magnitude change with respect to the balanced filter baseline as follows:

$$\text{High} \geq 66\%, \quad 66\% > \text{Medium} \geq 33\%, \quad \text{Low} < 33\%.$$

Table 2.4 tabulates the results providing a compact profile of the asymmetry sensitivities highlighting parameter settings with the most significant impact to CM and DM signals. The CM and DM performance is presented for each test run allowing the reader to observe the frequency response of every parameter change versus the baseline. The data is normalized and offset to the baseline permitting quantification of the impact of each parameter change.

Table 2.4 EMI Filter Imbalance Results Matrix

															CMin Response					DMin Response					
Run	L1 (mH)	L1-ls (µH)	L1-ESR (mΩ)	L1-EPC (pF)	L2 (mH)	L2-ls (µH)	L2-ESR (mΩ)	L2-EPC (pF)	Cy1 (pF)	Cy1-ESR (mΩ)	Cy1-ESL (nH)	Cy2 (pF)	Cy2-ESR (mΩ)	Cy2-ESL (nH)	RMS	LF	MF	HF	VHF	RMS	LF	MF	HF	VHF	Comments
Baseline2	5.1	23	30	15	5.1	23	30	15	2200	20	5	2200	20	5											Baseline w/ parasitics
1	5.25	23	30	15	5.1	23	30	15	2200	20	5	2200	20	5	L	L	L	L	L	M	L	L	L	L	Max inductance imbalance high DC+
2	5.15	23	30	15	5.1	23	30	15	2200	20	5	2200	20	5	L	L	L	L	L	L	L	L	L	L	Mid inductance imbalance high DC+
3	5.05	23	30	15	5.1	23	30	15	2200	20	5	2200	20	5	L	L	L	L	L	L	L	L	L	L	Mid inductance imbalance low DC+
4	4.95	23	30	15	5.1	23	30	15	2200	20	5	2200	20	5	H	M	M	M	M	M	L	L	L	L	Max inductance imbalance low DC+
5	5.1	23	30	15	5.25	23	30	15	2200	20	5	2200	20	5	L	L	L	L	L	M	L	L	L	L	Max inductance imbalance high DC-
6	5.1	23	30	15	5.15	23	30	15	2200	20	5	2200	20	5	L	L	L	L	L	L	L	L	L	L	Mid inductance imbalance high DC-
7	5.1	23	30	15	5.05	23	30	15	2200	20	5	2200	20	5	L	L	L	L	L	L	L	L	L	L	Mid inductance imbalance low DC-
8	5.1	23	30	15	4.95	23	30	15	2200	20	5	2200	20	5	H	M	L	L	L	M	L	L	L	L	Max inductance imbalance low DC-
9	5.1	23	30	15	5.1	23	30	15	2640	20	5	2200	20	5	L	L	L	L	L	L	L	L	L	L	Y-Cap DC+ tolerance value (+20%)
10	5.1	23	30	15	5.1	23	30	15	2420	20	5	2200	20	5	L	L	L	L	L	L	L	L	L	L	Y-Cap DC+ tolerance value (+10%)
11	5.1	23	30	15	5.1	23	30	15	1980	20	5	2200	20	5	L	L	L	L	L	L	L	L	L	L	Y-Cap DC+ tolerance value (-10%)
12	5.1	23	30	15	5.1	23	30	15	1760	20	5	2200	20	5	L	L	L	L	L	L	L	L	L	L	Y-Cap DC+ tolerance value (-20%)
13	5.1	23	30	15	5.1	23	30	15	2200	20	5	2640	20	5	L	L	L	L	L	L	L	L	L	L	Y-Cap DC- tolerance value (+20%)
14	5.1	23	30	15	5.1	23	30	15	2200	20	5	2420	20	5	L	L	L	L	L	L	L	L	L	L	Y-Cap DC- tolerance value (+10%)
15	5.1	23	30	15	5.1	23	30	15	2200	20	5	1980	20	5	L	L	L	L	L	L	L	L	L	L	Y-Cap DC- tolerance value (-10%)
16	5.1	23	30	15	5.1	23	30	15	2200	20	5	1760	20	5	L	L	L	L	L	L	L	L	L	L	Y-Cap DC- tolerance value (-20%)
17	5.1	23	30	15	5.1	23	30	15	2640	20	5	1760	20	5	L	L	L	L	L	L	L	L	L	L	Y-Caps max tolerance spread (2x20%), DC+ high
18	5.1	23	30	15	5.1	23	30	15	1760	20	5	2640	20	5	L	L	L	L	L	L	L	L	L	L	Y-Caps max tolerance spread (2x20%), DC- high
19	5.1	23	30	15	5.1	23	15	15	2200	20	5	2200	20	5	L	L	L	L	L	H	M	M	M	M	ESR imbalance +0.15
20	5.1	23	15	15	5.1	23	30	15	2200	20	5	2200	20	5	L	L	L	L	L	H	M	M	M	M	ESR imbalance -0.15
21	5.1	23	30	0	5.1	23	30	15	2200	20	5	2200	20	5	L	L	L	L	L	L	L	L	L	L	L1 0 EPC
22	5.1	23	30	15	5.1	23	30	0	2200	20	5	2200	20	5	L	L	L	L	L	L	L	L	L	L	L2 0 EPC
23	5.1	0	30	15	5.1	23	30	15	2200	20	5	2200	20	5	L	H	H	H	H	L	M	M	M	M	L1 0 leakage
24	5.1	23	30	15	5.1	0	30	15	2200	20	5	2200	20	5	L	H	H	H	H	L	M	M	M	M	L2 0 Leakage
25	5.1	23	30	15	5.1	23	30	15	2200	0	5	2200	20	5	L	L	L	L	L	L	L	L	L	L	Cy1 0 ESR
26	5.1	23	30	15	5.1	23	30	15	2200	20	5	2200	0	5	L	L	L	L	L	L	L	L	L	L	Cy2 0 ESR
27	5.1	23	30	15	5.1	23	30	15	2200	20	0	2200	20	5	L	L	L	L	L	L	L	L	L	L	Cy1 0 ESL
28	5.1	23	30	15	5.1	23	30	15	2200	20	5	2200	20	0	L	L	L	L	L	L	L	L	L	L	Cy2 0 ESL
29	5.25	23	30	15	5.1	23	30	15	2640	20	5	1760	20	5	L	L	L	L	L	M	L	L	L	L	Combined L imbalance, cap tolerance worst case DC+
30	5.1	23	30	15	5.25	23	30	15	1760	20	5	2640	20	5	L	L	L	L	L	M	L	L	L	L	Combined L imbalance, cap tolerance worst case DC-
31	5.1	23	30	15	5.25	23	30	15	2640	20	5	1760	20	5	L	L	L	L	L	M	L	L	L	L	Combined L imbalance, cap tolerance offsetting DC+
32	5.25	23	30	15	5.1	23	30	15	1760	20	5	2640	20	5	L	L	L	L	L	M	L	L	L	L	Combined L imbalance, cap tolerance offsetting DC-

Tests 23 and 24 yielded the most significant CM impact of all configurations. These two tests toggle the choke leakage inductance on either branch from 23uH to 0 and produce the most significant results of the study. Test 23 sets the DC+ leakage inductance to 0 and the DC- leakage to the maximum of 23uH while test 24 is the converse of the same imbalance magnitude. The CM current increases substantially in magnitude in each frequency band and are the only tests to exhibit a high impact per the evaluation criteria.

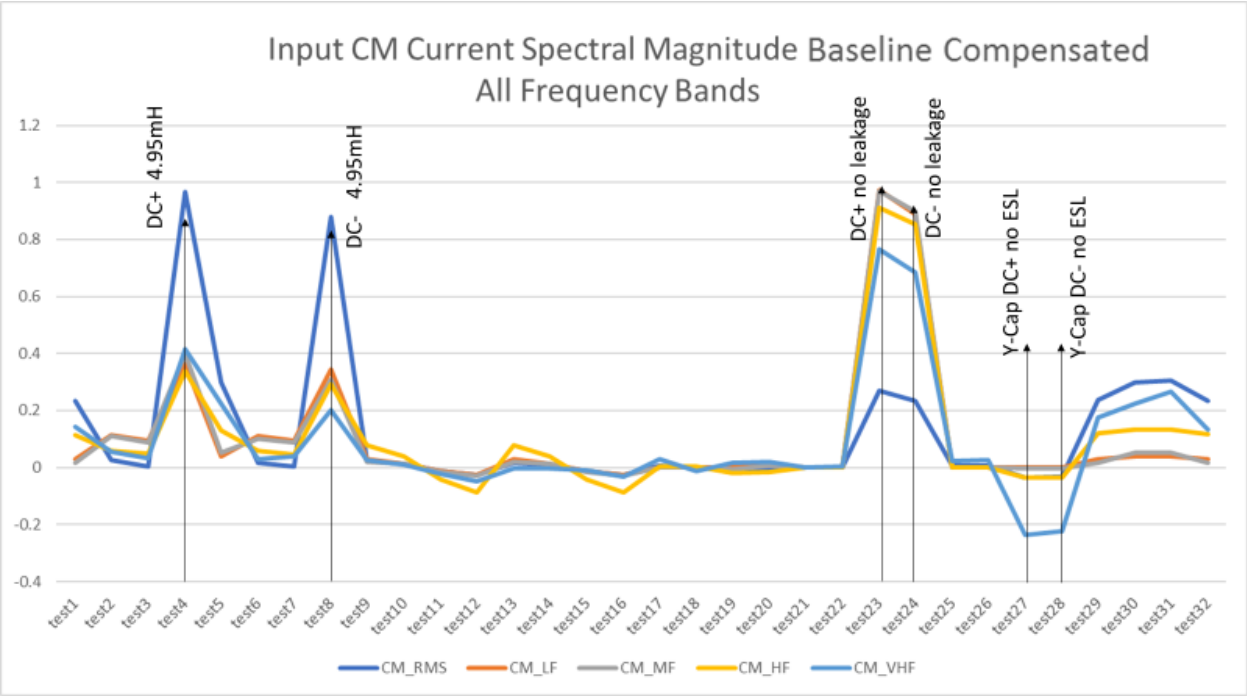

Figure 2.13 Input CM Current Spectral Magnitude at All Frequency Bands

Figure 2.13 plots the CM spectral current magnitude versus test configuration for each frequency band. The data is baseline compensated meaning a zero value on the y-axis is equivalent to the baseline performance. The CM increase for tests 4, 8, 23, and 24. This graph also allows these increases to be quantified. For example: in test 4 the CM current magnitude increased

approximately 40% more than baseline due to the -0.15mH imbalance in choke inductance on the DC- branch for all frequency bands. Figure 2.13 also shows that the CM RMS trends with the frequency bands which is expected as it is a convolution of all frequencies.

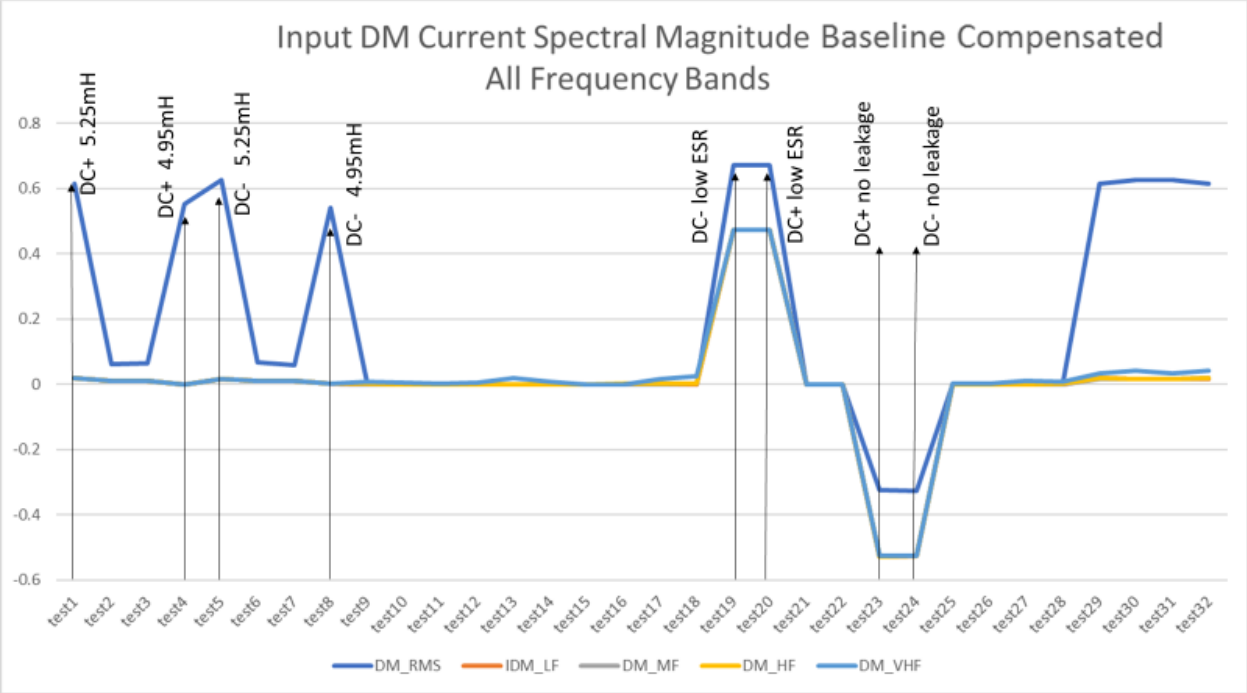

Figure 2.14 Input DM Current Spectral Magnitude at All Frequency Bands

In the DM frequency band plot of Figure 2.14, there is no observable change from baseline in response in the four frequency bands (LF, MF, HF, and VHF) until test 19 and 20 where the ESR is lowered on each branch generating a subsequent increase in DM current. Most importantly the observations of tests 23 and 24 are confirmed. The DM magnitude for each band is reduced approximately 50% from decreasing the leakage inductance by the same 50% (recall that test 23 and 24 eliminate the leakage in one of the branches reducing the total leakage in the DM path by half). This behavior is clear in all data sets and opposes often documented claims that CM choke

leakage inductance attenuates DM signals [9], [5], [6]. It was first thought the parasitic capacitance paths to the ground return allowed for this contradiction. Simulations with all capacitive paths to ground removed continued to exhibit this behavior. The DM RMS trends with the frequency bands similar to CM but is more responsive to the inductance imbalances which will be discussed further in the next section.

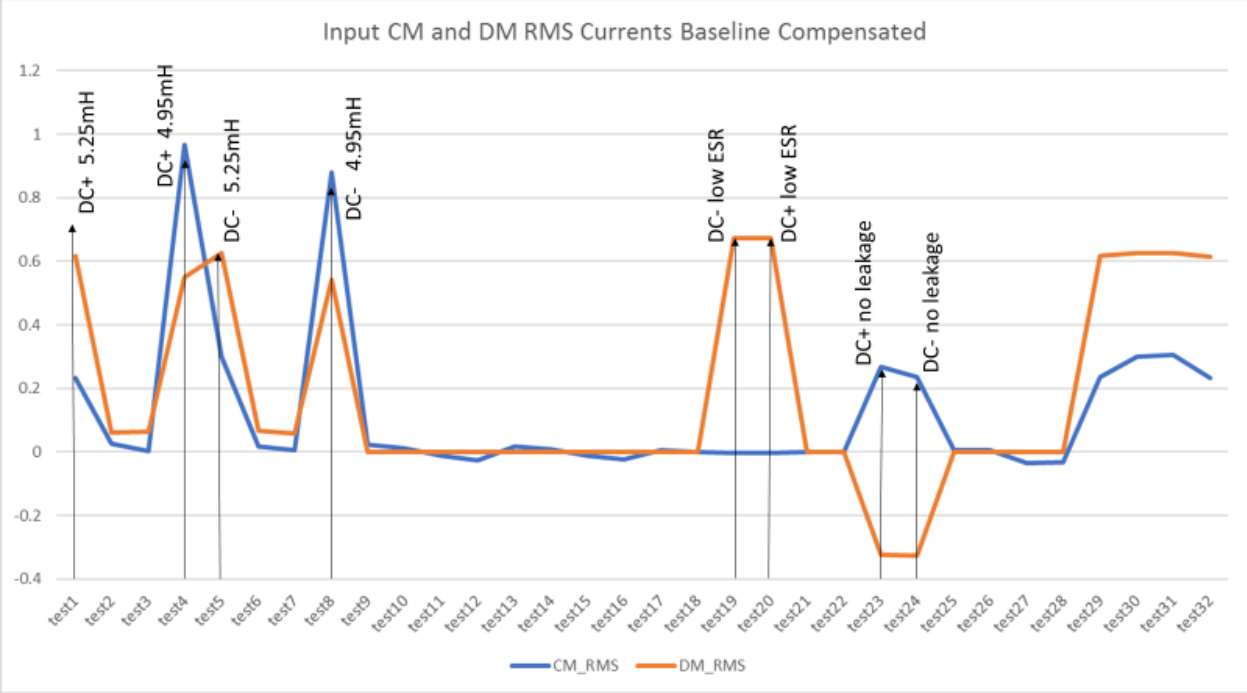

Figure 2.15 RMS CM and DM Currents Compensated to Baseline

Figure 2.15 overlays the CM and DM RMS responses. Notably it shows that the inductance imbalances (tests 1, 4, 5, and 8) cause the CM and DM to trend together which is not in agreement with proposals of CM to DM conversion [5], [6], [7]. However, the CM to DM conversion is present for the leakage imbalances of tests 23 and 24. This suggests that CM to DM conversion is conditional to the source of the signal.

Reviewing the MATLAB output of the initial test matrix identified which deadtime asymmetry configurations (if any) produced reductions in CM noise generate from the filter leakage imbalance. This initial exploratory data did find apparent reductions and highlighted they occurred only when the deadtimes were shifted in their bipolar pairs (Q1-Q4 or Q2-Q3 as shown in Figure 2.16). Further study of the results showed shifting either pair produced identical results as did shifting forward or backward when either was done in equal increments of time. This first set of results narrowed the scope of the number of overall test configurations allowing an increase of resolution of deadtime from 25ns to 1500ns and duty cycle from 35% to 49%. This large increase in resolution produced a better understanding of how much reduction can be achieved. Since the model is approximating the voltage imbalance, this parameter was also swept across a wide range (2.5 to 12 peak VDC).

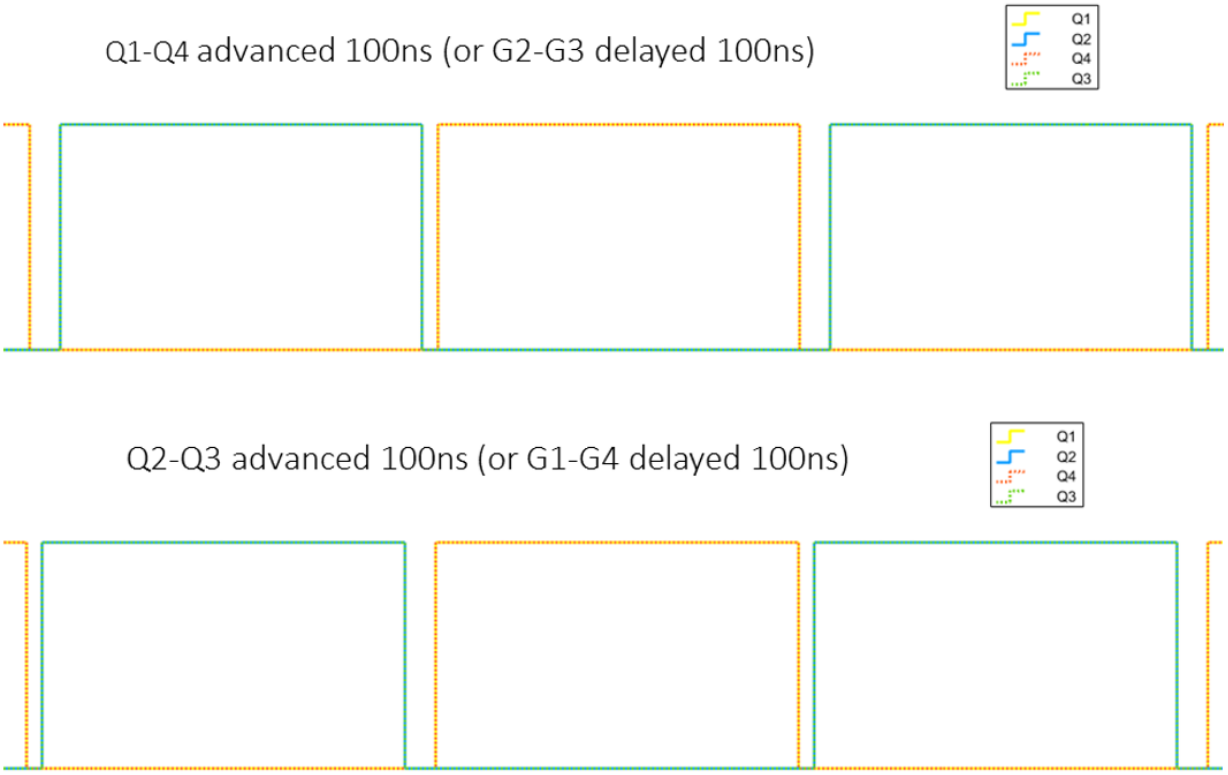

Figure 2.16 Gate Signal Shifting in Bipolar Pairs

The second round of focused MATLAB simulations are plotted in Figure 2.17 which shows percent reduction vs increasing deadtime. Interestingly, iterating voltage imbalance and duty cycle produce equivalent results as shown by the single MATLAB curve of the plot which effectively reduced the unique data points to eighteen. This characteristic made it possible to acquire the LTspice data which before was impractical for the hundreds of iterations given each simulation run takes 45 minutes. The LTspice simulations were performed and are also included in Figure 2.17.

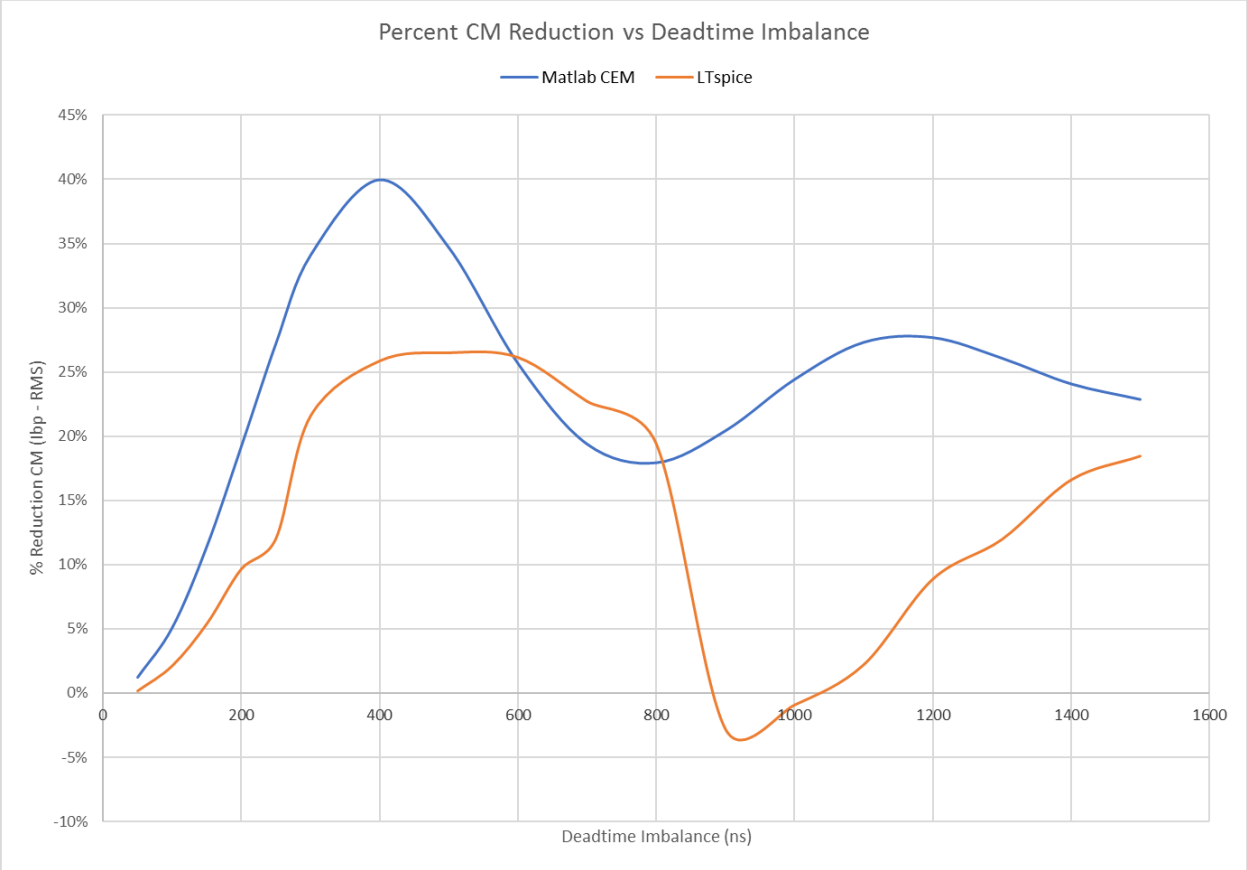

Figure 2.17 Reduction Results Plot: MATLAB vs LTspice

The Simulink results did identify the general reduction trend allowing the targeted LTspice simulations to be performed. Given that LTspice results have been validated empirically with the physical test bed (Figure 2.18), it is shown in Figure 2.17 that reductions seeming to exceed 25% can be achieved. However, further study of the raw data proved that the reductions are localized in frequency ranges and the total CM content was not altered.

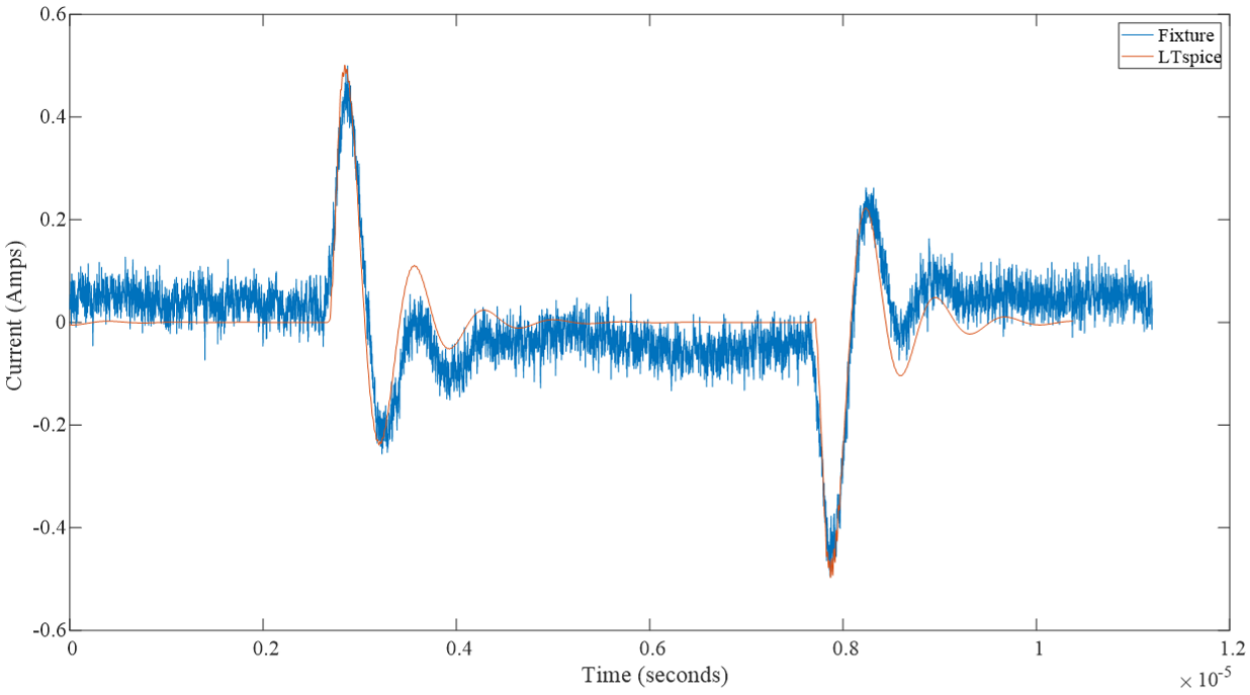

Figure 2.18 Half Bridge: LTspice and Physical Fixture Base Plate Current Agreement

The primary intent of this effort was to profile the sensitivities of EMI filter asymmetries and produce a toolset that can be used for follow-on studies for EMI analysis, particularly for inverter topologies like that of Figure 2.1 and Figure 2.2. This was accomplished with the outputs of Table 2.4 and the simulation tool of Figure 2.10.

The key results of this study are:

1) Leakage inductance imbalances generate significant CM currents in topologies similar to Figure 2.2
2) Asymmetric deadtime switching does NOT reduce total CM content, however it can redistribute CM to different frequency ranges resulting in localized reductions.
3) Developed significant simulation models for converter topologies used in follow on studies.

CHAPTER III

METHOD FOR MEASURING SINGLE PHASE LINE IMPEDANCE

3.1 Proposed Analytical Methods

Chapter 3 material is published: IEEE APEC 2022, March 2022 (ref. section 5.2)

Line impedance quantification has been historically difficult to achieve straightforwardly or with high accuracy. There are few commercially available instruments capable of measuring line impedance prompting many engineers to rely on estimations, calculations, or alternate measurement methods [18]. Other instrumentation capable of measuring line impedance is intended to mitigate and correct power quality making the equipment costly and superfluous for this dedicated task [14], [15]. Techniques using a purely resistive load would require a high wattage and impractical load resistor to generate the high current needed for accurate results or the addition of complex and costly switching circuitry to generate a momentary significant load current [14], [17], [18]. Attempting to measure the line resistance with a low current would result in a low signal-to-noise ratio (SNR) and poor accuracy. It is important to maintain optimum SNR as some environments, particularly commercial and industrial, may exhibit high noise content in the measured signals contributing to significant metrology errors. For example, 1V of signal noise infused on a 120VAC signal can produce 10% or more incremental error in the calculated line impedance if low current measurements are utilized.

The procedure here-in describes a novel technique to measure line impedance of a common residential or commercial 60Hz, 120V AC mains, utilizing a capacitor as the load to produce the

measurement parameters. An uncharged capacitor will act as a short circuit when initially energized, drawing maximum current as the AC line voltage is applied near peak value. This method to quantify line impedance of a single-phase power feed requires only three inexpensive, common lab components: an oscilloscope and a pair of differential probes or current clamp.

3.2 Approach

This practical approach to measuring elusive line impedance places a switch, a rectifying diode, and a large load capacitor in series as shown in Figure 3.1. Since an uncharged capacitor is a short circuit upon initial energization, a very large current results if the AC line voltage is applied near peak value. A resistor load will sustain a continuous current for the duration the switch is closed while the capacitor will stop conducting current once fully charged due to the rectification diode. The diode will permit the capacitor to charge in one polarity in few cycles, which will resolve the need for a high wattage component or complex switching circuitry. At energization, the current will be a very large impulse creating a large voltage drop (sag) across the line and source resistances which is important to optimize accuracy as it will maximize scale usage for the oscilloscope measurement and signal-to-noise ratio (SNR). In fact, the uncharged capacitor load will produce nearly maximum current and voltage sag magnitudes as it will effectively "short circuit" the AC mains at the time of switch closure. To achieve a similar response with a purely resistive load would require a small resistance similar to the ESR of the capacitor accompanied with complex and costly switching logic components. Since the resistor load would conduct continuously, intelligent switching logic would need to be incorporated that would duty cycle limit energization to achieve a similar response the capacitor load provides inherently.

Figure 3.1 shows the equivalent circuit of the line impedance and measurement circuit. The quantities R_S, L_S, and C_S are the resistance, inductance, and capacitance of the voltage source and

line feed. The quantity R_S represents the line and source resistance in series with the AC mains which for these experiments is a 120VAC, 60Hz, residential service. The right-hand side of the circuit is the load where *SW* is the energization switch, L_P is the parasitic inductance of the measurement circuit, C_{LOAD} is the load capacitance, and R_{ESR} is the load capacitor equivalent series resistance.

It is noted that environmental factors, specifically ambient temperature and wire self-heating, can influence resistance measurements. The ambient temperature can be easily compensated by adjusting the measurement result knowing the temperature coefficient of the wire material (for copper wire the temperature coefficient is 0.393% per degree Celsius). The proposed measurement method will impose negligible self-heating given it is a singular pulse and near zero continuous current. However, the designer will need to account for or remove other possible loadings on the circuit that may cause relevant self-heating.

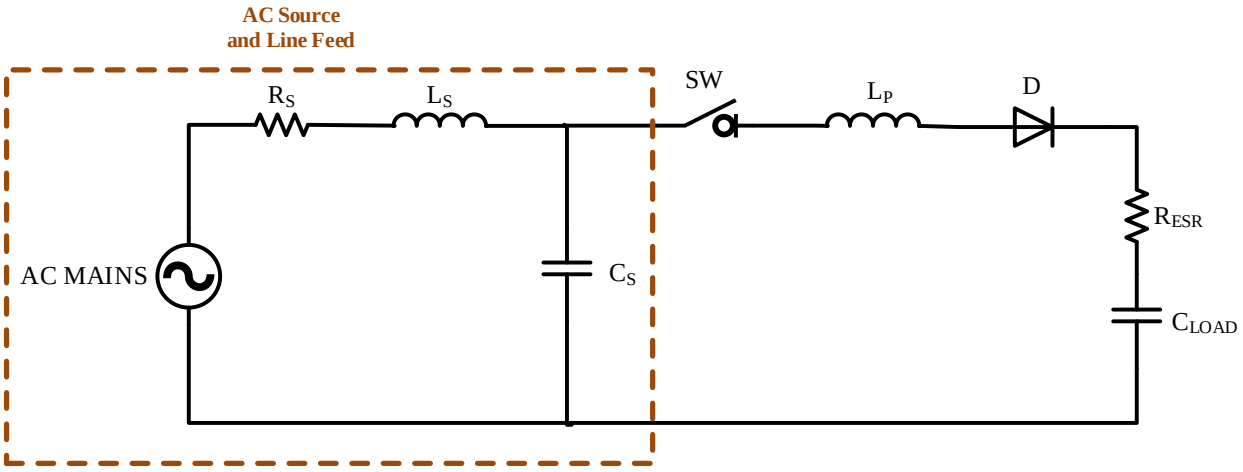

Figure 3.1 Equivalent Circuit of Residential Line Feed Including Impedance Measurement Components

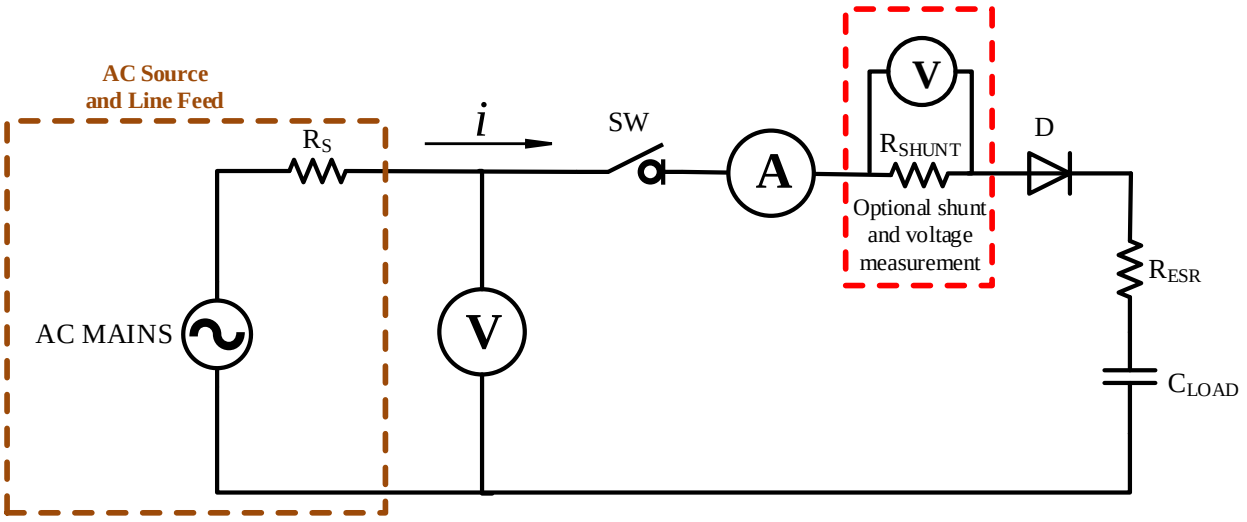

Figure 3.2 Simplified Equivalent Circuit of Line Impedance Measurement Method Using Capacitor Load

Since L_S and L_P are very small and C_S is negligibly small compared to the load capacitor, the model can be reduced to the circuit shown in Figure 3.2. C_{LOAD} is effectively a short circuit if discharged. When SW is closed a large current limited only by $R_S + R_{ESR}$ flows to charge the capacitor. The voltage observed by the scope in Figure 3.3 will show the sag or dip due to the $i \cdot R_S$ drop. The voltage dip (Δv) and current impulse (i_{pk}) captured on the oscilloscope can be used to calculate R_S by the following relationship:

$$R_S \cong \frac{\Delta v}{i_{pk}} \tag{3.1}$$

Best SNR is achieved when the circuit is switched closest to peak voltage. This will produce the largest current peak and associated voltage sag resulting in the best resolution for the line resistance calculation. Likewise, the load capacitor should be chosen for optimal current measurement as a small capacitance will reduce the current impulse duration, possibly making the

measurement more difficult. Care should be taken to be within the limits of the measurement instruments. As stated previously, the voltage dip (Δv) is the $i \cdot R_S$ drop. Similarly, the minimum voltage during the sag event is the $i \cdot R_{ESR} + v_D$ drop.

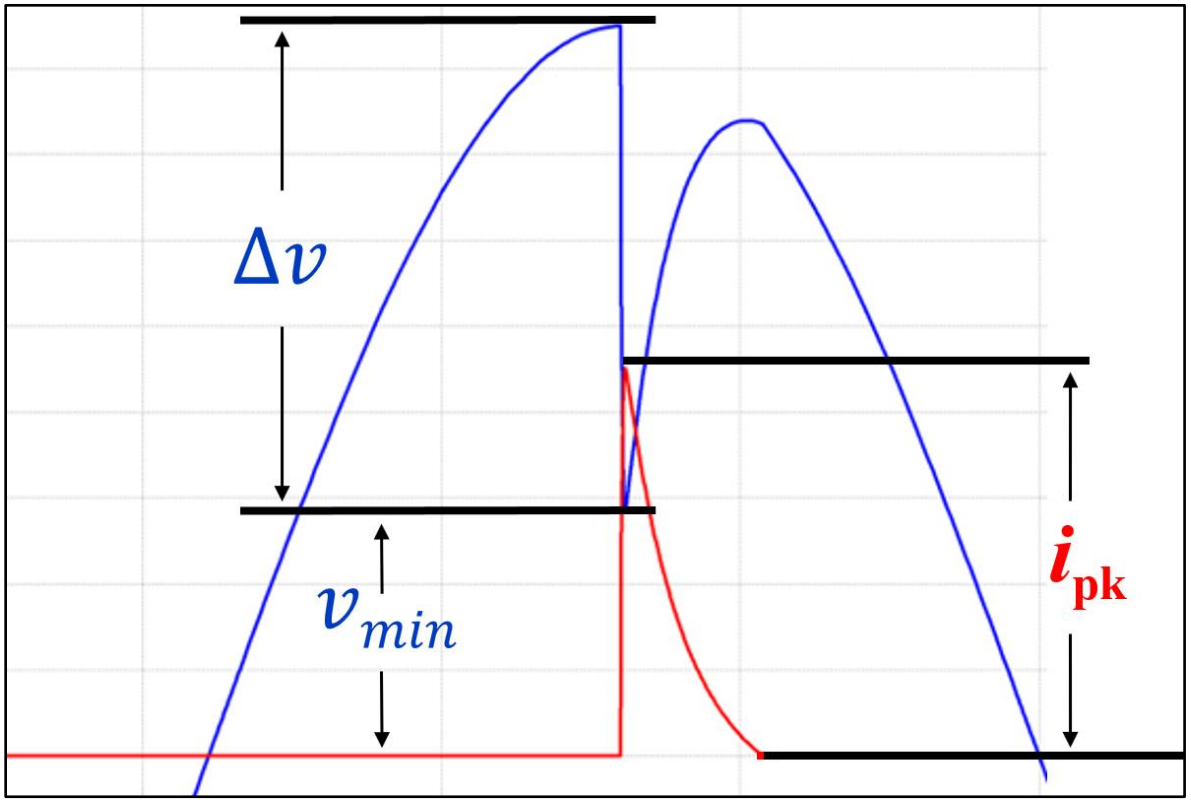

Figure 3.3 Voltage (blue) and Current (green) Observed at Switch Close Event

$$R_{ESR} \cong \frac{v_{min} - v_D}{i_{pk}} \tag{3.2}$$

Thus, the ESR of the capacitor can be calculated via equation (3.2) with the peak $i \cdot R_{ESR} + v_D$ obtained from the measurement in Figure 3.3 and if desired compared against the capacitor manufacturer datasheet. If a shunt resistor is employed, this would need to be considered in the calculation per equation (3.3):

$$v_{S\cdot pk} = \Delta v + v_{SHUNT\cdot pk} + v_{ESR\cdot pk} + v_{D\cdot pk} \quad (3.3)$$

Alternatively, the diode could be omitted, and the electrolytic capacitor could be replaced with a film capacitor such as one that is used for motor run/starting. The issue this method poses is the sizeable capacitance required for high current impulse, and voltage sag would continue to pull large RMS currents until the switch is re-opened. This detail would have to be managed.

A shunt resistor can be inserted in the circuit to perform the amperage measurement with the shunt voltage drop being measured with a differential probe as described in Figure 3.2. Otherwise, a current clamp would be utilized in place of a shunt for the current measurement. Considerations when choosing the current measurement method should include the quality of probes and shunts available, and the practicality and necessity of adding series resistance with the insertion of a shunt in the circuit under test. One such consideration is the circuit breaker characteristics protecting of the line feed being measured. Figure 3.4 shows the trip curve of a common residential circuit breaker [9]. The x-axis is multiples of breaker current rating and the y-axis is time to trip in seconds displayed on logarithmic scales. It can be observed on the trip curve in Figure 3.4 that the instantaneous trip region begins at 6 times the breaker rating. For a common residential 20A circuit this would equate to 120A-RMS or 170A peak indicating current peaks in this range will present the risk of tripping the circuit breaker. In cases where the margin to engaging these protective devices is inadequate, a shunt resistor can be added to mitigate this event as shown in Fig 3.2.

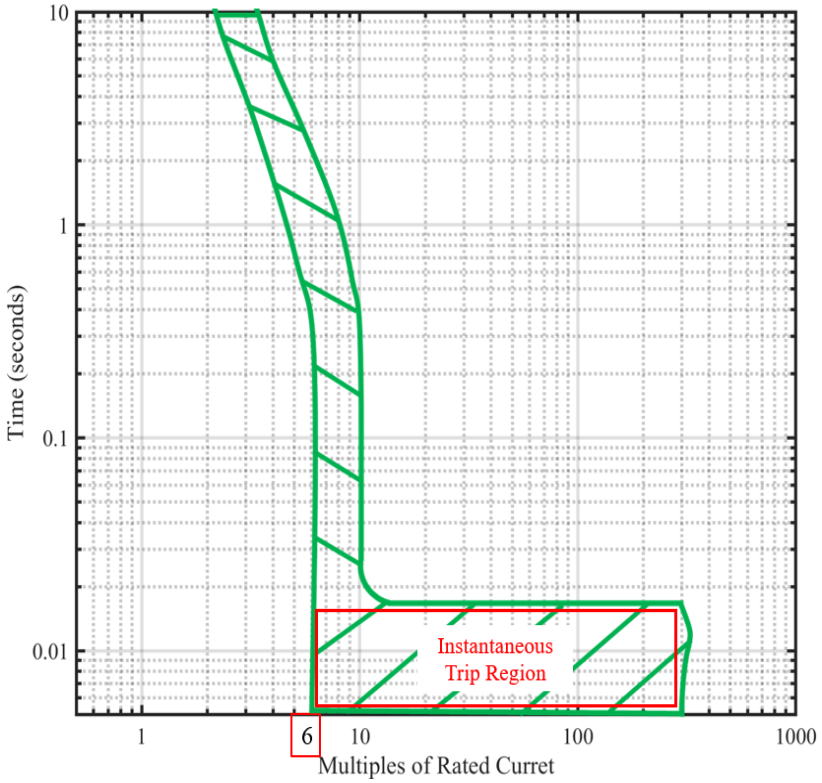

Figure 3.4 Square 'D' Trip Curve for QO Circuit Breaker Series

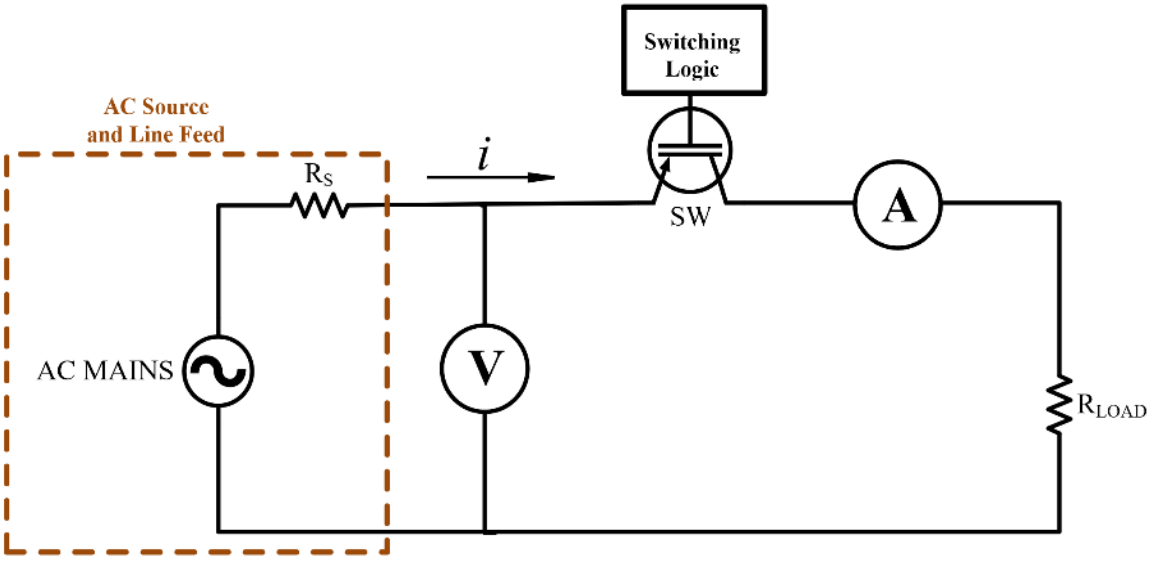

Figure 3.5 Alternate Line Impedance Measurement Method using Resistive Load with Duty Cycle Switching

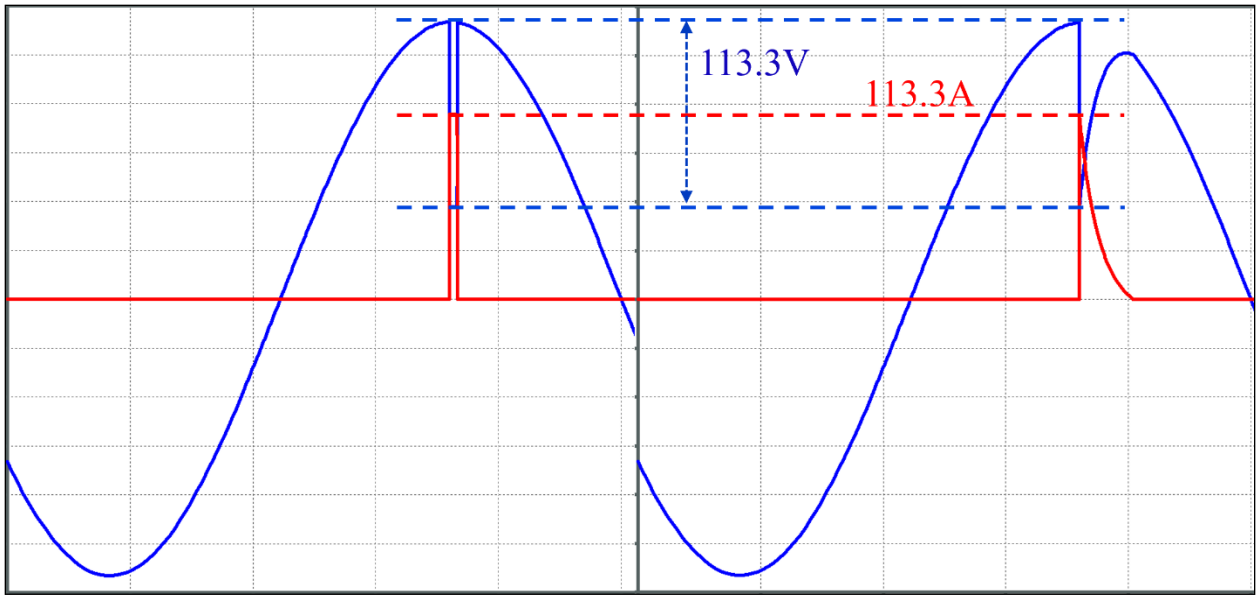

Figure 3.6 LTspice simulation: Voltage (blue) and Current (red). Left: Resistor Load with Duty Cycle Switching and Right: Capacitor Load with Simple Switching

3.3 Results

Both the capacitive load with simple switching of Figure 3.2 and the pure resistive load using duty cycle switching of Figure 3.5 were constructed and simulated in LTspice with a test line impedance of 1Ω. For the resistive method R_{LOAD} was set equal to the R_{ESR} simulation value 0.5 Ω allowing for direct comparison. Figure 3.6 shows the resulting voltage (blue) and current (red) measurements. Both methods produce identical voltage sags of 113.3V and a peak current pulse of 113.3A yielding the correct line impedance value of 1 Ω. The maximum duty cycle on-time for the resistive method would need to be adjusted to accommodate appropriate power delivery per the wattage rating of the selected load resistor. Likewise, consideration would also need to be given to select an appropriate minimum duty cycle on-time based on measurement system frequency response and capacitive and inductive system parasitics impacting signal rise times.

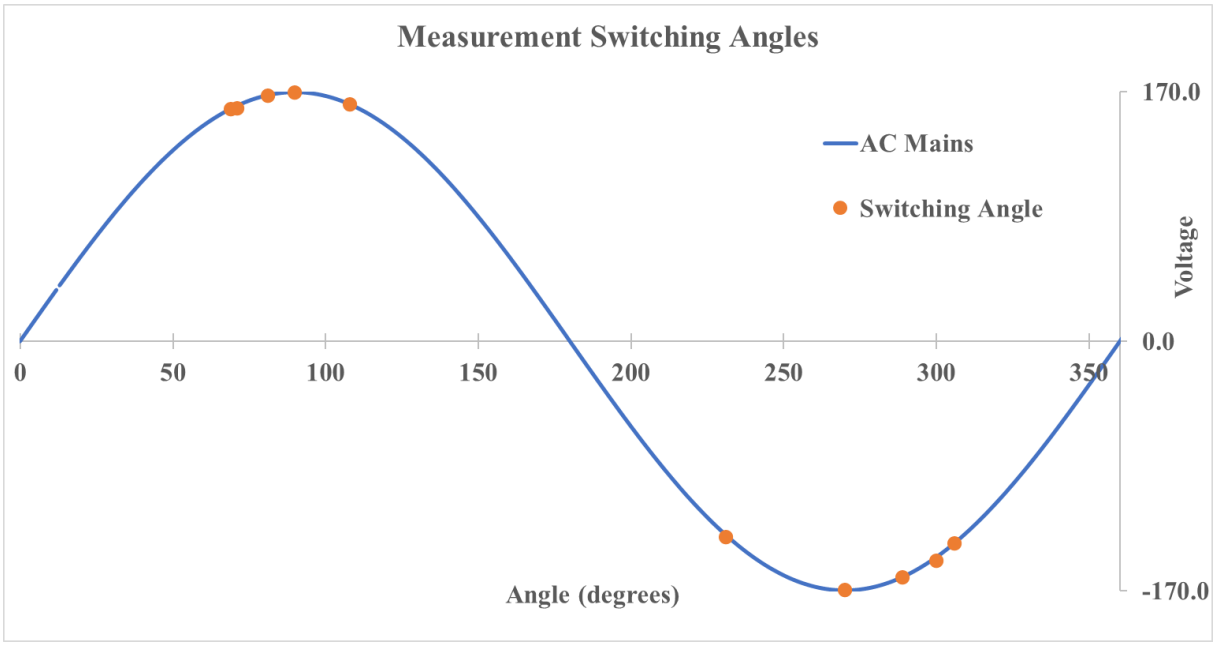

Figure 3.7 Measurement Switching Distribution

The circuit in Figure 3.2 was constructed and tested on a 120VAC, 20A, feed representative of a typical residential power circuit. Table 3.2 shows the list of measurement equipment and operating conditions for which the experiments were conducted. A load capacitance of 820μF was chosen to produce adequate current impulse durations, approximately 2ms, for measurement purposes. For the first experiment, both current clamp and shunt resistor methods were tested simultaneously for ten repetitions with the line impedance calculations and comparative results shown in Table 3.1. The data exhibits good agreement with the clamp method yielding an average line impedance of 0.764Ω and the shunt method yielding an average line impedance of 0.762Ω. The standard deviations are 0.033Ω and 0.024Ω with ranges of 0.717Ω to 0.819Ω and 0.731Ω to 0.797Ω respectively for the clamp and shunt data. The average of the percent differences for all ten measurements is 2.5% with a range of 0.5% to 5.3%. It is also important to note the

switching angle distribution shown in Figure 3.7. The ten-sample data set was collected with five points in each the positive and the negative half cycle with all data points taken within 40V of peak value to maintain optimal SNR and resolution. Figure 3.8 and Figure 3.9 show the scope captures for current clamp and shunt methods respectively for the 90° data point for visual procedure and to also validate the method's good agreement to the LTspice simulation. Another observation from the oscilloscope waveforms of experiment 1 is the residual charge left on C_{LOAD} reduces Δv. However, this should not dramatically impact the accuracy of the measurement if the residual charge is less than 40V. It is recommended to allow C_{LOAD} to discharge completely between iterations.

Table 3.1 Line Impedance Measurement Results of Experiment 1

Switch Angle (°)	Peak Voltage	Δv	i_{pk} (clamp)	i_{pk} (shunt)	R_{line} (clamp)	R_{line} (shunt)	% Difference
70	158.2	140.5	188.7	183.3	0.745	0.767	2.9%
70	158.4	141.6	188.9	183.9	0.750	0.770	2.7%
81	167.6	143.1	186.2	182.3	0.769	0.785	2.1%
90	169.8	134.6	187.6	184.1	0.717	0.731	1.9%
108	161.5	133.2	164.4	168.1	0.810	0.792	2.2%
231	-133.4	126.4	170.1	169.3	0.743	0.747	0.5%
270	-169.5	139.7	189.9	187.4	0.736	0.745	1.3%
289	-160.8	145.2	187.1	197.5	0.776	0.735	5.3%
300	-149.6	131.3	168.8	173.9	0.778	0.755	2.9%
306	-137.7	132.3	161.5	165.9	0.819	0.797	2.7%
				Mean	0.764	0.762	2.5%
				Standard Deviation	0.033	0.024	

Table 3.2 Operating Conditions and Metrology of the Measurement Waveform

OPERATION CONDITIONS		
PARAMETER	**VALUE**	**UNITS**
V_{AC}	120	V - RMS
Frequency	60	Hz
Service Panel	200	A - RMS
Circuit Breaker	20	A - RMS
Feed Wiring	12	AWG
METROLOGY		
EQUIPMENT	**DESCRIPTION**	**MEASURE**
PicoScope 3406D	200 MHz Oscilloscope	—
Hewlett Packard SI-9001	700V, 25 MHz Differential Probe	V_{LINE}
Flukei300s	300A, 20kHz AC/DC Current Clamp	I_{LINE}
Shunt Resistor	100W, 10mΩ 0.1%	—
Diodes Inc. GBJ2506	25A, 600V Rectifier	—
Panasonic EET-HC2D821BA	820μF, 200V, 20% Electrolytic Capacitor	—

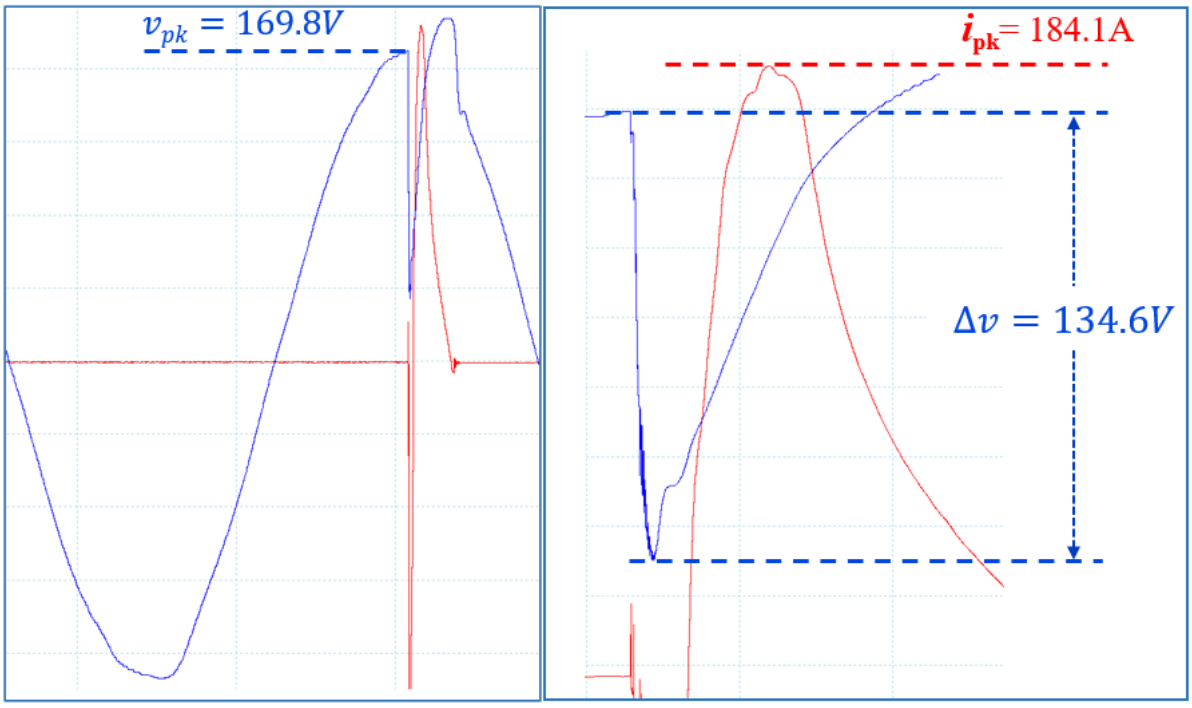

Figure 3.8 Experimental Voltage Sag and Current Peak at 90° Switching Angle Measured with Shunt: Blue= Voltage (V), Red= Current

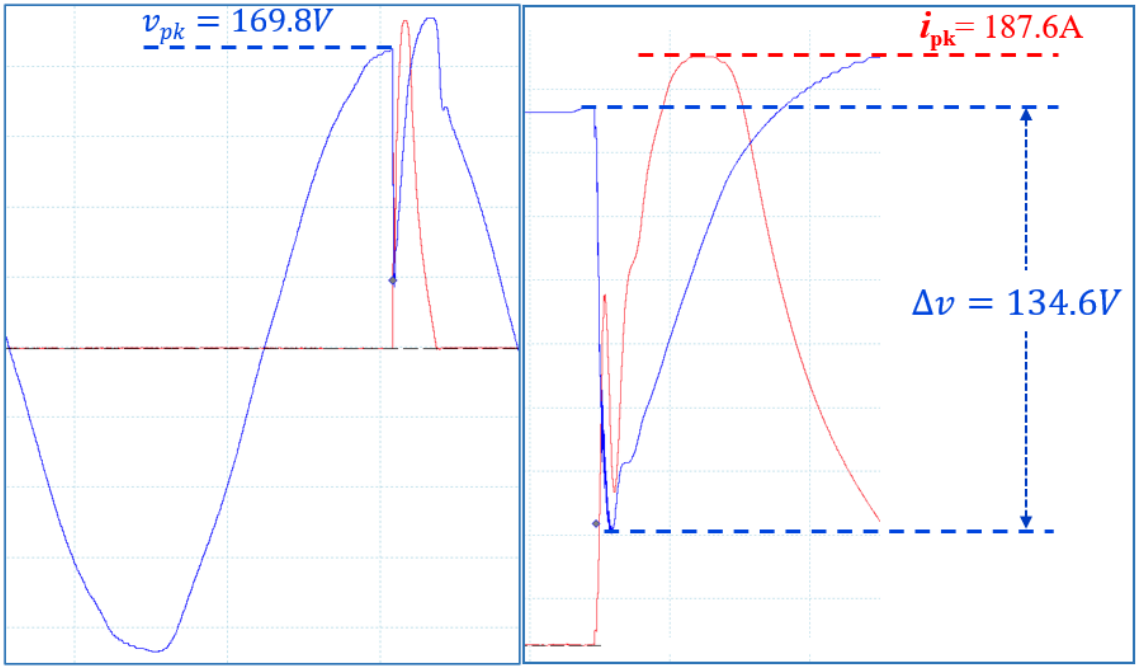

Figure 3.9 Experimental Voltage Sag and Current Peak at 90° Switching Angle Measured with Clamp: Blue= Voltage (V), Red= Current(A)

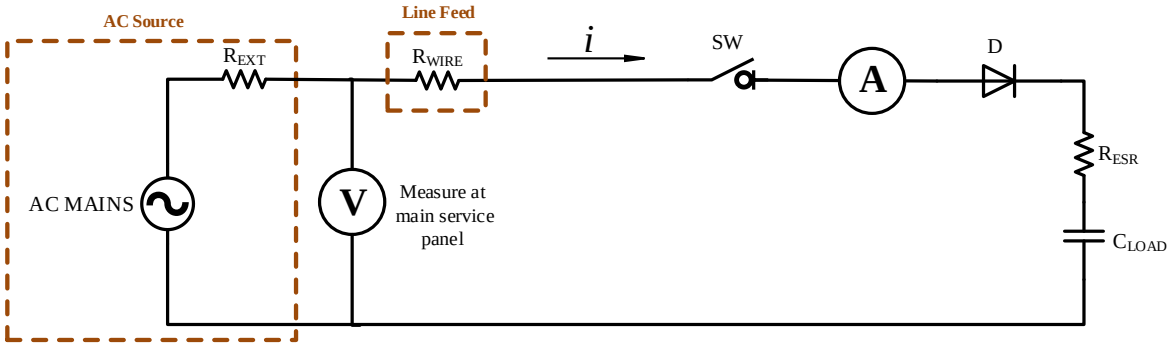

Figure 3.10 Line Impedance Distributed as External Source and Internal Wire Feed

One method to further validate the empirical data would be to compare the results of the first experiment to the calculated resistance of the line feed. However, calculating the total line impedance (R_S) of Figure 2 would be extremely challenging given information on external equipment of the residential electrical service entry would likely be unknown. If the line impedance is separated into two components, one being the external impedance (R_{EXT}) and the other being the connected line impedance (R_{WIRE}) as described in Figure 3.10, this approach can be used. First, experiment 1 would be repeated at the main electrical panel of the residence service entry yielding a measured value of R_{EXT}. Then R_{WIRE} can be calculated by knowing the wire type, gauge, and length. Finally, R_S, as described in Figure 3.2, can be calculated where $R_S = R_{EXT} + R_{WIRE}$.

The additional experimental devices under test (DUT) required to support this approach are described in Table 3.3 for reference. Table 3.4 shows the measurement results for experiment 2, yielding the average external impedance from the clamp and shunt measurements of R_{EXT} = 0.751Ω. The wire length from the first experiment was measured to be 14 feet. Given a resistance per unit length of 1.588mΩ/ft for 12AWG solid copper wire [10], R_{WIRE} can be easily determined:

$$R_{WIRE} = \left(14ft \cdot 1.588\frac{\text{m}\Omega}{ft}\right) * 2 = 0.044\Omega$$

And finally:

$$R_S = R_{EXT} + R_{WIRE} = 0.751\Omega + 0.044\Omega = 0.795\Omega$$

This result is in the range of measurements of Table 3.1 but lacks the desired certainty as the vast majority of the line impedance is distributed externally given the small resistance of the 14-foot wire feed. Extracting the measured value using the average of the clamp and shunt methods from experiment 1 and R_{EXT} from experiment 2 produces: $R_{WIRE\_MEAS\_14\Omega} = R_{S\_experiment1} - R_{EXT} = 0.763\Omega - 0.751\Omega = 0.012\ \Omega$. This is greater than 50% difference from the calculated value as 44mΩ is too small for the resolution of this process.

This validation can be improved if R_{WIRE} is increased dramatically. A third experiment was conducted on a known line feed length of 91 feet with a calculated resistance of $R_{WIRE\_CALC\_91\Omega} = 0.289\Omega$. The results of experiment 3 in Table 3.5 show an average total line impedance from the clamp and shunt measurements of 1.047Ω. Subtracting the measured source impedance R_{EXT} from the line impedance result of experiment 2 isolates the R_S value of the feed only. This provides a measured value of $R_{WIRE\_MEAS\_91\Omega} = 0.296\Omega$ which is within 2.5% of the calculated value. The excellent agreement of this result is in large part to the averaging of twenty measurements. As can be observed from the data in Tables 3.4 and 3.5, the range of the line impedance is 75mΩ and 79mΩ , respectively. This analysis performed with the minimum and maximum range points could reduce the agreement by a factor of ten or more.

Table 3.3 Experiment Description

#	Device Under Test	Length
1	Installed line feed	14 feet
2	Service entry main panel	0 feet
3	Uninstalled line feed	91 feet

Table 3.4 Line Impedance Measurement Results of Experiment 2

Switch Angle (°)	Peak Voltage	ΔV	i_{pk} (clamp)	i_{pk} (shunt)	R_{line} (clamp)	R_{line} (shunt)	% Difference
70	158.8	143.2	192.4	189.9	0.744	0.754	1.3%
75	163.2	142.8	192.1	188.5	0.743	0.758	1.9%
80	166.4	140.7	185.4	190.6	0.759	0.738	2.7%
90	168.6	146.7	187.7	184.2	0.782	0.796	1.9%
110	160	138.0	191.2	186.1	0.722	0.742	2.7%
225	-119.9	143.7	189.5	182.1	0.758	0.789	4.1%
270	-169.2	140.0	188.6	185.0	0.742	0.757	2.0%
285	-163.5	138.8	191.1	184.6	0.726	0.752	3.5%
300	-146.1	138.5	187.8	191.8	0.738	0.722	2.1%
310	-126.5	141.2	184.4	190.5	0.766	0.741	3.2%
				Mean	0.748	0.755	2.5%
				Standard Deviation	0.018	0.023	

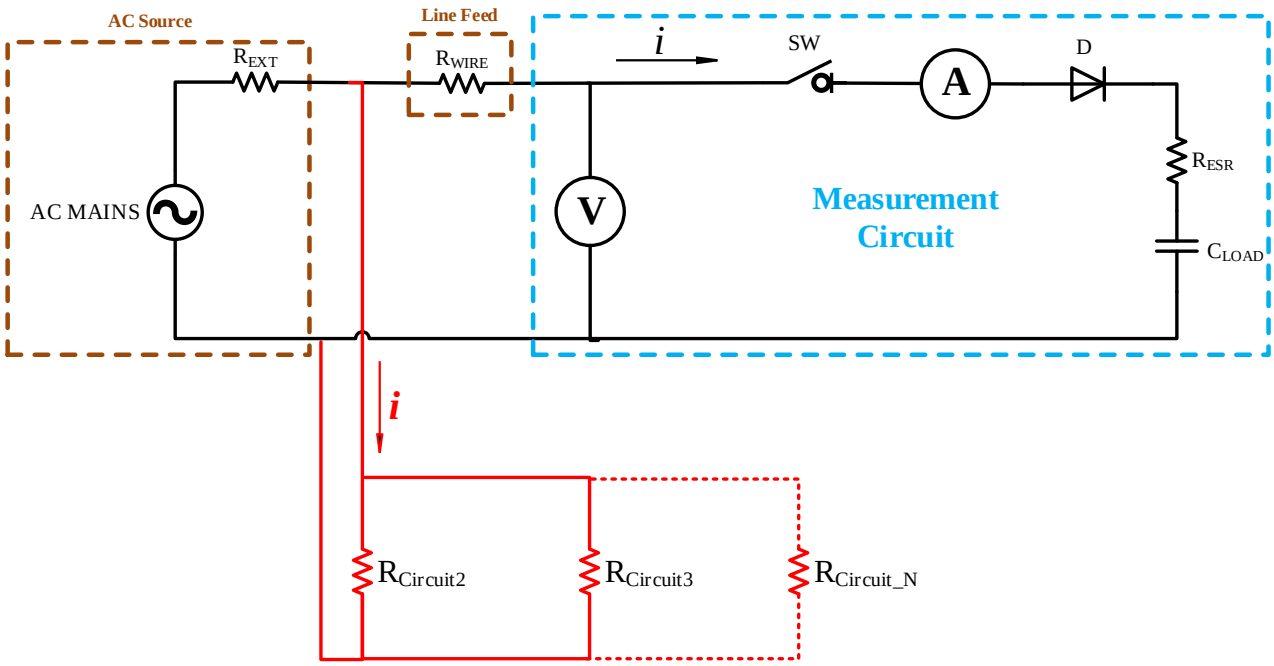

Figure 3.11 Measurement Circuit Impacted by Multiple Incremental Loaded Circuits Connected to the AC Mains

Further analysis of the results in Tables 3.1, 3.4, and 3.5, shows the undesirable large data range is due to several data points that could be classified as outliers. These irregular data points can largely be attributed to the presence of other loadings on the AC mains of the system under test. This loading branches from the measurement circuit as shown in Figure 3.11 and can be seen in the data as a change in v_{pk} as the increased or reduced current alters the $i \cdot R$ drop of the external line impedance. This consistent loading may have minimal impact on the measurement results but dynamic loads transitioning during the measurement sag event can have significant impact on the results. One identified method to abate these events would be to disconnect all potential loading circuits excluding the DUT which may not be feasible. Alternately, this impact could be minimized by averaging additional measurements while removing noticeable outliers.

Lastly, the effects of the line feed parasitic inductance terms L_S and L_P from Figure 3.1 that was omitted in the simplified model of Figure 3.2 can be seen in Figure 3.8 and Figure 3.9 as the current is shifted in time in the oscilloscope captures. The presence of reactive resonance. $L_S + L_P$ can be determined from these results but they have essentially no impact on the magnitude of the voltage sag and resistance calculation. However, it is recognized that the term "impedance" in academia is inclusive of reactive components versus its more casual use in industry. Therefore inductance calculation methods are included in this closing analysis.

Examining the current response in Figures 3.8, and 3.9, the current has the typical exponential response of an inductor transient which is an artifact of the series parasitic inductance of L_S and L_P. The series inductance can be calculated two ways: (1) knowing the time constant of an $R \cdot L$ circuit from equations 3.4 or (2) applying KVL to the line feed loop resulting in equation 3.5.

$$\tau = \frac{L}{R} \tag{3.4}$$

$$\Delta v = R \cdot i_{pk} + L\frac{di}{dt} \tag{3.5}$$

These two methods were evaluated using the LTspice simulation model which produced Figure 3.12. A series inductance of $L_T = L_S + L_p$ = 138μH, determined from online calculators for 91 feet of 12AWG Romex, was added to the simulation circuit.

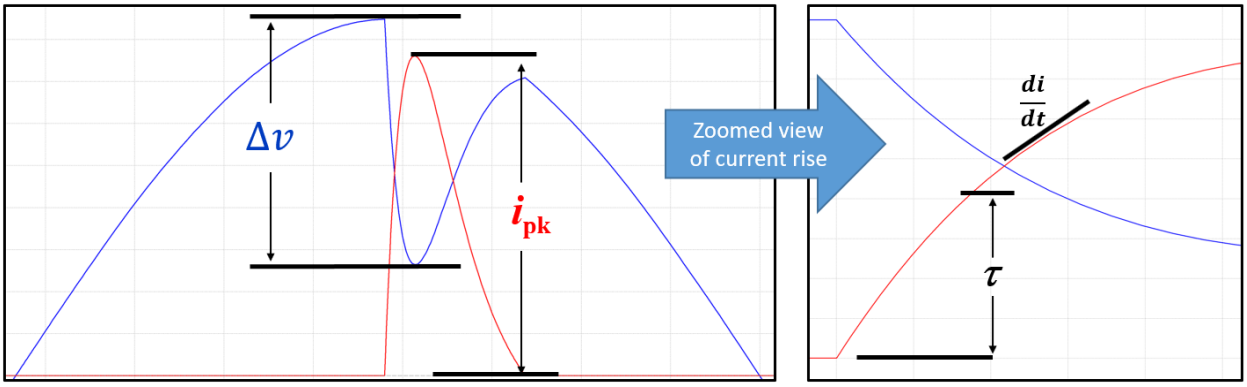

Figure 3.12 LTspice Simulation Waveforms with *Ls* = 138µH.

Method (2) was found to be unreliable as small variations in Δv or $\frac{di}{dt}$ measurements yield errors exceeding 100% in inductance calculations. Also, calculating $\frac{di}{dt}$ is extremely difficult without an oscilloscope with advanced math functions or exporting data into a program such as MATLAB making this option impractical. Method (1) produced consistent ballpark results yielding a value of L_T = 103µH. This is adequate to give the designer an idea of the reactance component of the line feed being analyzed.

The quantified resistance and inductance of the line feed can be used to determine the potential impact to the conducted EMI of a connected system. Qualitative application of the section 2.3 material can provide guidance of line impedance interaction with EMI filter characteristics while quantitative impact can be determined by applying CEM analysis methods of section 4.6.

CHAPTER IV

IMPROVED METHODOLOGY FOR CONDUCTED EMI ASSESSMENT

4.1 Proposed EMI Assessment Method

Chapter 4 material is published: Open Journal of Power Electronics, Oct. 2022 (ref. section 5.2)

Conventional test methods may introduce new challenges when evaluating WBG-based power electronic converter systems such as that presented in [21], [22]. As shown in Figure 4.1, connecting a ground-referenced EMI receiver to this type of converter system creates additional galvanic common-mode (CM) paths from the source filter (C_Y) [23] and power module parasitic capacitances (C_{ug}, C_{ag}, and C_{lg}) [24] through the EMI receiver's earth ground connection. These paths, displayed in Figure 4.1 as solid black lines for galvanic and brown dotted lines for parasitic, involve implicit capacitive couplings in the power source (C_Y), the simulated motor load (R_{load} and C_{sg}), the neutral connection point (C_{ng}), and the power module(s) (C_{ug}, C_{ag}, and C_{lg}) employed in the converter itself. The CM loop introduced by the galvanic instrumentation ground can dramatically impact the EMI behavior and compliance performance of this system, as reported in [21], [22]. One approach to address this problem is to utilize an alternate measurement method such as an oscilloscope with isolated voltage probes to obtain LISN measurements for compliance. However, adopting this approach introduces two potential challenges. The first challenge is ensuring that the alternate instrumentation has comparable accuracy to the traditional instrumentation. The second challenge is implementing the particular frequency-domain metrics

used for EMI compliance assessment. Compliance is typically evaluated in the frequency domain using metrics such as peak, quasi-peak (QP), and average operators that are applied to the

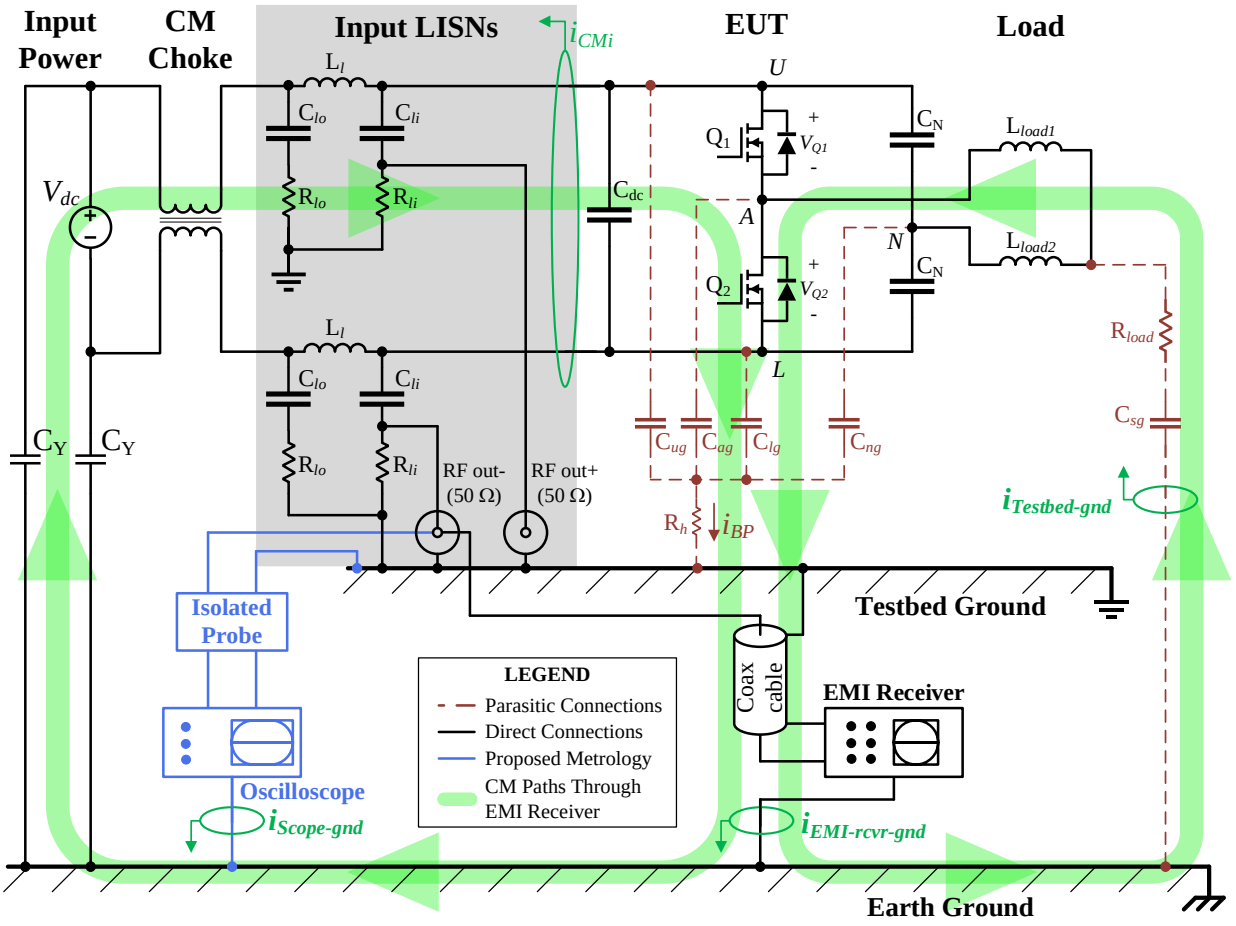

Figure 4.1 EMI Converter Testbed of [1], [2] with Induction Motor Load [5] with CM Loops

measured spectra. These metrics are not available in a conventional oscilloscope, which operates in the time domain. Therefore, software methods must be employed to post process the measured time-domain data to complete this compliance analysis. If these challenges can be overcome, the measurement approach described herein will have comparable accuracy of compliance assessments for WBG-based power electronic systems.

EMI compliance is evaluated against quasi-peak (QP) and average limits per 47 CFR part 15 [27]. A significant challenge associated with these compliance measurements is achieving full-band QP and average data given the time constants and dwell time requirements of [27], which are adopted from and defined in the CISPR 16-1-1 standard [26]. Many researchers have identified QP as the critical quantity for evaluating EMI compliance [28], [30], [31]; while [32] stresses that the QP measurement is of greatest importance. This work affirms that QP data is of greatest significance since it is responsible for most conducted EMI compliance failures. In the authors' experience, a device under test (DUT) will often comply with average limits but violate QP limits or pass QP limits with insufficient margin.

A typical EMI receiver requires that the user select points of interest from the peak output and then QP and average values are produced only for these selected frequency ranges. Muller makes this recommendation as one of the QP time saving principles outlined in [33]. This method is recommended because computing full-band QP data over the entire compliance band often requires several hours or more [29]. However, this timesaving approach, which relies on the operator selecting ranges of interest, could lead to false compliance passes because exceedances may exist in omitted sections of the scan. On the other hand, a designer may incur unnecessary cost to improve a peak exceedance that may be compliant when properly measured and evaluated as QP.

Considering these recognized challenges, significant efforts have been undertaken to provide full-band QP and average spectra with fast execution time. For example, some instrument vendors have developed hardware that is specifically designed to perform fast QP computations. One such instrument, the Gauss Instruments TDEMI X [34], is marketed as being 64,000 times faster than conventional EMI receivers. However, instruments with high-speed analysis capabilities are prohibitively expensive. Another approach is the development of "offline"

computational tools that can compute QP spectra from recorded experimental data or simulation predictions. For example, L. Yang and S. Wang [35] and Karaca et al. [38] offer predictive EMI performance analysis tools with fast computation times. These methods work in the frequency domain and rely on approximations for calculations of the compliance variables. Krug and Prusser [16] offer a similar frequency-based method. Their approach dramatically reduces peak scan times and offers some improvements for the computation of QP spectra as well. Giezendanner et al. [42] introduce a method of computing QP spectra in the time-domain and discuss the computational challenges associated with this approach.

This work presents an alternative approach for achieving full-band QP and average spectra. The proposed algorithm is implemented in MATLAB and is referred to as the MATLAB EMI receiver emulator (MERE). MERE works exclusively in the time domain, which stands in contrast to the frequency-domain methods utilized by most of the existing state-of-the-art implementations [30], [35], [36], [37]. This eliminates the need for approximations to deliver the compliance metrics, which provides improved accuracy. Through the application of initial conditions during each computation step, MERE delivers the full complement of compliance spectra (peak, QP, and average) approximately 75% faster than a typical instrument excluding lab and instrument setup time.

The contributions of this work are as follows. First, it proposes an isolated method for measuring the conducted emissions of power electronic systems. This method minimizes circulating currents through the instrumentation. Second, it demonstrates that the alternate measurement setup necessary to implement this approach can exceed the accuracy of conventional EMI receivers when attenuation is required. Third, it offers a data post processing tool that can efficiently produce full-band emissions metrics that are comparable to those produced by

commercial EMI receivers. Last, empirical data is presented showing the significant impact EMI receiver ground paths present to compliance measurement accuracy.

The organization of this work is as follows. Section 4.2 analyzes the accuracy of a conventional EMI receiver compared to the proposed alternate measurement setup, referred to as the "isolated" approach. Section 4.3 discusses the requirements and operation of EMI receivers. Section 4.4 describes the design and operation of the MATLAB EMI receiver emulator (MERE) post processing tool. Section 4.5 compares the performance of MERE to commercial EMI receivers across multiple test cases and analyzes the impact of circulating ground currents in the conventional setup.

4.2 Accuracy Analysis of Alternate EMI Measurement System

The first step in verifying the proposed isolated approach involves evaluating the accuracy of the isolated instrumentation setup compared to the conventional EMI receiver setup. Table 4.1 presents a calculated amplitude accuracy comparison of three candidate measurement setups computed from parameters provided in their respective datasheets: (1) the Gauss Instruments TDEMI X EMI receiver [14], (2) the Keysight N9038 EMI receiver [23], and the proposed isolated setup. Frequency accuracy of an oscilloscope is difficult to determine for this type of application. Therefore, this comparison focuses on the amplitude accuracy of the instruments as this comparison is possible to perform analytically. It is noted that an empirical validation of the isolated metrology accuracy (which reflects both the amplitude and frequency components) is included in Section V. The isolated measurement setup consists of a Tektronix 5-series MSO oscilloscope [25] and a Tektronix THDP0200 isolated voltage probe [26]. For the conventional EMI receiver, measurement accuracy and optional attenuator accuracy values are considered in

the summary. For the isolated setup, oscilloscope resolution, oscilloscope gain, probe gain, and probe bandwidth accuracies are included in the accuracy summary.

Table 4.1 Amplitude Accuracy Comparison: Conventional Setup and Isolated Setup

	EMI Receiver Measurement Accuracy (%)*	Attenuator (20 dB) Accuracy (%)*	Overall RSS Accuracy (%)
Gauss TDEMI X	2.878	Not included	2.878
Keysight N9038	1.712	Not included	1.712
Gauss TDEMI X	2.878	2.276	3.669
Keysight N9038	1.712	2.276	2.848

Oscilloscope Resolution bits (ENOB)*	Oscilloscope Resolution Accuracy (%)	Oscilloscope Gain Accuracy (%)*	Probe Gain Accuracy (%)*	Probe BW Accuracy (%)*	Overall RSS Accuracy (%)
7.9	0.209	0.5	2	1.1	2.346
10	0.049	0.5	2	1.1	2.337
12	0.012	0.5	2	1.1	2.337

* Values form manufacturer datasheets [14] [23] [25] [26]

The root-sum-of-squares (RSS) technique [24] was employed to combine the accuracy components of each system to yield overall system accuracy. For the conventional setup, the overall accuracy is computed as follows:

$$a_{conv} = \sqrt{(a_M)^2 + (a_A)^2} \tag{4.1}$$

where a_M and a_A are the EMI receiver measurement and attenuator accuracies, respectively. For the isolated setup, the overall accuracy is computed as follows:

$$a_{alt} = \sqrt{(a_R)^2 + (a_G)^2 + (a_{PG})^2 + (a_{PB})^2} \tag{4.2}$$

where a_R, a_G, a_{PG}, and a_{PB} are the oscilloscope resolution, gain, probe gain, and probe bandwidth accuracies, respectively.

For the conventional setup, typical or 95th percentile accuracies were used in place of worst-case values. For the isolated setup, accuracy is presented for three resolution settings of the oscilloscope in terms of effective number of bits (ENOB). The first setting corresponds the ENOB value for an inexpensive oscilloscope, while the other two settings correspond to the ENOB values for high-end instruments. Surprisingly, oscilloscope resolution is not a major contributor to the overall system accuracy, which is dominated by the contribution of the 1.5 kV isolated differential voltage probe used in this setup. It is noted that the relative importance of the individual contributions will be influenced by probe selection and therefore by the voltage level of the system under test. This analysis demonstrates that the isolated setup is expected to have similar error to the conventional setup, according to instrument specifications. However, the accuracy of the conventional setup will also be influenced by the presence of inline attenuation. The use of external attenuators is usually required to protect the instrument input when measuring power electronic systems with an EMI receiver. Table 4.1 presents an additional configuration for each EMI receiver that reflects the influence of adding a HAT-20+ coaxial 20 dB attenuator [27] to the signal chain. These configurations demonstrate that an additional accuracy degradation of approximately 2% is incurred by the use of external attenuation. This can be a significant consideration depending on the amount of attenuation required given that CISPR 16-1-1 [26] specifies an accuracy of better than +/- 2 dB in the band B frequency range.

4.3 EMI receiver Requirements and Operation

This section describes the operation of a typical EMI receiver.

4.3.1 Application Standard and Frequency Band

The scope of this work focuses on the conducted emissions requirements for class A and B unintentional radiators per 47 CFR part 15 [27], which are subject to conducted compliance in band B (150 kHz – 30 MHz). This category covers a vast population of devices that face significant EMI challenges, many of which are caused by power switching circuits.

4.3.2 Measurement System and Compliance Limits

Compliance to 47 CFR part 15 conducted emissions requirements is determined by measurements acquired from an EMI receiver connected at the measurement ports of 50 μH/50 Ω line impedance stabilization networks (LISNs) [27]. The LISNs are connected in the power path of the DUT allowing conducted emissions to be evaluated per the requirements set forth in [27]. Specifically, the measurements are performed in the frequency range defined by CISPR 16-1-1 [26] and compared to the limits described in Table 4.2. It is noted that the compliance limits are imposed as QP and average quantities rather than peak quantities. The QP measurement is not straightforward as it is intended to "weigh" the repetitiveness of reoccurring peaks. This weighing operation can be modeled by the capacitor voltage in the analog circuit shown in Figure 4.2.

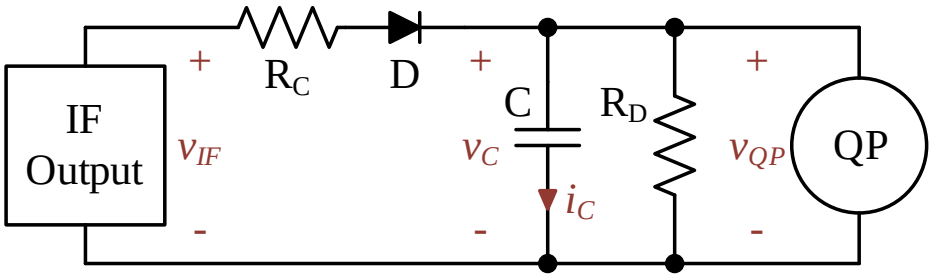

Figure 4.2 Quasi-peak Detection Circuit [40]

Table 4.2 Conducted Limits and Quasi-peak Time Constants [27]

Emission Frequency (MHz)	Conducted Limits (dBmV)			
	Class A		Class B	
	QP	Ave	QP	Ave
0.15 - 0.5 ….....	79	66	66 to 56	56 to 46
0.5 - 5 ….....	73	60	56	46
5 - 30 ….....	73	60	60	50

	IF 6dB BW	τ_c	τ_d	τ_m
Band B (0.15 - 30MHz)	9kHz	1 ms	160 ms	160 ms

The charge time, or "attack time" is determined by $R_C \cdot C$; while the discharge time, or "decay time" is determined by $R_D \cdot C$. Since the attack time is much shorter than the decay time, the capacitor voltage is correlated to the frequency of pulse repetition. It should be noted that modern EMI receivers implement this weighting function in software rather than with analog circuitry.

4.3.3 EMI Receiver Operation

The EMI receiver general operation shown in Figure 4.3 can be described by the following sequence. First, the RF signal measured at the LISN is preconditioned via an attenuator, preselection filter, and preamplifier. The signal is then mixed with the sweep generator, which is the prescribed method of stepping through the selected band.

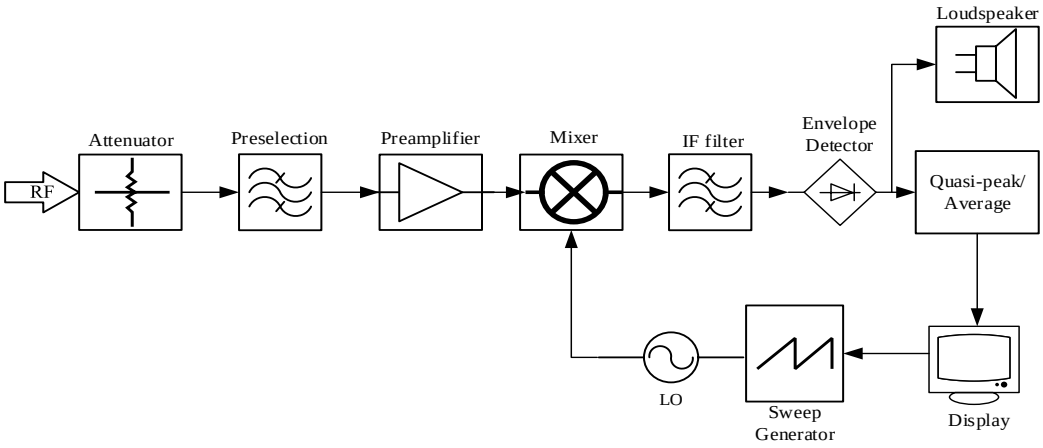

Figure 4.3 Example Block Diagram of EMI Receiver [26]

At each step, the signal is processed by the intermediate filter (IF) at the specified resolution bandwidth (RBW), which is 9 kHz for band B. Next, the signal is demodulated with an envelope detector. Finally, the QP and average values are computed, and the process is repeated at each frequency step until the end of the measurement band is reached. EMI receivers may allow for configurable step size, which should be less than the IF 6 dB RBW (Table 4.2). Typically, the step size is set to ½ the RBW value [29],[38]. In general, the compliance measurement block that computes the quasi-peak and average spectra is the most computationally intensive step of the system [32],[33].

It is noted that the standard includes tolerance and variation criteria for certain portions of the procedure shown in Figure 4.3, such as the shape of the IF filter roll-off [26]. To understand the impact of these parameters on compliance measurements and establish an acceptable variance threshold, three CISPR 16-1-1 compliant, commercial EMI receivers were compared experimentally: the Gauss Instruments TDEMI X, the Rohde & Schwarz FSH20, and the Keysight N9038A. Each instrument was configured with identical parameters and connected to an arbitrary

waveform generator configured to produce a 400 kHz square wave. This signal was chosen as a reference due to its rich harmonic content, which provides a multitude of peak comparison points. An overlay of the peak, QP, and average spectra produced by these instruments are included in Figure 4.5. The results demonstrate observable differences, particularly with wide separation in the noise floors. On the other hand, the fundamental and harmonic peaks agree within approximately 2.5 dB across the entire measurement band. Discussions with instrument manufacturers revealed a significant level of proprietary content in the implementation of the standard procedure shown in Figure 4.3, which may account for the observed differences. It is noted that this comparison was performed multiple times, with similar results observed in every case. This demonstrates that CISPR 16-1-1 compliant instruments may differ in the peak, QP, and average spectra computed for a given signal by as much as 2.5 dB. It is further noted that MIL-STD-461G [39] specifies a 3 dB variance acceptance criterion for LISN attenuation over frequency. This specification is not related to the accuracy of the measurement receiver used in MIL-STD-461G. However, this specification nevertheless reinforces that 2.5 dB may be an acceptable variance for compliance measurements performed with different instruments.

4.4 MATLAB EMI Receiver Emulator (MERE)

The MATLAB EMI receiver emulator (MERE) is a custom software package written in MATLAB that calculates EMI performance metrics comparable to those produced by a CISPR 16-1-1 compliant EMI receiver. This tool or a similar method is necessary to utilize the isolated measurement setup proposed in this paper for EMI compliance evaluation. MERE performs all operations in the time domain, after reading input from a data file. The content of this file may represent waveforms produced by a circuit simulator or measured signals from an oscilloscope or data logger. In either case, the data should represent LISN voltages that are measured in the same

manner described previously. The input file contains the instantaneous time and LISN voltage magnitude for a recommended minimum duration of 70 switching cycles to ensure capture of system anomalies. The sample rate for the LISN voltage measurements should be at least eight times greater than the highest frequency of interest (30 MHz for band B).

The operation of the MERE process is shown in functional block form in Figure 4.4. To start the process, data is imported into the MATLAB environment as a numerical table. The frequency sweep loop is initialized to the start of the frequency band. This loop sweeps the center frequency f_c across the measurement band at the prescribed increment of ½ the required IF filter RBW, which is specified in Table 4.2. During each iteration in the calculation loop, the time-domain data is resampled at the sampling frequency (f_s) which is critical for optimizing the resulting vector length to achieve a balance between computational efficiency and accuracy. By executing a large number of experiments, it was determined that the best results are obtained in the range $4f_c \leq f_s \leq 8f_c$. After the input data is resampled, it is processed through the IF filter. A Gaussian filter was implemented using the MATLAB signal processing toolbox. Note that other filter types were trialed and produce comparable peak results. This filtered data is then processed through the MATLAB envelope function.

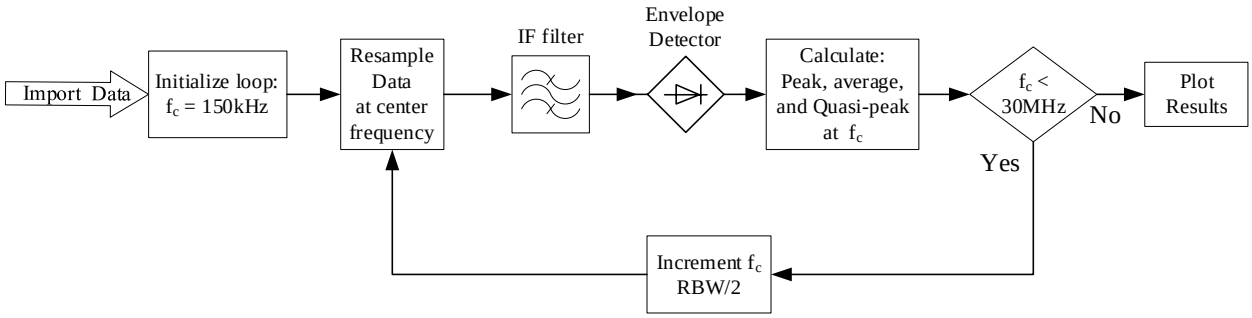

Figure 4.4 MERE Functional Block Diagram for CISPR Band B

The peak and average values are determined by applying the MATLAB max and average functions to the output vector of the envelope function. However, quasi-peak is significantly more challenging as it requires numerically solving two differential equations based on the two operating points of the quasi-peak detection circuit of Figure 4.2. These two operating points correspond to the two diode conduction modes.

When the diode is conducting ($i_C > 0$), the current through the capacitor is:

$$i_C = \frac{v_{IF} - v_C}{R_C} - \frac{v_C}{R_D} = C\frac{dv_C}{dt} \tag{4.3}$$

where v_{IF} is the output voltage of the IF filter, v_C is the capacitor voltage, R_C is the charge resistor, and R_D is the discharge resistor. Rearranging (15) and recognizing from Figure 4.2 that $v_{QP} = v_C$ yields

$$v_{QP} = \int \left(\frac{v_{IF} - v_{QP}}{R_C \cdot C} - \frac{v_{QP}}{R_D \cdot C}\right) dt \tag{4.4}$$

where $\boldsymbol{v_{QP}}$ is the quasi-peak output voltage. Converting to the Forward Euler form yields the first equation for numerical analysis:

$$v_{QP}(n+1) \approx \mathrm{h} \cdot \left(\frac{v_{IF}(n) - v_{QP}(n)}{R_C \cdot C} - \frac{v_{QP}(n)}{R_D \cdot C} \right) + v_{QP}(n) \tag{4.5}$$

where *h* is the integration time step. When the diode is not conducting **($i_C < 0$),** the current through the capacitor is:

$$i_C = \frac{-v_C}{R_D} = C \frac{dv_C}{dt} \tag{4.6}$$

where R_D is the discharge resistor. Rearranging (18) and again recognizing from Figure 4.2 that $v_{QP} = v_C$ yields

$$v_{QP} = \int \left(\frac{-v_{QP}}{R_D \cdot C} \right) dt \tag{4.7}$$

Converting to the Forward Euler format yields the second equation for numerical analysis:

$$v_{QP}(n+1) \approx \mathrm{h} \cdot \left(\frac{-v_{QP}(n)}{R_D \cdot C} \right) + v_{QP}(n). \tag{4.8}$$

These two states are summarized by

$$v_{QP}(n+1) \approx \begin{cases} \mathrm{h} \cdot \left(\frac{v_{IF}(n) - v_{QP}(n)}{R_C \cdot C} - \frac{v_{QP}(n)}{R_D \cdot C} \right) + v_{QP}(n) & i_C > 0 \\ \mathrm{h} \cdot \left(\frac{-v_{QP}(n)}{R_D \cdot C} \right) + v_{QP}(n) & i_C < 0. \end{cases} \tag{4.9}$$

The forward Euler equations (4.9) were implemented in a nested loop in the calculation block

of Figure 4.4 to numerically solve for the QP voltage. Finally, f_c is incremented by ½ the RBW value, and the process is repeated until the end of the measurement band is reached. It is noted that all operations are performed in the time domain, including the application of the IF filter. The computational burden can be significantly reduced by the careful application of initial conditions. Initial conditions can be inferred from the known relationship between the four following magnitude metrics [40]:

$$Peak \geq QP \geq RMS \geq Average \tag{4.10}$$

Thus, the initial value for the QP numerical integration can be set to the RMS value of the envelope detector, which greatly reduces the number of iterations required to reach the final value at each (f_c) frequency step.

Given the operational implementation of the commercial instruments is proprietary, the MERE tuning process is completed through iterative experimental comparisons. The primary sensitivity of the tuning process is the selection of the IF filter type, filter parameters, and sampling frequency (f_s). For the Gauss instrument, a Gaussian filter was selected based on the instrument results and the parameters were adjusted to achieve the strongest agreement with the instrument's noise floor (see Appendix A.2). Note the peak values vary little during this adjustment. The frequency step should also be tweaked to match the instrument settings.

It is noted that the results shown in the data tables of Figure 4.5 do not strictly obey equation 4.10 due to the selection of the reference signal. It is well known that continuous, unmodulated signals, such as the square-wave reference signal used in this example, produce equal values for

all detectors [40]. Thus, any variance observed between the peak, QP, and average values reported in Figure 4.5 is likely the result of measurement noise.

4.5 Method Verification

4.5.1 Function Generator Verification

For verification, the output of MERE was also compared to peak, QP, and average measurements with the three commercial EMI receivers shown in Figure 4.5. As observed in this figure, MERE produces good agreement with the EMI receiver measurements for all peaks. MERE predictions average within 2 dB of all EMI receiver measurements over the entire band for peak, QP, and average results. Specifically compared to the Gauss TDEMIX instrument, MERE is within 2 dB of each peak with the exception of 20.4 MHz data point. Several MERE parameters including filter type, filter order, sampling frequency, and signal vector length were specifically tuned to achieve the agreement to the Gauss TDEMI X measurement. This procedure is straightforward, and MERE can be readily tuned to match the performance of other instruments. This tunability highlights one of the ancillary benefits of MERE over single-instrument analysis, as it provides a measure of insight into the sensitivity of parameters that are employed while implementing the analysis procedure shown in Figure 4.4. It is also noted that the results in Figure 4.5 were produced by MERE in 44 minutes running on a standard 2.7 GHz laptop. By comparison, a conventional EMI receiver required almost four hours to complete analysis of the same reference signal. required almost four hours to complete analysis of the same reference signal.

MERE was also compared to the frequency domain tool of [35]. These results are presented in Appendix A.

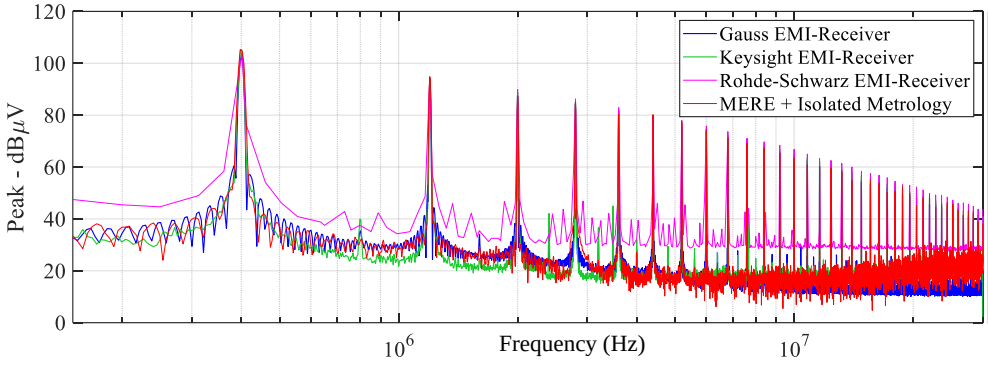

Freq	Gauss	Keys.	R+S	MERE
400kHz	103.2	105.7	104.22	104.8
1.2MHz	92.98	93.96	94.72	93.67
2MHz	87.51	88.82	89.98	87.38
2.8MHz	84.36	85.01	86.27	85.09
3.6MHz	81.41	81.86	82.89	80.3
4.4MHz	78.31	79.16	79.85	78.44
10MHz	64.07	65.09	66.83	63.37
20.4MHz	48.24	49.54	52.29	44.6
29.2MHz	39.28	41.36	43.75	38.35

(a)

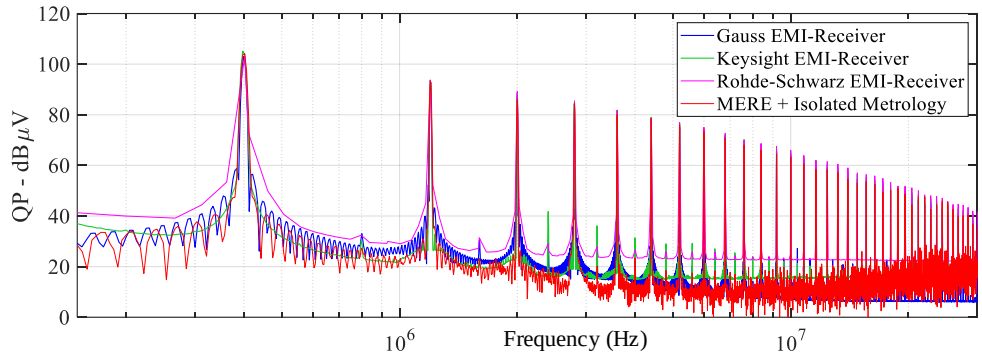

Freq	Gauss	Keys.	R+S	MERE
400kHz	103.1	105.1	103.1	104.16
1.2MHz	92.88	90.96	93.69	92.16
2MHz	87.4	88.61	89.19	85.94
2.8MHz	84.25	84.88	85.47	84.58
3.6MHz	81.3	80.92	81.84	80.07
4.4MHz	78.2	79.03	78.64	78.16
10MHz	63.92	64.88	65.93	63.04
20.4MHz	47.81	49.16	51.12	43.8
29.2MHz	38.33	40.81	41.91	36.93

(b)

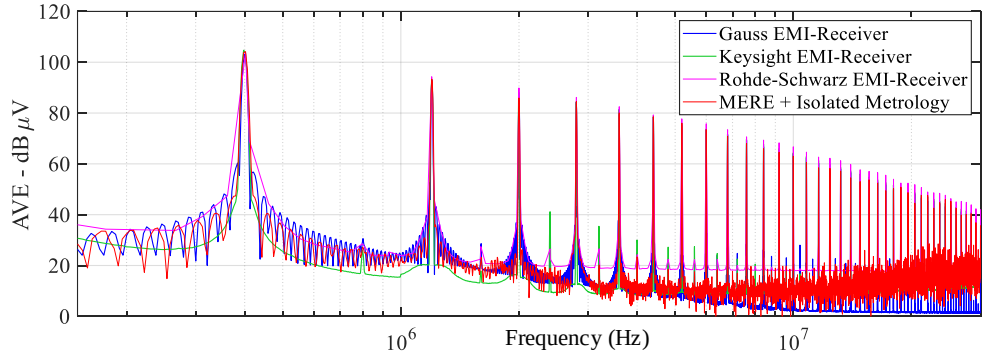

Freq	Gauss	Keys.	R+S	MERE
400kHz	103.2	104.2	103.66	104.17
1.2MHz	92.98	91.9	94.3	92.16
2MHz	87.5	88.2	89.88	85.95
2.8MHz	84.35	83.9	86.18	84.58
3.6MHz	81.4	80.8	82.49	80.07
4.4MHz	78.3	77.4	79.26	78.16
10MHz	64.05	64.35	66.71	63.04
20.4MHz	48.04	48.66	51.83	43.7
29.2MHz	38.76	40.11	42.34	36.89

(c)

Figure 4.5 EMI Performance Comparison Plots for a 400 kHz Square Wave Stimulus: (a) Peak, (b) QP, and (c) Average

4.5.2 WBG-Based Converter Validation

The efficacy of the proposed isolated measurement approach was further evaluated through an experimental study involving a WBG-based single-phase inverter. This inverter utilizes a single commercially available 1.2 kV SiC MOSFET half-bridge power module from Wolfspeed (CAS120M12BM2). For all experiments reported here, the inverter was operated at 177 kHz using complementary PWM with a fixed 50% duty cycle. The load of this converter is designed to simulate the impedance of one phase of a three-phase motor, with a reasonable parasitic coupling to the chassis of the machine, which is assumed to be bonded to earth ground for safety reasons. In this study, the notional schematic shown in Figure 4.1 was realized in hardware by making minor adjustments to the EMI testbed previously presented in [2]. The hardware realization of this system is shown in Figure 4.6 and Figure 4.7. Two experiments were performed using this configuration as described in Table 4.3 and the operating conditions and metrology components are summarized in Table 4.4.

Table 4.3 Experiment Descriptions

#	Metrology	Description
1	EMI Receiver & Oscilloscope	Simultaneous Time & Frequency Domain
2	Oscilloscope	Time Domain Only

Table 4.4 Operating Conditions and Metrology of Study

OPERATING CONDITIONS		
PARAMETER	**VALUE**	**UNITS**
V_{dc}	600	V
f_{sw}	177	kHz
$t_{dead\text{-}time}$	700	ns
R_{load}	416.7	Ω
C_{sg}	0.2	µF
METROLOGY		
EQUIPMENT	**DESCRIPTION**	**MEASURE**
Tektronix MSO58	1 GHz, 6.25 GS/s Oscilloscope	—
Tektronix THDP0200	1.5 kV, 200 MHz Differential Probe (150V Mode)	V_{LISN}
Tektronix TCP0030A	30 A, 120 MHz Current Probe	$I_{Testbed\text{-}gnd}$ $I_{EMI\text{-}rcvr\text{-}gnd}$ $I_{Scope\text{-}gnd}$
Keysight N9000A	9 kHz – 3 GHz Signal Analyzer	V_{LISN}
Mini-Circuits BW-20N100W	20 dB Attenuator	—
Mini-Circuits HAT-20+	20 dB Attenuator	—
Schwarzbeck VTSD 9561 D	20 dB Pulse Limiter	—

In the first experiment, the testbed was operated with a conventional EMI receiver (Keysight N9000A) connected to the DC- LISN measurement port. The EMI receiver was attached using attenuators to achieve 60 dB of total attenuation. This was necessary to reduce the unfiltered

LISN voltage from an unattenuated value of 30.9 dBm to a level that would not damage the EMI receiver input. The EMI receiver was powered through a Tripp-Lite IS1000 isolation transformer to minimize CM currents through the instrument's power leads. A second, standalone 50 Ω terminating resistor was connected to the DC+ LISN measurement port, which was not instrumented. This configuration is representative of the conventional EMI compliance setup. Simultaneously during this experiment, an isolated voltage probe was used to measure the DC- LISN in the time domain. These specific measurements are shown in Figure 4.7a and b. The data recorded from this probe was later analyzed using the MERE method. This experiment serves two purposes. First, it provides further opportunity to validate the output of the MERE method against EMI receiver measurements. This analysis is more representative of a power electronic converter compliance setup compared to the validation studies presented in the previous section. Second, this study provides a mechanism to directly evaluate the impact of the spectrum analyzer on the resulting emissions measurements.

In the second experiment, the spectrum analyzer was removed and the DC- LISN measurement port was connected to a standalone 50 Ω terminating resistor. In this configuration, the isolated voltage probe remained attached to the DC- LISN measurement port to measure the LISN voltage in the time domain. This metrology is demonstrated in Figure 4.7c, and the details of these two experiments are summarized in Table 4.3. The time-domain LISN voltage measurements from both experiments were analyzed using the MERE method for subsequent comparison and analysis.

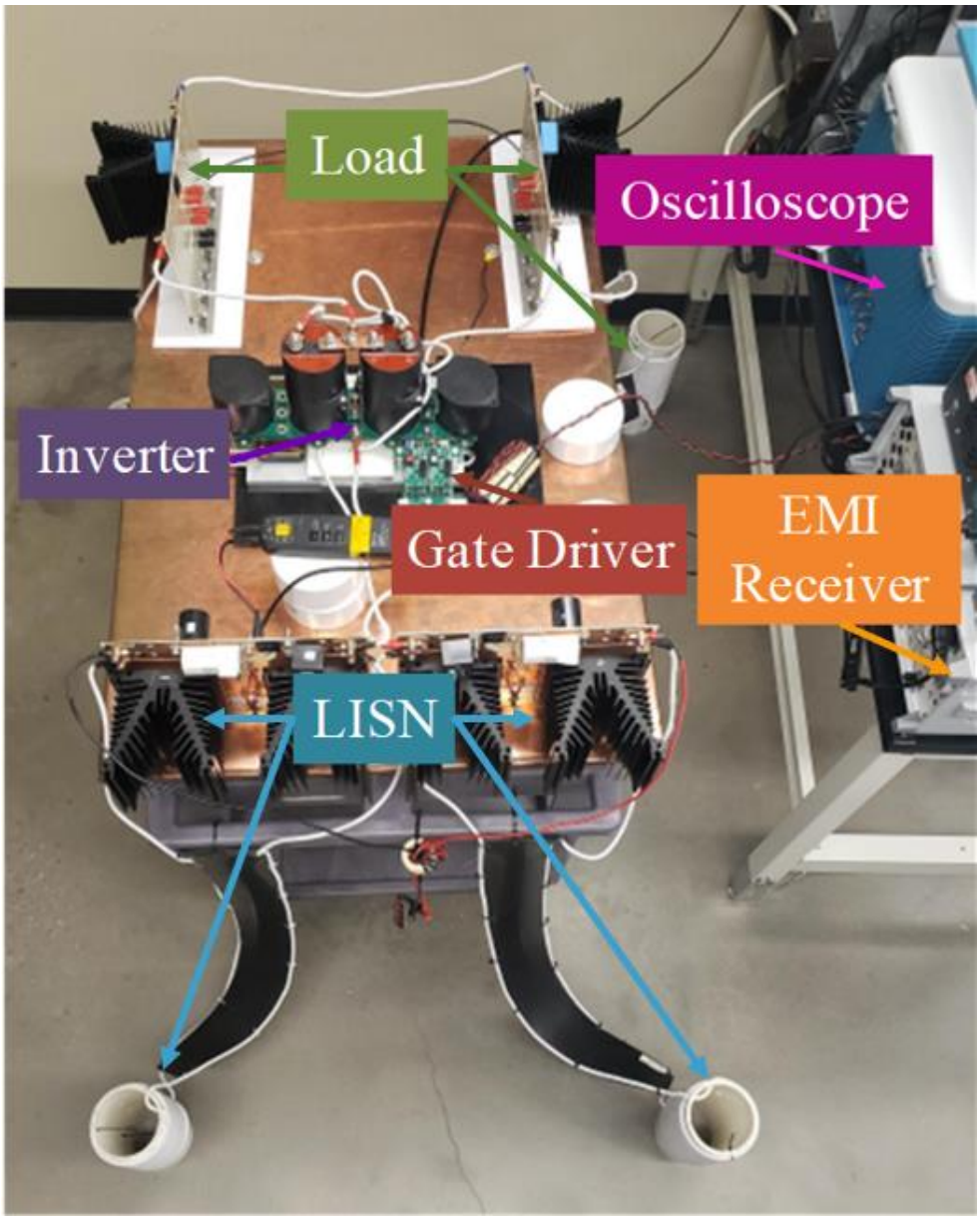

Figure 4.6 High-Power Converter EMI Testbed

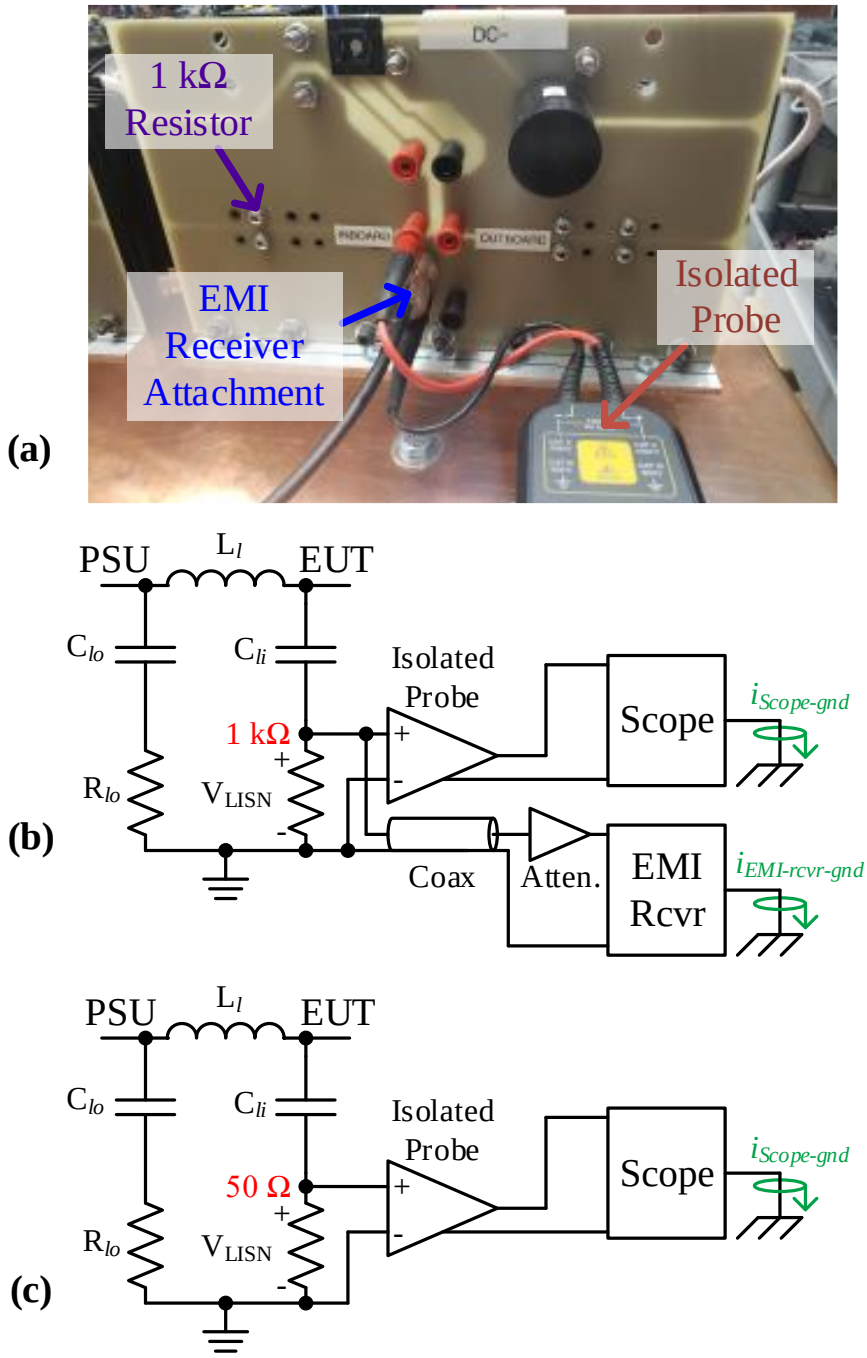

Figure 4.7 a) LISN Metrology Attachments on the Realized Testbed, and Notional Diagram of the Metrology Connections for (b) Experiment 1 and (c) Experiment 2

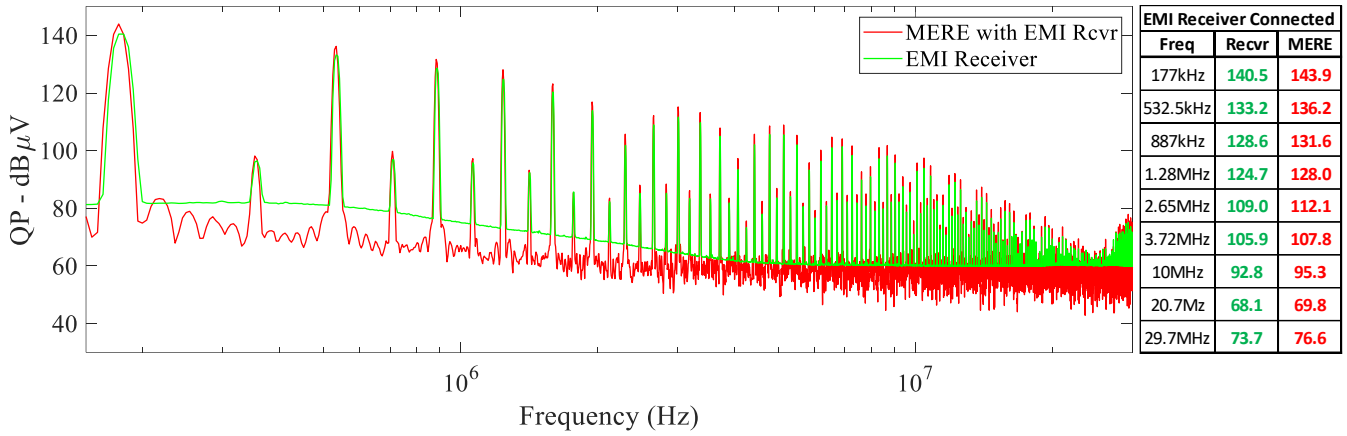

EMI Receiver Connected		
Freq	Recvr	MERE
177kHz	140.5	143.9
532.5kHz	133.2	136.2
887kHz	128.6	131.6
1.28MHz	124.7	128.0
2.65MHz	109.0	112.1
3.72MHz	105.9	107.8
10MHz	92.8	95.3
20.7Mz	68.1	69.8
29.7MHz	73.7	76.6

(a)

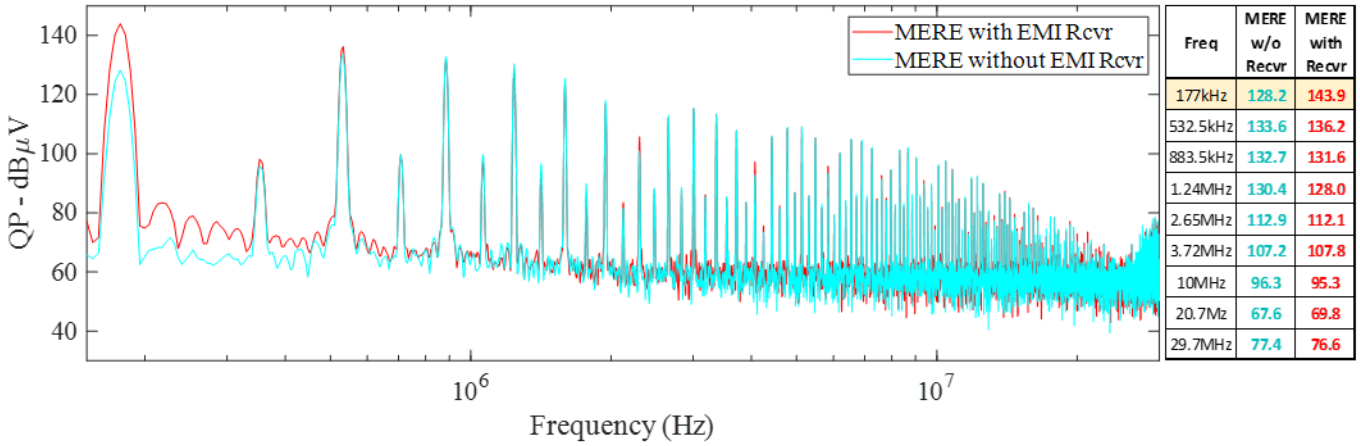

Freq	MERE w/o Recvr	MERE with Recvr
177kHz	128.2	143.9
532.5kHz	133.6	136.2
883.5kHz	132.7	131.6
1.24MHz	130.4	128.0
2.65MHz	112.9	112.1
3.72MHz	107.2	107.8
10MHz	96.3	95.3
20.7Mz	67.6	69.8
29.7MHz	77.4	76.6

(b)

Figure 4.8 (a) Experiment 1: Quasi-peak Spectra: EMI Receiver Measurement vs. MERE Output with EMI Receiver Connected
(b) Experiment 2: Quasi-peak Spectra: MERE Output with EMI Receiver Connected (Experiment 1) vs MERE Output without EMI Receiver Connected

The results of Experiment 1 are presented in Figure 4.8a for the two measurement methods. In this experiment, the MERE method output and the EMI receiver measurements demonstrate strong agreement across the entire CISPR frequency range. Specifically, the MERE method output and the EMI receiver measurements differ by an average of only 2.6 dBμV at the fundamental and

first five harmonics identified in the table of Figure 4.8a. This agreement is on the same order as the agreement observed between different CISPR 16-1-1 compliant EMI receivers, as described in Section 4.3. This outcome further corroborates the validity of the MERE method for accurately characterizing the EMI performance of WBG-based power electronic systems. Figure 4.8b presents a comparison of the output of the MERE method from Experiment 1 (EMI receiver connected) and Experiment 2 (EMI receiver disconnected). The most notable feature of this plot is a reduction of 15.7 dBμV in emissions at the switching frequency (177 kHz) when the EMI receiver is disconnected from the system. The emissions profile at higher harmonics is also impacted by the removal of the EMI receiver although to a lesser degree than the fundamental frequency. These differences suggest that the flow of current through the EMI receiver ground connection significantly influences the EMI behavior of the system. Figure 4.9 presents a time-domain comparison of the leakage current through the output coupling of the converter load both with the EMI receiver connected (Experiment 1) and without the EMI receiver connected (Experiment 2). The exact measurement locations are shown in Figure 4.1. This comparison confirms that the testbed output leakage current increases by nearly 150% RMS when the EMI receiver is attached to the system. Figure 4.9 also demonstrates that nearly all of the output leakage current returns through the EMI receiver ground connection when it is attached (Experiment 1). Further testing was conducted increasing the dc bus voltage of the converter system from 600 VDC to 1000 VDC in 100-volt increments. The results, shown in Figure 4.10, show a direct increase in EMI receiver ground currents. The plot also shows the minimal ground current impact introduced by the oscilloscope and differential probe instrumentation which is connected in both experiments. Thus, the presence of a ground-referenced EMI receiver introduces a galvanic return path that increases the circulation of CM currents in the system. Additional experiments were performed

with varying load resistor values, but the plots were omitted for brevity. The same trends were observed in these alternative operating conditions suggesting this phenomenon is not specific to one set of operating conditions. The presence of this return path significantly influences the emissions behavior of the system under analysis. The net result is an exaggerated emissions profile, especially at the switching frequency, which may lead to an overly conservative design for the emissions control features of the system. It is also noted that this influence is caused by the conventional ground-referenced qualification instrumentation and is artificial in the sense that this influence would not be present in a deployed system.

In addition, the proliferation of circulating CM currents in the system during compliance testing also increases the risk of damage to the instrument itself. During this study, the EMI receiver manufacturers were consulted regarding the allowable level of ground current for these instruments. These discussions revealed that the instruments considered herein may incur internal damage with as little as 1.0 A_{rms} of ground current. In the authors' experience, ground current levels far in excess of this threshold occur during steady-state operation at DUT power levels of only a few kilowatts. In fact, the operating conditions utilized for the studies described in this paper were significantly modified to avoid exceeding the safe ground current threshold of the attached instrumentation. Even more concerning is the fact that the safe level of ground current may be exceeded without the operator's knowledge unless specific provisions are made for measuring this parameter. Such measurements require instrumenting the power cable of the EMI receiver, which is not common practice. Overall, these factors reinforce the need for isolated measurements during EMI compliance assessment of power electronic converters, which is one of the principal advantages offered by the proposed isolated method with MERE.

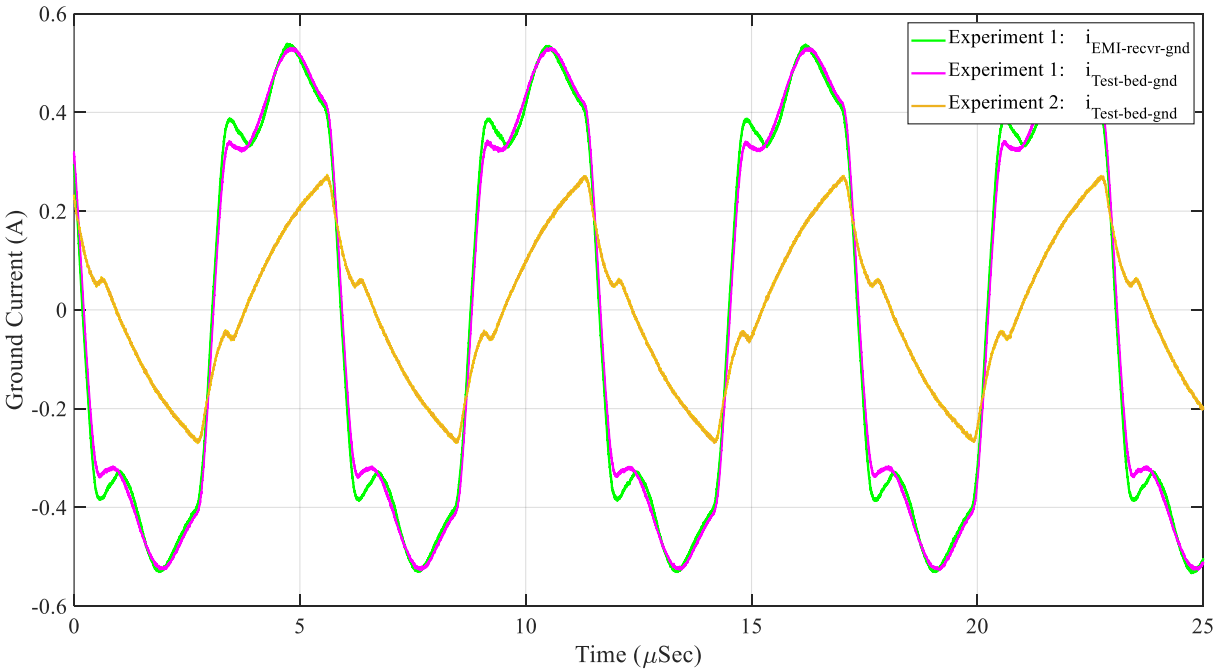

Figure 4.9 Ground Currents with (Experiment 1) and without (Experiment 2) the EMI Receiver Connected

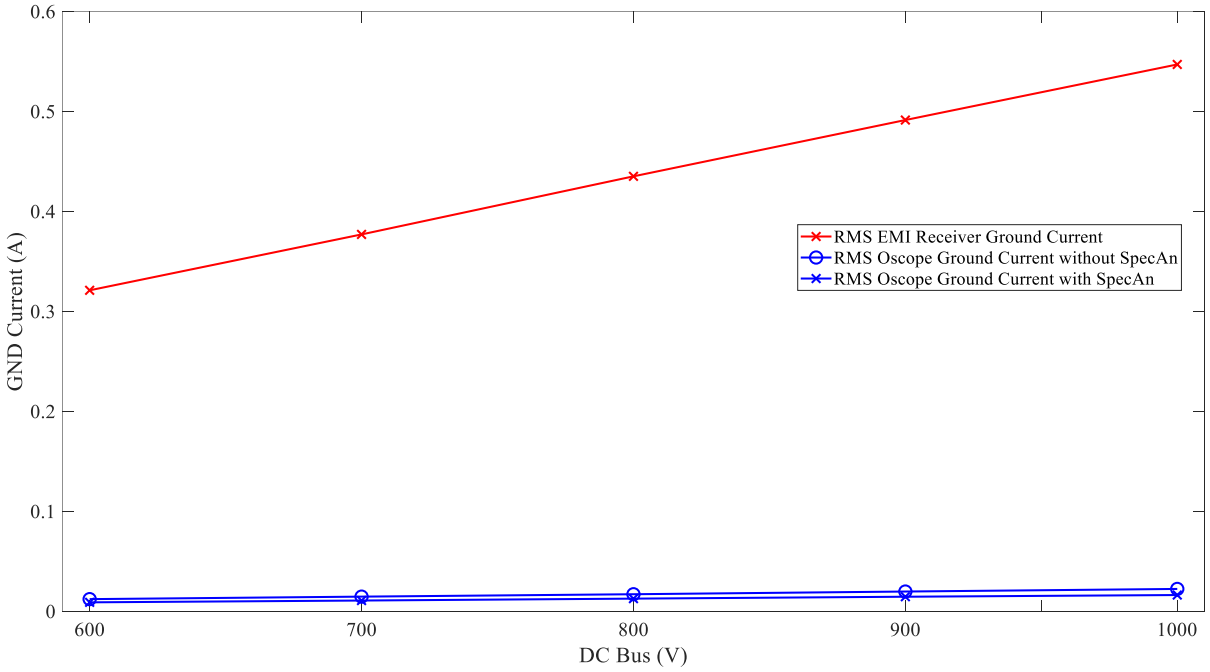

Figure 4.10 EMI Receiver Ground Current as a Function of DC Bus Voltage

4.6 Predictive Model Application

It is useful for designers to have a predictive tool to understand the potential impact of EMI receiver earth ground coupling to their design. This section presents models for predictive applications.

Based on prior work in chapter 2, an updated LTspice model was constructed that is representative of the test bed configurations of experiments 1 and 2 and is shown in Figure 4.11.

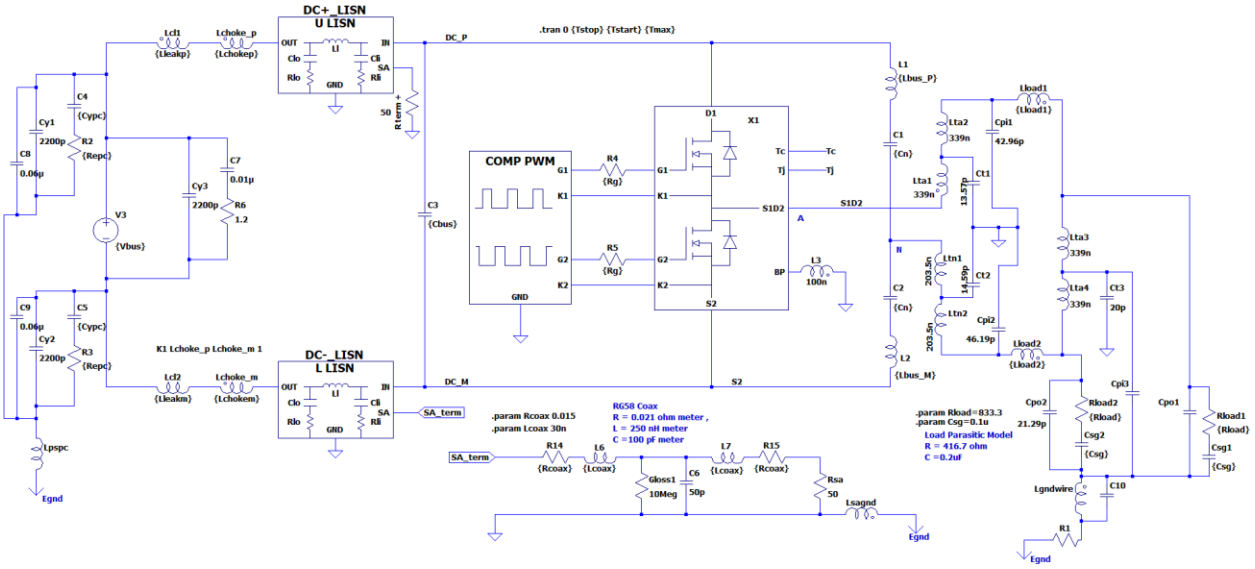

Figure 4.11 LTspice Simulation Model of Testbed for Experiments 1 and 2

The model updates include the addition of earth ground references, power supply filter components, LISN parasitics, EMI receiver load, and converter load with parasitics, which are all represented in the notational diagram of Figure 4.1. The circuit simulation was conducted in experiment 1 and 2 modes by connecting and disconnecting the earth ground reference from the 50Ω termination of the DC- LISN connection.

For validation, the experimental ground current measurements of Figure 4.9 were compared to LTspice and are shown in Figure 4.12. The LTspice simulation exhibits excellent agreement between experimental and simulation results for both configurations.

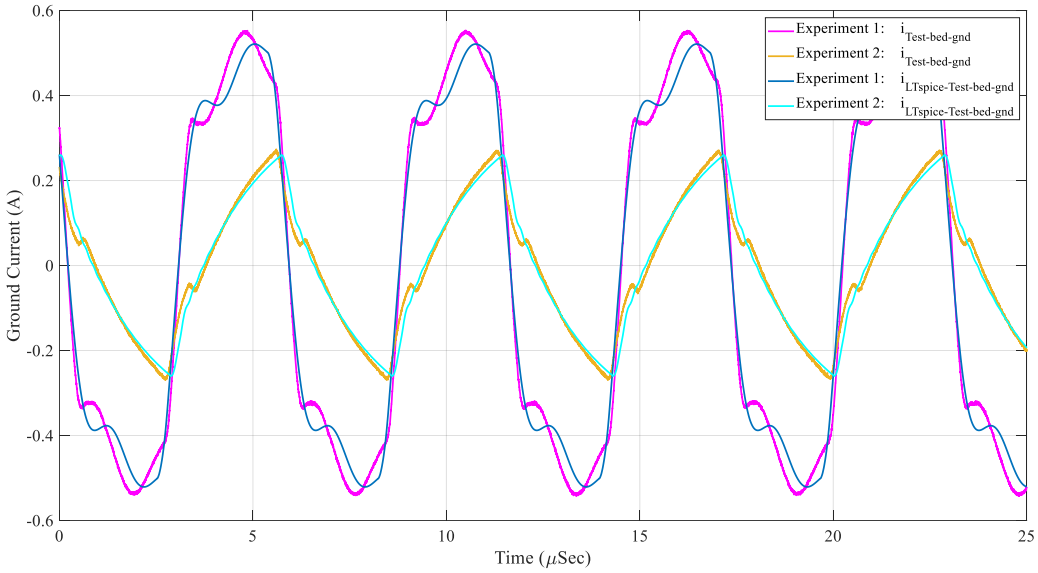

Figure 4.12 Empirical Testbed Ground Current Comparison with LTspice Simulation for Experiments 1 and 2

Next the LTspice simulation results were post processed with MERE and compared to Figure 8 also producing excellent agreement. These results were then used to compensate the EMI receiver data from experiment 1 by subtracting the LTspice differential spectral output.

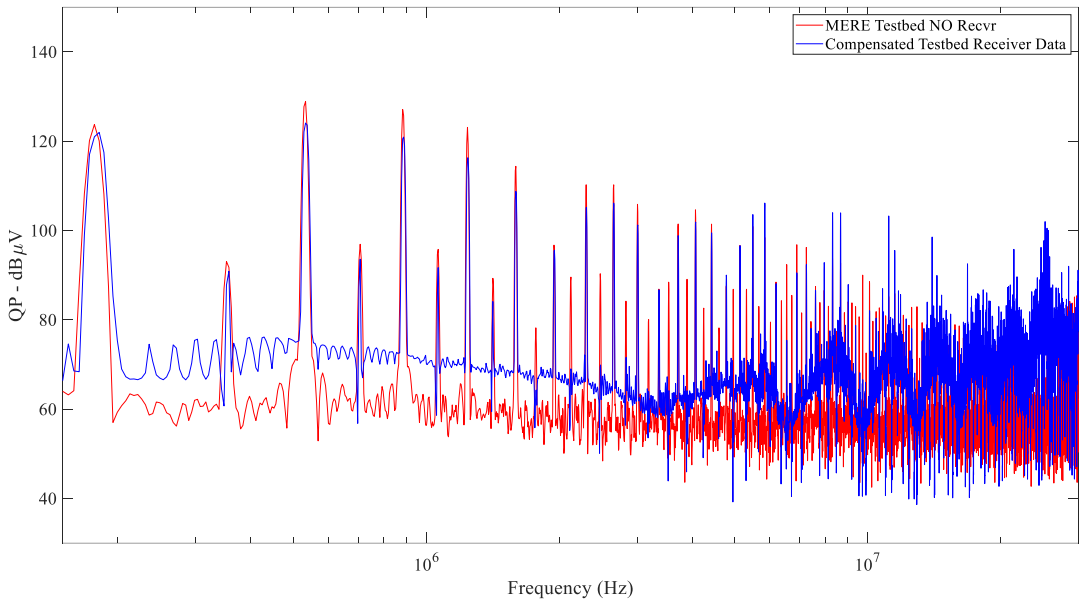

Figure 4.13 LTspice Compensated Testbed EMI Receiver Data from Experiment 1 Compared to Post processed Isolated Method of Experiment 2

As can be seen in Figure 4.13 the compensated testbed EMI Receiver data of experiment 1 has excellent agreement with the isolated method of experiment 2 in the low frequency range validating the LTspice predictive method for this band. This analysis, and the fact that the results of Figure 4.8b indicate the EMI receiver coupling only significantly impacts the fundamental frequency, led to further investigation to understand the root cause.

To better understand the common mode behavior a CEM was employed. Building on prior work for the base testbed from chapter 2, a new CEM was developed for the testbed configuration of Figure 4.1 and is shown in Figure 4.14. This model provides a clearer illustration of the common mode current paths for the two test cases of an EMI receiver connected and not connected in the system.

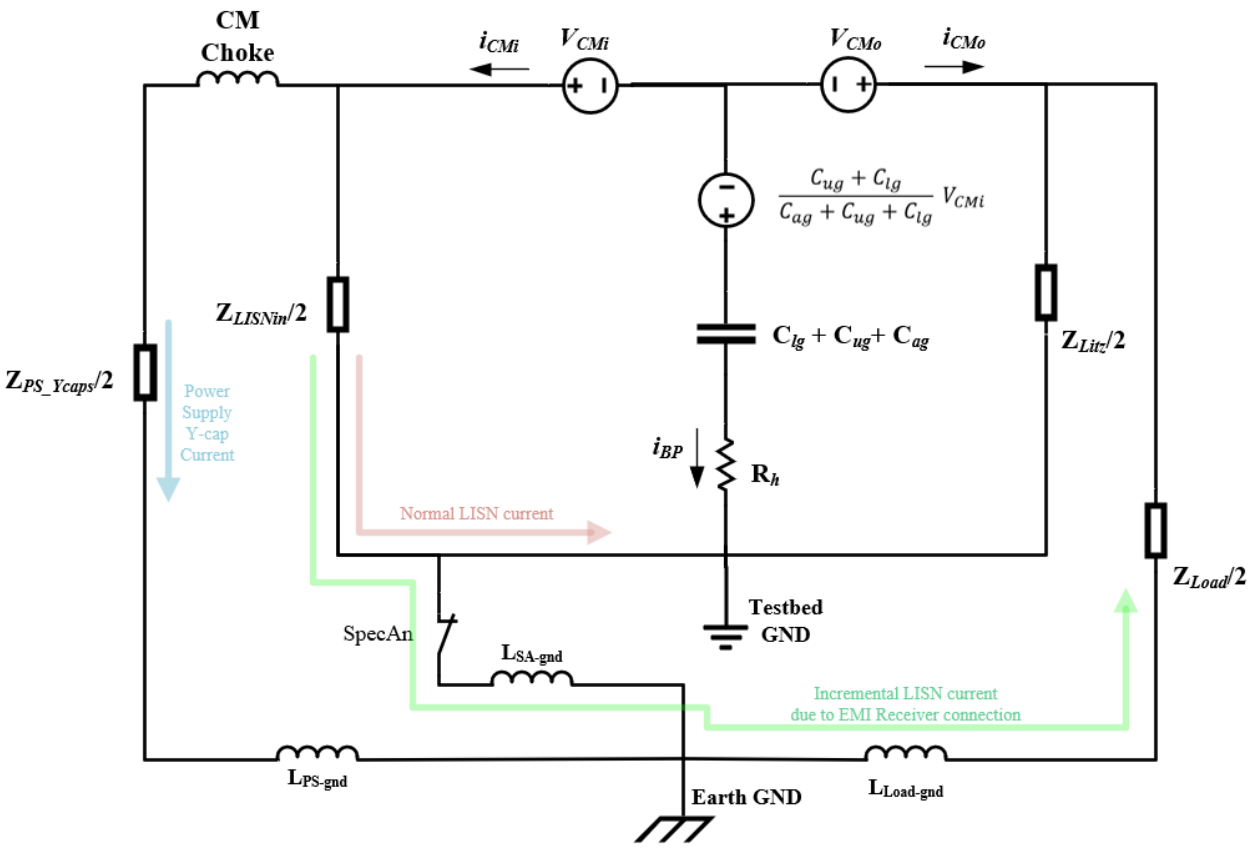

Figure 4.14 CEM Model for the Testbed Configuration of Figure 4.1 with Normal LISN Current (brown) and Incremental LISN Current (green) via the Earth Ground Connection.

The CEM was simplified by reducing the superfluous parasitics included in the LTspice model that were confirmed to have no significant impact. The model was then constructed in both MATLAB Simulink and LTspice as shown in Figure 4.15.

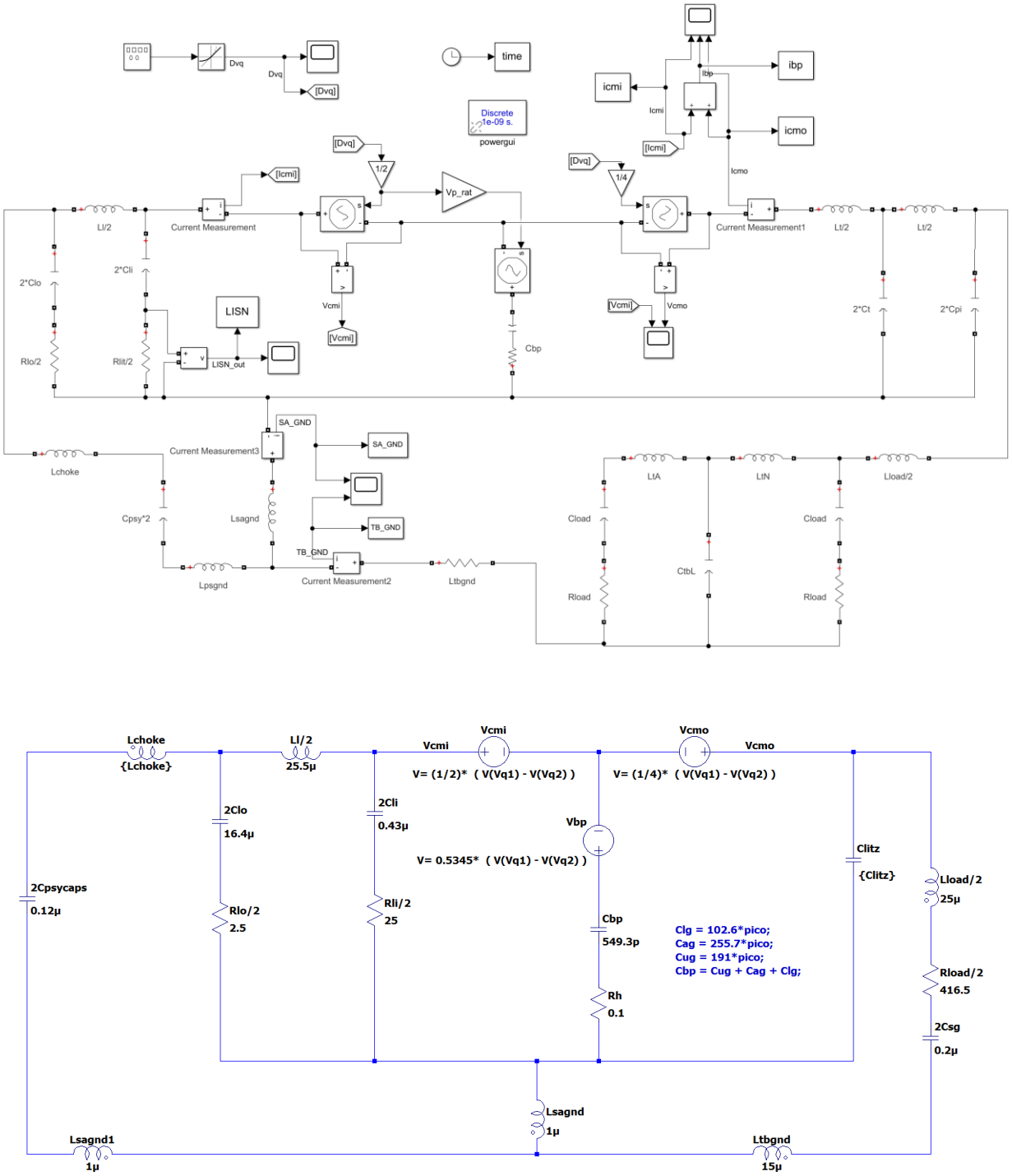

Figure 4.15 MATLAB Simulink (top) and LTspice (bottom) CEM Models for Testbed of Figure 4.1

Before being used to investigate frequency behavior, the CEM was validated to have good agreement with the testbed empirical results similar to the full LTspice model and is shown in Figure 4.16.

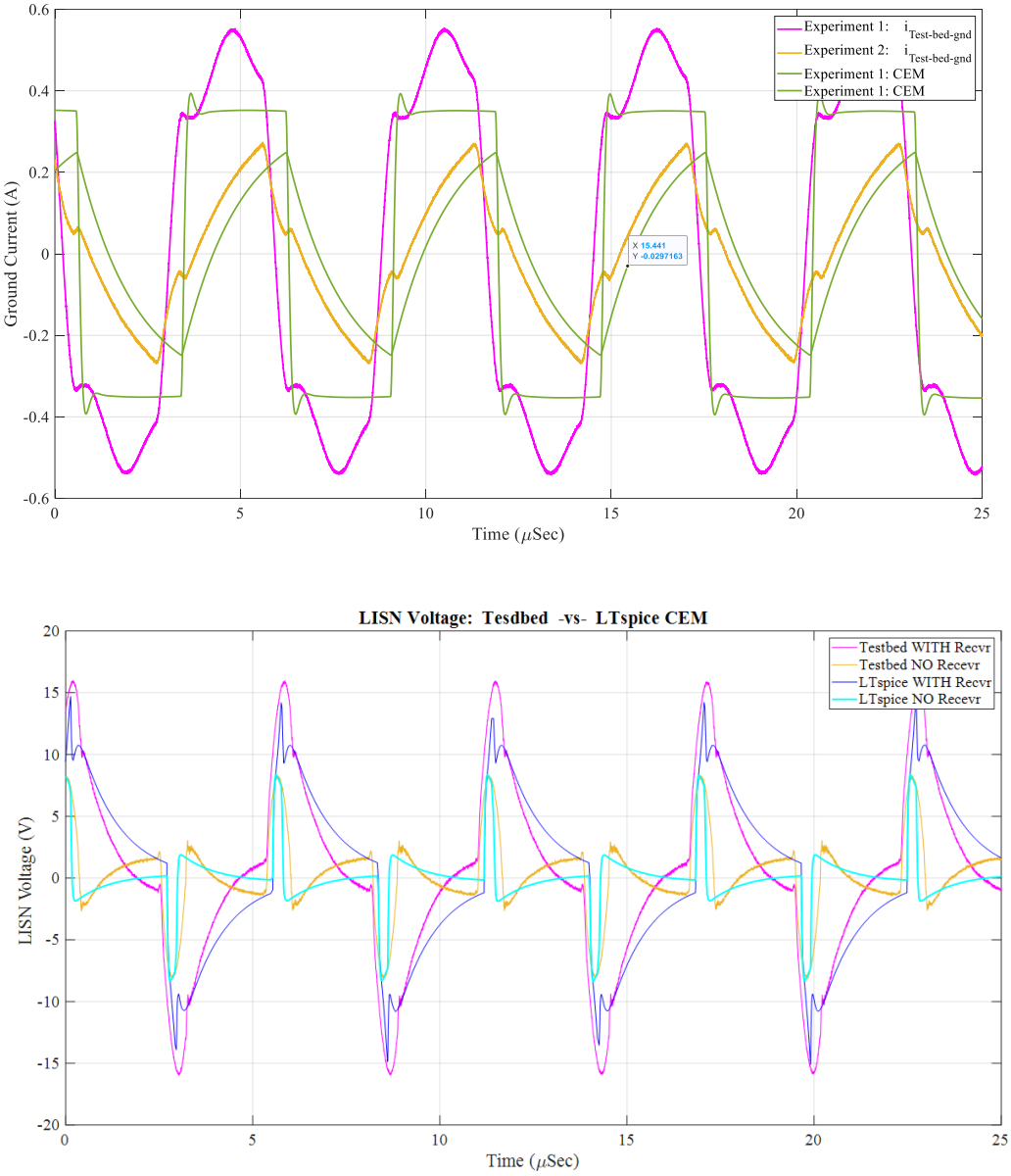

Figure 4.16 Empirical Testbed Ground Current Comparison (top) and LISN Voltage (bottom) with CEM Model for Experiments 1 and 2

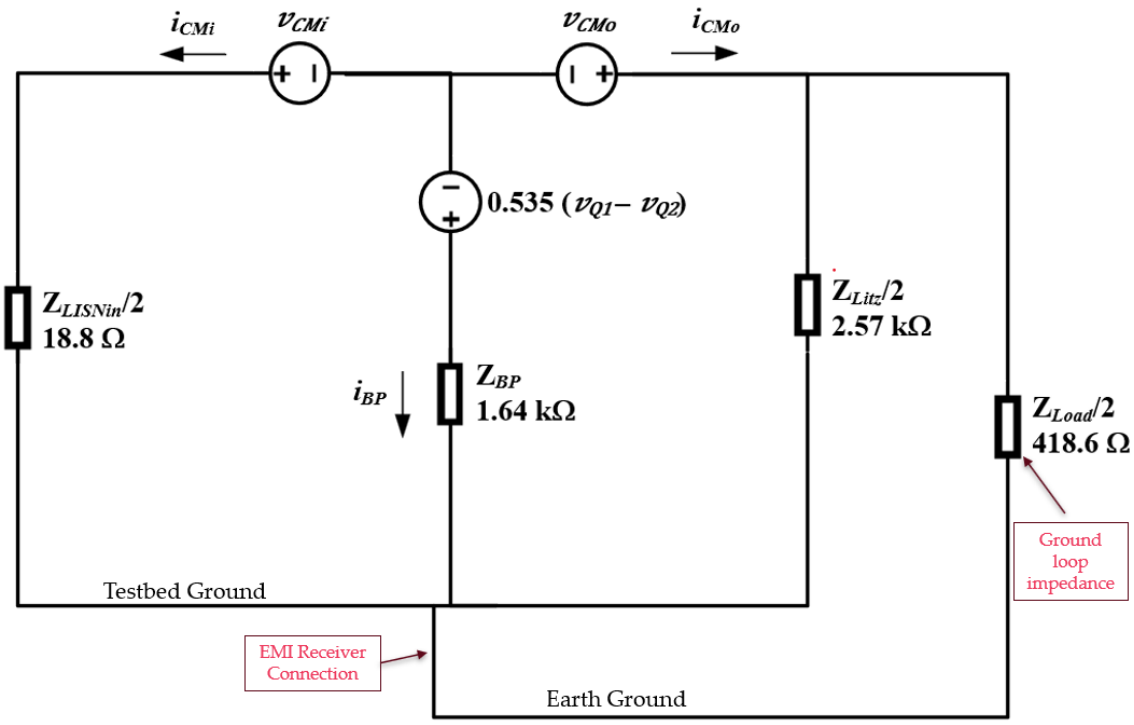

Figure 4.17 Simplified CEM with Load Impedances Magnitudes at Fundamental Frequency of 177kHz

Considerable analysis and evaluation of the CEMs determined the low impedance earth ground path is responsible for the EMI receiver coupling spectral behavior of Figure 4.8b. Specifically, this coupling is only significant near the fundamental frequency of 177kHz for the case when the EMI receiver is connected. At this frequency, significant incremental current is drawn through the LISN via the path of L_{LOAD}, $L_{SA\text{-}gnd}$, and $L_{TB\text{-}gnd}$, shown in green in Figure 4.14, as their total impedance is relatively low compared to the usual current return path thru Z_{LITZ}, shown in brown in Figure 4.14. This effect is further visualized in Figure 4.17 which shows the magnitude of impedances for the LISN, baseplate parasitics, and the loads at 177kHz. The impedance of the load side without EMI receiver connected is comprised of the litz wire parasitics and is relatively large at 2.57kΩ. Adding of the EMI receiver places the low impedance of the

ground loop, 418.6Ω, in parallel reducing the total impedance of that path to 419.9Ω greatly increasing the current flow. This behavior increases the EMI compliance voltage measurement at the LISN. The current through the power supply Y-capacitors, shown as the blue arrow in Figure 4.14, is negligible due to the sizeable CM choke. The earth ground path impedances increase directly with frequency, reducing the afore stated incremental LISN current and negating the coupling impact of the EMI receiver at frequencies above the fundamental frequency. This condition is observed in Figure 4.8b at frequencies above 700kHz and is additionally illustrated in Figure 4.18 showing a comparison 'With EMI Recvr' and 'NO EMI Recvr' of the experimental LISN current over frequency. Therefore, the earth ground conductor and its relatively low total impedance, is the key parameters impacting the compliance measurements with the EMI receiver connected.

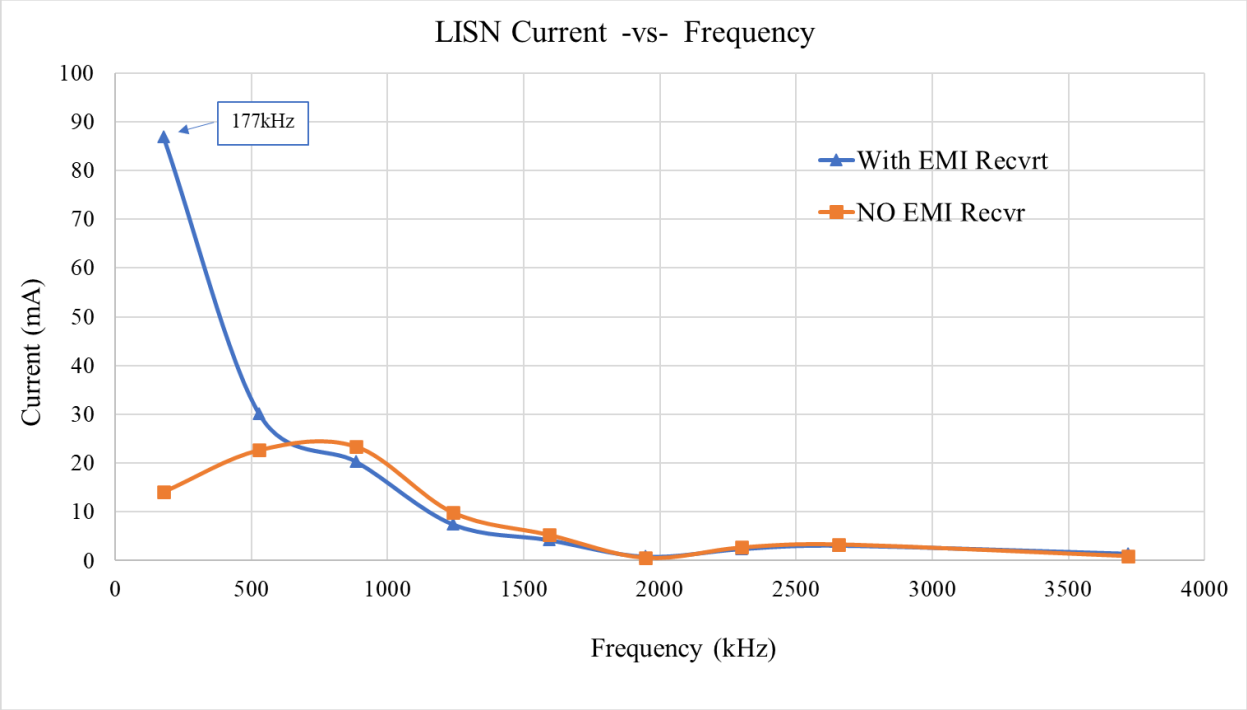

Figure 4.18 LISN Current Comparison versus Frequency With and Without EMI Receiver Connected

Furthermore, the impedance ratio of the load path impedances can be used to calculate the EMI receiver coupling to the EMI compliance metric at the fundamental frequency. The ratio of the impedance with no receiver connected to with a receiver connected is: $\frac{NO\ Recvr}{With\ Recvr} = 6.11$. This is confirmed with ratios from experimental data of LISN current: $\frac{With\ Recvr}{NO\ Recvr} = 6.17$ and the compliance metrics peak: $\frac{With\ Recvr}{NO\ Recvr} = 6.14$ and quasi-peak: $\frac{With\ Recvr}{NO\ Recvr} = 6.135$. Note the compliance metrics are calculated in volts and not dBμV. This excellent agreement validates the impedance ratio is a predictive tool that can accurately yield EMI compliance metrics for the case without an EMI receiver from experimental compliance data with an EMI receiver connected or vice versa.

This method can be applied to other systems by following this general application guideline:

- Develop CEM
    - Identify and confirm ground coupling components and parasitics
    - Derive CM sources
        - For half bridge refer to reference [21]
        - For full bridge refer to chapter 2.2
- Profile frequency response of system
    - Determine key frequency behavior points
- Conduct impedance analysis

4.7 Results

This work introduces an isolated approach for conducting EMI compliance analysis of power electronic converters using an oscilloscope, differential probes, and software-based post processing tool. This method provides two primary benefits for the analysis of WBG-based converters compared to the conventional approach, which involves a ground-referenced EMI receiver. First, the method provides galvanic isolation between the equipment under test and the instrumentation. This isolation reduces the circulation of leakage current through implicit CM coupling paths in the system, which would otherwise return through the EMI receiver ground lead. For the system considered here, the elimination of this leakage path is shown to reduce the conducted emissions at the fundamental frequency by 15.7 dBμV. This finding is consistent with emerging literature claiming that circulating CM currents can dramatically influence the emissions behavior of WBG-based converter systems. Second, the proposed method may also provide measurement accuracy benefits compared to the conventional approach when inline attenuators must be used to protect the input circuitry of the EMI receiver. This work also introduces a post-processing tool called the MATLAB EMI receiver emulator (MERE), which produces compliance metrics with comparable accuracy to those produced by commercially available EMI receivers. The proposed isolated measurement approach proposed can be readily implemented with common laboratory instrumentation and is amenable to the analysis of high-power, medium-voltage systems with minimal risk to the instrumentation. Lastly, predictive analysis techniques were introduced to give the designer an option to evaluate EMI receiver ground coupling impact prior to expending valuable lab resources.

Overall, the approach proposed herein is expected to yield improved emissions characterization of WBG-based converter systems, especially in the transition to medium-voltage applications.

CHAPTER V

CONCLUSION

5.1 Conclusion and Contributions

This research provided a complete comprehensive analysis of EMI filter imbalances allowing component variances to be profiled and understood and found that leakage inductance had the most significant impact on CM generation. Investigation of converter asymmetric deadtime switching was determined to have no impact on total CM noise and exhibited the characteristic of moving spectral energy in the band similar to spread spectrum techniques. Significant simulation models for converter topologies were developed, specifically the MERE tool for post processing time-domain data to produce EMI compliance metrics.

This research also includes a novel method to measure single phase line impedance. This method allows the designer to measure line stiffness accurately and effectively with readily available components for a fraction of a percent of the cost of a dedicated line impedance instrument. Also, the novel use of a capacitor load enables optimal accuracy given it initially acts as a short circuit and when rectified will cease conducting current upon reaching full charge. Resistive load techniques achieving comparable accuracy and SNR require switching intelligence, making them impractical to construct from discrete components. This characterization and quantification of line impedance can provide the designer with vital information to improve the robustness of their system's power input stage, including an EMI filter's attenuation performance and the reliability of protection components.

Lastly and most significant this work introduces an isolated approach for conducting EMI compliance analysis of power electronic converters using an oscilloscope, differential probes, and software-based post processing tool. This method provides two primary benefits for the analysis of WBG-based converters compared to the conventional approach, which involves a ground-referenced EMI receiver. First, the method provides galvanic isolation between the equipment under test and the instrumentation. This isolation reduces the circulation of leakage current through implicit CM coupling paths in the system, which would otherwise return through the EMI receiver ground lead. For the system considered here, the elimination of this leakage path is shown to reduce the conducted emissions at the fundamental frequency by 15.7 dBμV. This finding is consistent with emerging literature claiming that circulating CM currents can dramatically influence the emissions behavior of WBG-based converter systems. Second, the proposed method may also provide measurement accuracy benefits compared to the conventional approach when inline attenuators must be used to protect the input circuitry of the EMI receiver. This paper also introduces a post-processing tool called the MATLAB EMI receiver emulator (MERE), which produces compliance metrics with comparable accuracy to those produced by commercially available EMI receivers. The isolated measurement approach proposed in this paper can be readily implemented with common laboratory instrumentation and is amenable to the analysis of high-power, medium-voltage systems with minimal risk to the instrumentation. Predictive methods were also introduced to provide designers options to assess the impact of EMI receiver earth ground coupling prior to experimental analysis. Overall, the approach proposed herein is expected to yield improved emissions characterization of WBG-based converter systems, especially in the transition to medium-voltage applications.

5.2 Publications

Chapter 3 material is published and was presented at APEC 2022 conference March of 2022:

> M. Didat and S. Choi, "*Simple, Low Cost, Method for Measuring Single Phase Line Impedance*," 2022 IEEE Applied Power Electronics Conference and Exposition (APEC), Houston, TX, USA, 2022, pp. 1735-1741, doi: 10.1109/APEC43599.2022.9773660.

Chapter 4 material is published in the IEEE Open Journal of Power Electronics in October of 2022:

> M. Didat, C. D. New, S. Choi and A. Lemmon, "Improved Methodology for Conducted EMI Assessment of Wide Band-Gap Power Electronics," in *IEEE Open Journal of Power Electronics*, vol. 3, pp. 731-740, 2022, doi: 10.1109/OJPEL.2022.3214761.

5.3 Future Work

Opportunities for future work include:

- Compare the proposed line impedance method to conventional instrumentation and expand the proposed method to multi-phase systems
- Submit a paper covering the material in section 4.6
- Research the application of the proposed EMI assessment method and CEM predictive analysis on grounded power electronic systems and 120VAC consumer electronic systems
- Present the proposed isolated EMI assessment method to instrument manufacturers including Keysight, Rohde & Schwarz, and Gauss Instruments

REFERENCES

[1] Andrew N. Lemmon, Robert Cuzner, James Gafford, Methodology for Characterization of Common-Mode Conducted Electromagnetic Emissions in Wide-Bandgap Converters for Ungrounded Shipboard Applications, IEEE Journal of Emerging and Selected Topics in Power Electronics Volume: 6, Issue: 1, March 2018 , Pages: 300 – 314

[2] Andrew N. Lemmon, Modeling, measurement, and management of conducted EMI and common-mode behavior in shipboard power systems: Part III: EMI characterization, compliance, and mitigation methods, IEEE Conferences: 2017 IEEE Electric Ship Technologies Symposium (ESTS),Year: 2017,Pages: 1 – 53

[3] Aaron D. Brovont; Andrew N. Lemmon, *Common-mode/differential-mode interactions in asymmetric converter structures*, IEEE Conferences: 2017 IEEE Electric Ship Technologies Symposium (ESTS), Year: 2017, Pages: 84 – 90

[4] Robert Cuzner; Rasoul Hosseini; Andrew Lemmon; James Gafford; Michael Mazzola, Control and characterization of electromagnetic emissions in wide band gap based converter modules for ungrounded grid-forming applications, 2016 IEEE Applied Power Electronics Conference and Exposition (APEC), Year: 2016, Pages: 1577 – 1584

[5] Fred C. Lee, Shuo Wang, *Investigation of the Transformation Between Differential-Mode and Common-Mode Noises in an EMI Filter Due to Unbalance*, IEEE Transactions on Electromagnetic Compatibility Volume: 52, Issue: 3, Aug. 2010, Pages: 578 – 587

[6] J. Xue, F. Wang, B. Guo, EMI noise mode transformation due to propagation path unbalance in three-phase motor drive system and its implication to EMI filter design, Proc. IEEE Appl. Power Electron. Conf. Expo., pp. 806-811, Mar. 2014

[7] Heinz Rebholz, Stefan Tenbohlen, *Prospects and Limits of Common- and Differential-Mode Separation for the Filter Development Process*, Institute of Power Transmission and High Voltage Technology (IEH), Universität Stuttgart, Stuttgart, Germany, 2008

[8] Niall Oswald, Philip Anthony, Neville McNeill, and Bernard H. Stark, An Experimental Investigation of the Tradeoff between Switching Losses and EMI Generation With Hard-Switched All-Si, Si-SiC, and All-SiC Device, IEEE Transactions on Power Electronics, Volume 29, no. 5, pp. 2393-2406, May 2014

[9] Ernie Wittenbreder, Leakage Inductance (Part 3): Improving Power Supply Filtering, Efficiency, And Density, How2Power Today, ISSUE: November 2015

[10] Aaron D. Brovont, Andrew N. Lemmon, Christopher New, Blake W. Nelson, and Brian T. Deboi, *Cancellation of Leakage Currents through Power Module Baseplate Capacitance*, APEC, Year: 2019, PID2005

[11] M. V. Chilukuri, M. Y. Lee and Y. Y. Phang, "Voltage sag sensitivity of home appliances and office equipment," *CIRED 2009 - 20th International Conference and Exhibition on Electricity Distribution - Part 1*, 2009, pp. 1-6, doi: 10.1049/cp.2009.1096.

[12] S. Saksena and S. G. Karady, "Effects of voltage sags on household loads," *IEEE Power Engineering Society General Meeting, 2005*, 2005, pp. 2456-2461 Vol. 3, doi: 10.1109/PES.2005.

[13] J. M. Flores-Arias, F. J. Bellido-Outeiriño and A. Moreno-Munoz, "A fast RMS meter for detecting sag events in household environments," *2014 IEEE International Conference on Consumer Electronics (ICCE)*, 2014, pp. 321-322, doi: 10.1109/ICCE.2014.6776024.

[14] K. Matsui, H. Kojima, M. Koyama, I. Yamamoto, F. Ueda and H. Mori, "Some measurement techniques of distribution line impedance on hot-line," *2005 European Conference on Power Electronics and Applications*, 2005, pp. 8 pp.-P.8, doi: 10.1109/EPE.2005.219207.

[15] Zhenguo Shao, JinPing Peng and Jian Kang, "Locating voltage sag source with impedance measurement," *2010 International Conference on Power System Technology*, 2010, pp. 1-6, doi: 10.1109/POWERCON.2010.5666557.

[16] Manoj Gulati, Shobha Sundar Ram, and Amarjeet Singh. *2014*. An in-depth study into using EMI signatures for appliance identification. *In Proceedings of the 1st ACM Conference on Embedded Systems for Energy-Efficient Buildings (BuildSys '14)*. Association for Computing Machinery, New York, NY, USA, 70–79. DOI:https://doi.org/10.1145/2674061.2674070

[17] M. L. Gasperi, D. L. Jensen and D. T. Rollay, "Method for AC Powerline Impedance Measurement," in *IEEE Transactions on Industry Applications*, vol. 44, no. 4, pp. 1034-1037, July-aug. 2008, doi: 10.1109/TIA.2008.926189.

[18] Russell, Michael, "*The Impact of Mains Impedance on Power Quality*", Originally Presented at Power Quality 2000, Boston, MA, October 2000

[19] Square D, QO Molded Case Circuit Breakers Characteristic Trip Curve Number 730-3, Drawing number B48095-730-03, June 1995

[20] ASTM B258-14, "Standard Specification for Standard Nominal Diameters and Cross-sectional Areas of AWG Sizes of Solid Round Wires Used as Electrical Conductors", West Conshohocken: ASTM International.

[21] A. N. Lemmon, A. D. Brovont, C. D. New, B. W. Nelson and B. T. DeBoi, "Modeling and Validation of Common-Mode Emissions in Wide Bandgap-Based Converter Structures," in *IEEE Transactions on Power Electronics*, vol. 35, no. 8, pp. 8034-8049, Aug. 2020, doi: 10.1109/TPEL.2019.2963883.

[22] A. D. Brovont, A. N. Lemmon, C. New, B. W. Nelson and B. T. DeBoi, "Analysis and Cancellation of Leakage Current Through Power Module Baseplate Capacitance," in *IEEE Transactions on Power Electronics*, vol. 35, no. 5, pp. 4678-4688, May 2020, doi: 10.1109/TPEL.2019.2944410.

[23] G. Escobar, P. R. Martinez-Rodriguez, S. Iturriaga-Medina, J. C. Mayo-Maldonado, J. Lopez-Sarabia and O. M. Micheloud-Vernackt, "Mitigation of Leakage-Ground Currents in Transformerless Grid-Tied Inverters via Virtual-Ground Connection," in *IEEE Journal of Emerging and Selected Topics in Power Electronics*, vol. 8, no. 3, pp. 3111-3123, Sept. 2020, doi: 10.1109/JESTPE.2019.2933399.

[24] D. N. Dalal *et al.*, "Impact of Power Module Parasitic Capacitances on Medium-Voltage SiC MOSFETs Switching Transients," in *IEEE Journal of Emerging and Selected Topics in Power Electronics*, vol. 8, no. 1, pp. 298-310, March 2020, doi: 10.1109/JESTPE.2019.2939644.

[25] B. Mirafzal, G. L. Skibinski and R. M. Tallam, "Determination of Parameters in the Universal Induction Motor Model," in *IEEE Transactions on Industry Applications*, vol. 45, no. 1, pp. 142-151, Jan.-Feb. 2009, doi: 10.1109/TIA.2008.2009481.

[26] CISPR 16-1-1 ed3.0 - Specification for radio disturbance and immunity measuring apparatus and methods - Part 1-1: Radio disturbance and immunity measuring apparatus - Measuring apparatus, *CISPR Std.*, 2010-01-29, page.

[27] Title 47 – Telecommunication, Chapter I - Federal Communications Commission, Subchapter A – General, Part 15 - Radio Frequency Devices, October 1, 2010, page 775.

[28] J. H. Cook, "Quasi-Peak-to-RMS Voltage Conversion," *in IEEE Transactions on Electromagnetic Compatibility*, vol. EMC-21, no. 1, pp. 9-12, Feb. 1979.

[29] P. Lezynski, "Random Modulation in Inverters With Respect to Electromagnetic Compatibility and Power Quality," in *IEEE Journal of Emerging and Selected Topics in Power Electronics*, vol. 6, no. 2, pp. 782-790, June 2018, doi: 10.1109/JESTPE.2017.2787599.

[30] S. Linkwitz, "Realization of CISPR Quasi-Peak Detection Requirements with an Envelope Quasi-Peak Detector*," 1984 International Symposium on Electromagnetic Compatibility*, Tokyo, 1984, pp. 1-5.

[31] A. M. Trzynadlowski, M. Zigliotto, S. Bolognani and M. M. Bech, "Reduction of the electromagnetic interference conducted to mains in inverter-fed AC drives using random pulse width modulation," *Conference Record of 1998 IEEE Industry Applications Conference*. Thirty-Third IAS Annual Meeting (Cat. No.98CH36242), St. Louis, MO, USA, 1998, pp. 739-744 vol.1.

[32] J. Wei, D. Gerling and S. P. Schmid, "Prediction of conducted EMI in power converters using numerical methods," *2012 15th International Power Electronics and Motion Control Conference (EPE/PEMC)*, Novi Sad, 2012, pp. DS1a.3-1-DS1a.3-6.

[33] K. Muller, "Speeding up quasi peak weighting EMI tests," *IEEE 1991 International Symposium on Electromagnetic Compatibility*, Cherry Hill, NJ, USA, 1991, pp. 169-172.

[34] *TDEMI X Datasheet*, GAUSS INSTRUMENTS International GmbH, Munich, Germany, 2017

[35] L. Yang, S. Wang, H. Zhao and Y. Zhi, "Prediction and Analysis of EMI Spectrum Based on the Operating Principle of EMC Spectrum Analyzers," in *IEEE Transactions on Power Electronics*, vol. 35, no. 1, pp. 263-275, Jan. 2020.

[36] F. Krug and P. Russer, "Quasi-peak detector model for a time-domain measurement system," in *IEEE Transactions on Electromagnetic Compatibility*, vol. 47, no. 2, pp. 320-326, May 2005.

[37] Chenggang Li, Li Zhang, Tian Dong, Tao Wang and Henglin Chen, "An EMI receiver model with consideration of the intermediate frequency filter," *2016 Asia-Pacific International Symposium on Electromagnetic Compatibility (APEMC)*, Shenzhen, 2016, pp. 233-236, doi: 10.1109/APEMC.2016.7523018.

[38] T. Karaca, B. Deutschmann and G. Winkler, "EMI-receiver simulation model with quasi-peak detector," *2015 IEEE International Symposium on Electromagnetic Compatibility (EMC)*, Dresden, 2015, pp. 891-896.

[39] "MIL-STD-461G", Requirements for the control of electromagnetic interference characteristics of subsystems and equipment, Dec. 2015.

[40] Dipl. -Ing. Dieter Schwarzbeck, "The EMI-Receiver according to CISPR 16-1-1," *Schwarzbeck Mess-Elektronik*, An der Klinge 29, D-69250 Schönau / Germany

[41] W. Schaefer, "Signal detection with EMI receivers," *1998 IEEE EMC Symposium. International Symposium on Electromagnetic Compatibility. Symposium Record (Cat. No.98CH36253)*, Denver, CO, USA, 1998, pp. 761-765 vol.2, doi: 10.1109/ISEMC.1998.750295.

[42] F. Giezendanner, J. Biela, J. W. Kolar and S. Zudrell-Koch, "EMI Noise Prediction for Electronic Ballasts," in *IEEE Transactions on Power Electronics*, vol. 25, no. 8, pp. 2133-2141, Aug. 2010, doi: 10.1109/TPEL.2010.2046424.

[43] *N9038A MXE EMI Receiver Datasheet*, Keysight Technologies, Santa Rosa, CA, 2019

[44] *Spectrum Analysis Basics*, Application Note AN150, Keysight Technologies, Santa Rosa, CA, Published in USA, October 10, 2020, 5952-0292

[45] *Tektronix 4/5/6 Series MSO, LPD64 (MSO44, MSO46, MSO54, MSO56, MSO58, MSO58LP, MSO64,LPD64)*, Instruction Manual, 077-1303-11

[46] *Tektronix THDP0100/0200 & TMDP0200 High Voltage Differential Probes*, Instruction Manual, 077-0540-01

[47] *HAT -20+ Coaxial Fixed Attenuator*, Datasheet, Mini-Circuits, REV. G M151107 EDR-5087/3 HAT-20+ RVN/LC/CP/AM 150724

APPENDIX A

SUPPORTING ANALYSIS AND DOCUMENTATION

A.1 MERE Comparison to Yang/Wang Method

Additional analysis was performed to compare MERE to the predictive method proposed by L. Yang, et al. for computing the QP spectra in [35]. This approach was implemented in MATLAB and utilized to evaluate the testbed experimental data studied previously. The results of this comparison are shown in Figure A.1. It is noted that the results from MERE and the Yang method demonstrate substantial differences. Specifically, the fundamental and harmonic peaks are different by as much 7.8 dBμV, and the frequency floors differ by as much as 20 dBμV at several regions of the band. While some of these discrepancies may be explained by the tolerance provisions of the standard, it is likely that the approximations utilized in [35] also contribute to these differences. Further noise floor analysis is presented in Appendix section A.2.

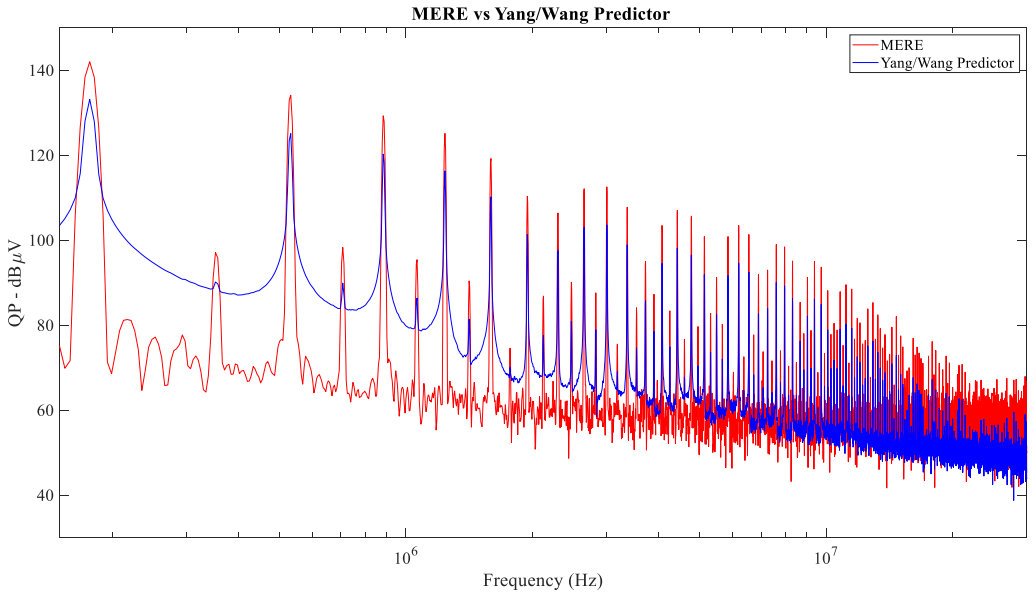

Figure A.1 Comparison between MERE and Yang, Wang et al. Predictor [35]

A.2 Noise Floor Analysis

Noise floor differences are observed in the different analyses of chapter 4. This artifact was further investigated with significant impact found due to the inline attenuation that was intentionally installed or internal to the instrumentation.

Ambient noise measurements were performed for both metrology configurations considered in chapter 4: the EMI receiver and the isolated metrology using MERE. The results of this analysis are presented for two idle states of the test bed. In Figure A.2, the gate drivers were on and switching at 177 kHz with the testbed set to 0 Vdc. In Figure A.3, the testbed was again at 0 Vdc and the gate drivers were powered on, but in this experiment, the gate drivers were not switching. In both cases, the ambient noise peaks are in good agreement for the two metrology setups, but the noise floor is consistently higher for the EMI receiver compared to the oscilloscope setup. The reason for the elevated noise floor observed with the EMI receiver is the presence of the 60 dB attenuation required to protect the instrument's input from the high input DC voltage. This attenuation restricts the dynamic range of the EMI receiver and therefore limits its ability to measure small signals. Figure A.4 compares the EMI receiver signal with and without the 60 dB attenuator attached, with no input signal. This plot confirms that the attenuators are the cause of the 60 dB noise floor elevation.

It is important to note that noise floor variance is not a significant factor for evaluating compliance per the limits of Table 4.2 as it is typically orders of magnitude lower than QP and average peaks throughout the spectra.

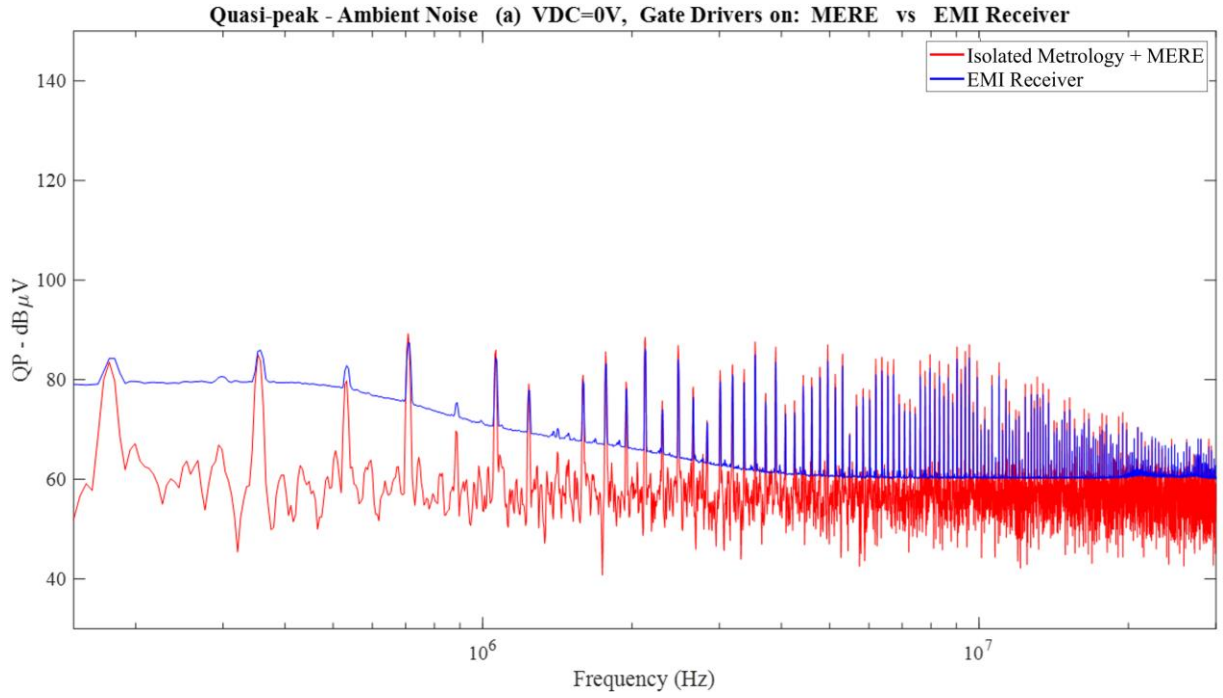

Figure A.2 Testbed Noise Floor Measurements at Vdc = 0 V and Gate Drivers Switching

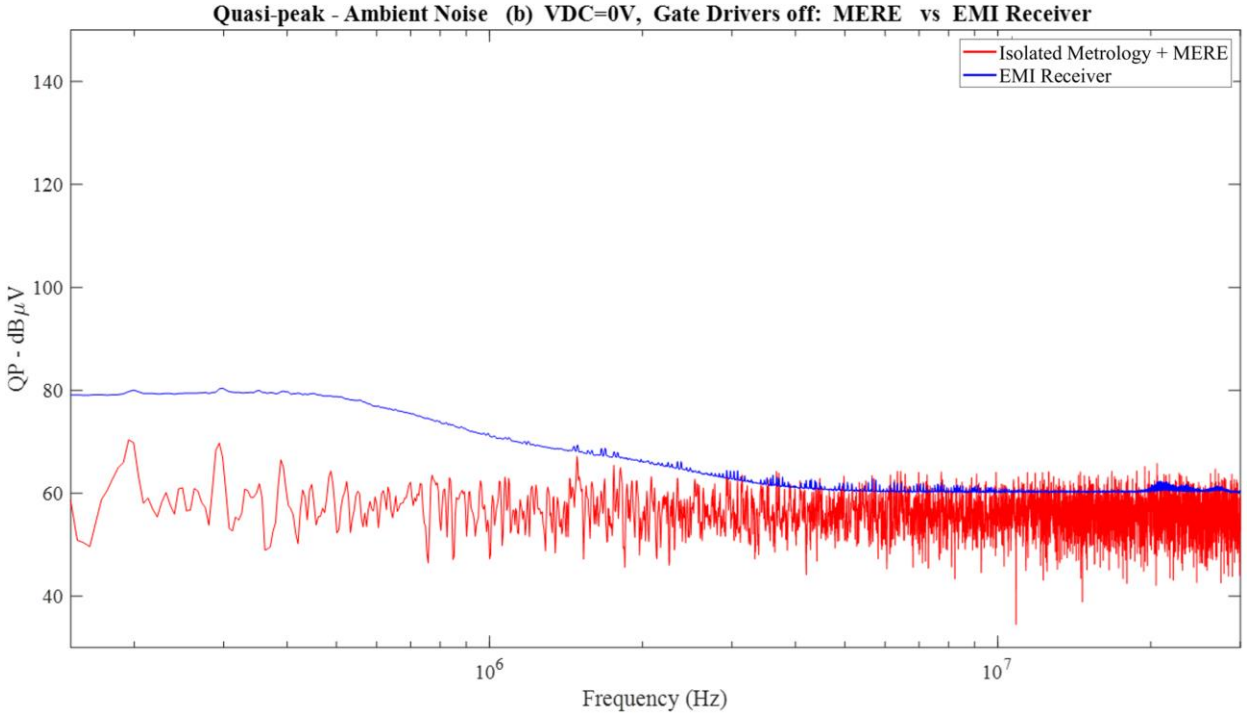

Figure A.3 Testbed Noise Floor Measurement at Vdc = 0 V and Gate Drivers not Switching

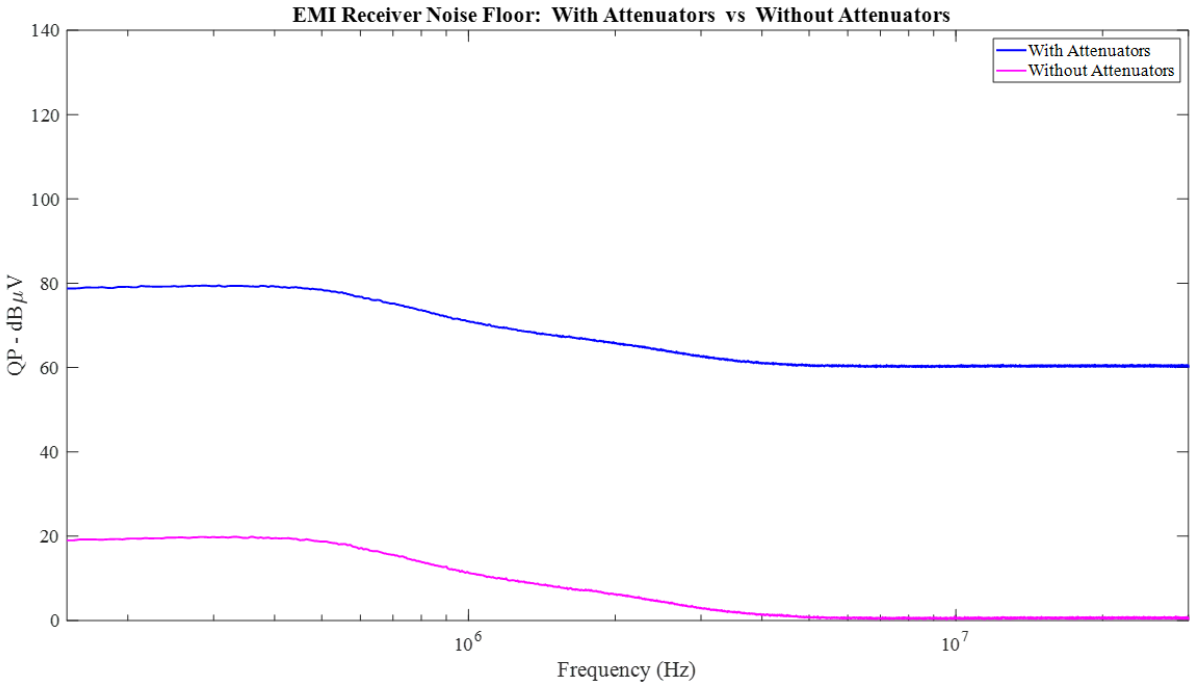

Figure A.4 Noise Floor Measurements with and without Attenuators